UNIVERSIDADE Ð
COIMBRA

Jacinto Renato Pinto Fonseca

MAGNETIC INELASTIC DARK MATTER SEARCHES IN LUX

Dissertação no âmbito do Mestrado em Física Nuclear e de Partículas orientada pelo Professor Doutor Cláudio Frederico Pascoal da Silva e apresentada ao Departamento de Física da Universidade de Coimbra.

Julho de 2020

Magnetic Inelastic Dark Matter searches in LUX

Jacinto Fonseca

July 2020

Sumário

O trabalho apresentado nesta tese focou-se no estudo de Matéria escura inelástica magnética, MiDM. Este é um dos modelos propostos para explicar a discrepância entre os resultados obtidos pela experiência DAMA/LIBRA e os resultados obtidos por outras experiências de detecção directa de Matéria Escura.Primeiramento, introduziu-se a problemática da Matéria Escura, através do foco nas evidências da existência de Matéria Escura, possíveis candidatos a Matéria Escura e métodos de detecção de Matéria Escura. Além disso, foram também descritas as propriedades físicas de Xenon, a importância do Xenon para os detectores de Cintilação e o princípio de funcionamento de um detector TPC de duas fases. Descreveu-se também o equipamento usado no detector de LUX, as calibração efectuadas em LUX e o pacote de software NEST no contexto dos modelos de campo eléctrico de LUX.Depois disso, abordou-se a problemática da Matéria Escura Magnética Inelástica, MiDM, de um ponto de vista teórico e de análise de dados.Do ponto de vista teórico, recorreu-se às linguagens de programação python e Mathematica para construir um modelo de sinal para MiDM através de uma análise sobre os factores de forma, a secção eficaz diferencial, e a taxa de eventos diferencial do WIMP.Finalmente, foi feita a análise da Matéria Escura Inelástica Magnética (MiDM), considerando os dados recolhidos por LUX entre 11 de setembro de2014 e 2 de maio de 2016, que correspondem à Run IV. Estes dados foram usados para estudar várias propriedades associadas a MiDM, como a tipologia de eventos, a profundidade do evento obtida pela assimetria entre o topo e o fundo do detector para o pulso S1, a forma do pulso S2, a probabilidade de emparelhamento das sequências cronológicas associadas a um sinal produzido por MiDM e as fontes de fundo associadas a MiDM. Para que a análise descrita neste trabalho seja concluída no futuro, será necessário estudar os factores que afectam a eficiência, adicionar a contribuição da largura do pulso S2 aos cálculos

da probabilidade de emparelhamento e considerar um recuo nuclear para o primeiro pulso.

Abstract

The work described in this thesis focused on the study of Magnetic inelastic Dark Matter, MiDM. This was one of the models proposed to explain the discrepancies between DAMA/LIBRA and other direct detection dark matter results.Firstly, it was introduced the Dark Matter subject, focusing on Dark Matter evidences, candidates for particle Dark Matter and methods for Dark Matter detection.It was also described the physics of Xenon, its importance to scintillation detectors and the working principle dual-phase TPC detector. Also, it is briefly described the hardware of the LUX detector, its calibrations and the NEST software package in the context of LUX electric field models.After that, this work focused on Magnetic Inelastic Dark Matter, MiDM, by a theoretical and data analysis perspective. From a theoretical point of view, it was discussed a signal model for MiDM, with a python and Mathematica analysis on the form factors, differential cross-section and WIMP differential event rate.Finally, it was made an analysis on Magnetic inelastic Dark Matter(MiDM) using the data collected by the LUX detector between September 11, 2014 and May 2, 2016, corresponding to the Run IV dark matter search. This data was used to study several properties associated to MiDM, such as its event typology, the depth of the event from S1 top-bottom asymmetry and S2 pulse shape, the paring probability of the chronological sequences associated with a signal produced by MiDM and the background sources associated with MiDM. The analysis described in this work would be concluded by studying the factors that affect the efficiency, adding the S2 pulse width contribution to the pairing probability calculations and considering a nuclear recoil for the first pulse.

Acknowledgements

First of all, I would like to thank to my advisor, Doctor Cláudio Silva for his patience, guidance and support throughout the development of this thesis.

I would like to thank to rest of the members of the Juri: Doctors Maria Isabel Lopes, Fernando Amaro and Filipa Borges.

I also would like to thank to the LIP Dark Matter Group, namely to the Professors Alexandre Lindote, Vladimir Solovov and Francisco Neves, and to my co-workers Ricardo Cabrita, Cédric Pereira, Guilherme Pereira and Andrey Solovov.

I thank to my family for their support and consideration during this long academic period. To my mother Maria da Graça Pinto, my grand-father Carlos Pinto, my brother Oliver Fonseca and my sisters Ana Cecília Fonseca and Leonor Fonseca.

I thank to some of my friends and people that accompanied me during this long journey. To Mafalda Marques, Fábio Horta, Jan Vincent Bersier, Paola di Nunzio, Pedro Monney, Pedro Réquio, Diogo Barbosa, Pedro Martins, Teresa Andrein, Judit Jesus, Filipe Pereira and Rita Silva.

Finally, I would like to give a special thanks to República do Kuarenta, which was my home during most of my academic period.

Physical constants and Acronyms

c	Speed of light in a vacuum inertial system	$299,792,458\, m/s$
G	Gravitational Constant	$6.67384 \times 10^{-11}\, N \cdot m^2/kg^2$
$M_\odot$	Solar Mass	$1.9891 \times 10^{30}\, Kg$
bckg	Background	
CMB	Cosmic Microwave Background	
coi	Coincidence	
DM	Dark Matter	
EFT	Effective Field Theory	
ER	Electronic Recoil	
iDM	inelastic Dark Matter	
keV$_{ee}$	kilo electronvolts, assuming an electronic recoil for the energy reconstruction	
keV$_{nr}$	kilo electronvolt, assuming a nuclear recoil for the energy reconstruction	
LUX	Large Underground Xenon	
LXe	Liquid Xenon	
LZ	LUX-ZEPLIN	
MiDM	Magnetic inelastic Dark Matter	
NEST	Noble Element Simulation Technique	
NR	Nuclear Recoil	

PHD	photo-electron detected
PHE	photo-electron
PMT	Photomultiplier tube
RQ	Reduced Quantities
SM	Standard Model
SS	Single Scatter
SURF	Sanford Underground Research Facility
TPC	Time Projection Chamber
WIMP	Weakly Interacting Massive Particle

Contents

Introduction

The work described in this thesis will focus on the study of Magnetic inelastic Dark Matter, MiDM [1, 2]. This was one of the models proposed to explain the discrepancies between DAMA/LIBRA and other direct detection dark matter results [2, 3].

This thesis is structured by four chapters that study Magnetic Inelastic Dark Matter, MiDM, by a theoretical and data analysis perspective. In the first chapter, it is introduced the Dark Matter subject, focusing on Dark Matter evidences and candidates for particle Dark Matter. In the second chapter, there is a description of Xenon physics, its importance to scintillation detectors and the working principle of a dual-time projection chamber (dual-phase TPC) detector. Also, it is briefly described the hardware of the LUX detector, its calibrations and the NEST software package in the context of LUX electric field models. In the third chapter, the signal model for MiDM is discussed with a python and Mathematica analysis on the form factors, differential cross-section and WIMP differential event rate. In the last chapter, the LUX detector data is analysed from the MiDM model perspective, including an analysis on the background sources of MiDM.

Chapter 1

Astrophysical evidences for Dark Matter

During the past decades, it has been suggested that the energy density of our universe is dominated by two main components with an almost unknown nature, namely Dark Energy and Dark Matter [4, 5]. Dark Energy is an almost uniform component of the universe, being responsible for the expansion of the universe [5]. Dark Matter is a type of matter whose interactions with ordinary matter are observed only through gravitational and probably weak forces, excluding the electromagnetic and strong forces [4, 5, 6].

In this chapter, the subject of dark matter will be discussed. There will be introduced some evidences for dark matter existence, some of its more reliable candidates, and the methods to detect this type of matter.

1.1 Evidence for Dark Matter

The first evidences for dark matter were described in the 1930s by Jan Oort and Fritz Zwicky [7]. They both studied the dynamics of galaxies and clusters of galaxies [8]. In 1932, Jan Oort measured the velocities of stars in several galaxies, such as the Milky Way and NGC 4594 galaxy, also known as Sombrero Galaxy or M104 [8, 9]. From these measurements, he discovered that the stars were moving faster than the expected for the observed velocities on luminous matter [9]. In spite of Jan Oort suggesting the existence of additional unseen mass to explain this observations, these phenomena can also be explained by unseen dwarf stars or absorption from interstellar gas or dust [10, 11]. In 1933, Fritz Zwicky estimated the mass of the Coma cluster (Abell 1656), following two different methods: obtaining this mass experimentally, measuring the Coma Clusters's luminosity, and theoretical calculations on the Coma Cluster's mass, using the virial theorem.

Fritz Zwicky applied the virial theorem to the Coma Cluster, which expected mass is given by [10]

$$M_c = \frac{3}{G}\langle v_r^2\rangle R_c \tag{1.1}$$

where M_c is the mass of the Coma Cluster, ,v_r is the radial projection of the velocity and R_c is the radius of the Coma Cluster and G= 6.672 $\times 10^{-11}$ N m^{2}kg^{-2} is the gravitational constant [10, 12]. For the mass of the Coma Cluster, M_c, Fritz Zwicky obtained 4.5 $\times 10^{13} M_\odot$, at the order of 500 times bigger than the mass inferred from luminosity [10, 13, 14]. For the mass that was not accounted, Zwicky called it "dunkle Materie", german for dark matter.

At a smaller scale, another evidence for dark matter was observed in the 1970s [15, 16]. This evidence came from the rotational curves of spiral galaxies, consisting on the graphs that relate the circular velocity of galactic constituents, $v(r)$, to the distance from the center of the galaxy, known as galactic radius, r [10, 16]. To obtain these velocity curves, they measured the Doppler redshift of the 21-cm emission line of hydrogen as a function of the radial distance to the galactic center [10, 17].

From Newtonian mechanics and Kepler laws, the expected circular velocity for spiral galaxies, $v(r)$, is described by [10, 16, 18]

$$v(r) = \sqrt{\frac{GM(r)}{r}}, \tag{1.2}$$

where $M(r)$ is the mass of the galaxy contained inside the radial distance r [10, 19]. At a large radii, the equation 1.2 shows a dependence of the velocity on the radius square root, such as $v(r) \propto r^{-1/2}$ [10]. From this dependence, it is expected that stars and gas further away from the center of the galaxy to move slower than those closer to the mass concentrated in the center region of the galaxy, known as bulge mass.

The velocity curves of spiral galaxies were first studied by Vera Rubin and Kent Ford [18, 19]. From their observations, Vera Rubin and Kent Ford stated that the data shows a flat distribution of velocities, which is not consistent with the theoretical predictions given by the equation 1.2 at large radii [10, 18]. An example

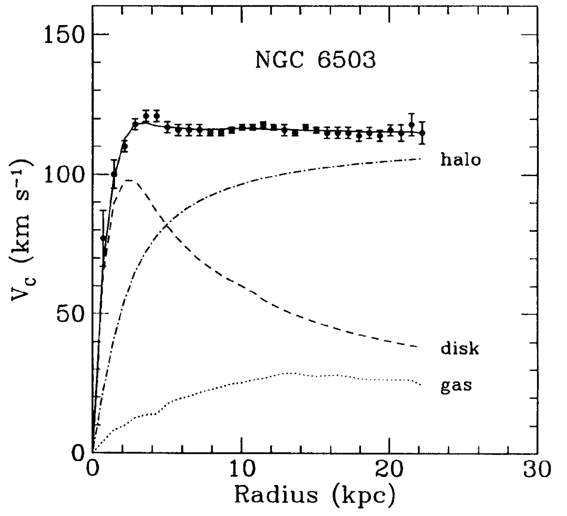

Figure 1.1: Velocity distribution curve of the NGC 6503 galaxy [15].

of this behaviour is shown in figure 1.1 for the NGC 6503 dwarf spiral galaxy [20]. From these figure, the observed behaviour correspond to a flat rotation curve [21]. This curve implies that the mass in the galaxy has a proportional behaviour with the distance to the center of the system [10]. This is shown in equation 1.2 for a constant $v(r)$, which implies $M(r) \propto r$. The figure 1.1 also shows the expected velocity curve, which is described by the "disk" plus "gas" curves [15, 21]. For the velocity curve of galaxies, the discrepancies between the observations and theoretical predictions are explained by the existence of huge dark halos of dark matter on the galaxies composition, in addition to the luminous matter [18].

For the previous dark matter evidence, it was assumed a Newtonian dynamics approach for the galactic scales [21]. For scales similar to the solar system, the measurements confirm this behavior for gravity. As an alternative to dark matter, several scientists suggested that the galactic evidence of Fritz Zwicky and Vera Rubin can be explained by modified Newtonian dynamics for larger scales, namely the MOdified Newtonian Dynamics (MOND) [21, 22]. This idea was tested with measurements in a bullet cluster, which are composed clusters who have recently collided and passed through each other [23].

Consequently, the collision between the two clusters lead the baryonic matter to heat and emit X-rays, which are observed and used to map the luminous mass distri-

Figure 1.2: Image of the galaxy cluster 1E 0657-56, known as Bullet Cluster [24]. Chandra X-ray Observatory image (pink) and dark matter mass distribution (blue) obtained from weak lensing measurements and overlaid by visible light from the Hubble Space Telescope [24, 25]

bution. Alternatively to the analysis of particle velocities, the mass distribution of massive objects at a galactic scale can be obtained indirectly, using the gravitational lensing technique [21, 26].

Based on General Relativity, gravitational lensing is a consequence of space-time distortion [25, 27]. This effect occurs when a distribution of matter between a distant light source and an observer bends light from the source, as it follows a geodesic path from its source to detection on earth [26, 28]. As opposed to luminous matter, the emitted light will appear to bend around nothing for a dark matter distribution [28]. Gravitational lensing distorts space-time in a more visible way when this effect results in arcs and multiple images of the background object, namely strong gravitational lensing [17]. Because of the high non-linearity of the strong lensing, these distortions are few and difficult to measure. Alternatively, the more common form of lensing is weak gravitational lensing, consisting in a much smaller space-time distortion [17, 29]. This effect results in images that are only slightly distorted, being only detected by measuring a large number of sources [10, 17].

Both strong and weak gravitational lensing are used to measure the size and distribution of dark matter halos, obtaining the mass density required to cause the observed lensing [11]. An example of weak gravitational lensing observations is a set of images of the Bullet Cluster 1E 0657-56, obtained by the Hubble telescope [24]. In the figure 1.2, it is shown a composite of these images accompanied by

X-ray observations of the Bullet Cluster by the Chandra X-ray observatory. It shows the contributions of the X-rays emitted by baryonic matter in pink, while the contributions of the mass from gravitational lensing are represented in blue [23]. Until recently, most of the scientists claimed that gravitational lensing could not be explained by a modified newtonian dynamics, because the amount of mass obtained from gravitational lensing is larger than the luminous mass [21]. According to them, this would demonstrate that the matter obtained from gravitational lensing decouples from baryonic matter induced by the formation of the bullet cluster [21, 23]. This decoupling would imply the existence of a non-luminous and non-baryonic matter, which favours the existence of dark matter [10, 21]. Most recently, this assumption has been contradicted by other scientists that proposed newest relativistic formulations of MOND [30]. Such formulations solve the problem of gravitational lensing in relativistic theories of MOND, but are unable to explain temperature fluctuations in the cosmic microwave background and particle abundances in the early universe [30, 31, 32]. These cosmological phenomena will be discussed further below.

At a cosmological scale, another evidence for dark matter came from anisotropies on Cosmic Microwave Background, CMB. CMB is a thermal radiation that isotropically fills the Universe and it closely follows and ideal black body spectrum with a temperature of T = 2.726 K [10, 20]. Before the formation of CMB, the universe was filled with a hot, dense plasma consisting of electrons and baryons in thermal equilibrium [29, 33]. In this period, the photons scattered off of the electrons, restricting their movement across the universe and causing it to be opaque to radiation [21, 33]. The average temperature of the universe decreased due to its expansion and the photons became less energetic [21]. When the universe cooled to about 3000 K, its energy reached a value below the binding energy of hydrogen of 13.6 keV [20, 33]. This caused the protons and electrons to combine, forming neutral hydrogen atoms, [33]. As photons had enough energy to ionize the hydrogen, the universe became transparent to radiation and the photons were no longer in thermal equilibrium with the electrons [20, 21]. These photons decoupled from the electrons and formed the cosmic microwave background, CMB [21].

In spite of filling the universe isotropically, CMB has small anisotropies that come

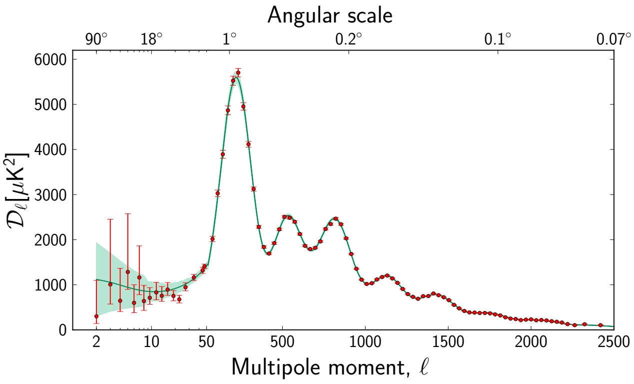

Figure 1.3: Power Spectrum of the Cosmic Microwave Background, obtained from the Planck 2015 data [34].

from temperature fluctuations of the order of $\frac{\delta T}{T} \sim 10^{-4}$ [10, 18, 20]. As shown in the figure 1.3, these fluctuations are well studied by the temperature power spectrum obtained in the analysis of the CMB anisotropy data from Planck 2015 results [10, 35]. By applying a fit to the power spectrum, it was determined the size and position of peaks shown in the figure 1.3 [29]. From this fit, it is possible to collect valuable information on the curvature and energy-matter composition of the universe in the form of the density parameter, Ω_i, that is given by [16, 20]

Table 1.1: Sample from Planck 2015 fit results [10, 16, 29].

Parameter	Symbol	Measured Value
Baryonic matter density	Ω_b	0.02230 ± 0.00014
Cold Dark Matter density	Ω_{CDM}	0.1188 ± 0.0010
Total matter density	Ω_m	0.3089 ± 0.0062
Dark Energy density	Ω_λ	0.6911 ± 0.0062
Curvature	Ω_k	$0.0008^{+0.0040}_{-0.0039}$

$$\Omega_i = \frac{\rho_i}{\rho_c} \tag{1.3}$$

where ρ_i is the density of the species i and ρ_c is the density required for flatness, also known as critical density [20, 29]. In the table 1.1, there are shown the best fit parameters from the Planck 2015 results for the energy content of the universe [10, 16, 29]. This results are consistent with a flat, dark energy dominated universe, as described by the model known as ΛCDM or standard model of cosmology [29].

1.2 Dark Matter Candidates

Some of the evidence for dark matter was shown in the previous section of this chapter. In addition to show evidence for dark matter existence, it is also necessary to investigate its nature [36].

As a starting point, it was proposed that dark matter could be explained without the addition of any new particles [28, 36]. As an example, the dark matter halo was considered to be composed by baryonic, massive non-luminous bodies of regular matter, namely Massive Compact Halo Objects, MACHOs [10, 36]. Among others, these massive objects would consist of neutron stars, white dwarfs, brown dwarfs, Jupiter-like planets and black holes [10]. Such baryonic objects should be detectable through the measurement of changes in the brightness of more distant stars due to gravitational lensing by more nearby MACHOs, namely microlensing experiments [19]. From these searches, it was determined that less than 25% of the dark halos could be due to baryonic dark matter, with masses between 2 $\times 10^{-7}$ and one solar mass at a 95% confidence limit [33]. Another constraint on MACHOs as baryonic dark matter comes from measurements of the contribution of baryons to the energy density of the universe [37]. Theoretically, it was expected the abundances of light elements and cosmic microwave background to be consistent with the predictions made from the big bang nucleosynthesis, which is the theory that explains the production of light elements during the early universe. However, the measurements obtained a baryon contribution of less than 20 % of the total matter of the universe. In spite of these constraints, it remains possible that MACHOs could exist in the form of primordial black holes, if they were formed before nucleosynthesis [19]. However, this assumption has not been yet confirmed experimentally.

The standard model also contains non-baryonic candidates for dark matter, such as the neutrinos [8]. They are good dark matter candidates due to their properties, as they are stable, interact with ordinary matter very weakly and are massive [20]. As relativistic dark matter candidates, the neutrinos are collectively known as Hot Dark

Matter [38]. However, large structure formation requires that the universe should have a non-relativistic, Cold Dark Matter component [23]. During this period, this dark matter component would become gravitationally bound to galaxies. This is confirmed by the observations on galaxy clusters, Cosmic Microwave Background and Lyman-α [33, 38]. Although, it is possible to consider a different hypothesis related to the neutrino [19]. It consists in a extension of the standard model, adding a right-handed neutrino, known as sterile neutrino [29]. However, they can only be cold and account for structure formation for some particular scenarios. In addition, there is no solid evidence for the sterile neutrinos existence, in spite of some claims of their existence due to some experiments anomalous results [29, 39].

Another dark matter candidate is the Axion, which consists of a light boson [19, 25]. The Axion was proposed by Peccei-Quinn to solve the strong CP problem [25]. This problem consists of a symmetry breaking due to CP violation on strong interactions, which was predicted by Quantum Chromodynamics, QCD, but not observed experimentally [7, 21]. According to Peccei-Quinn, the axions are particles with low mass, electrically neutral and stable, which have very weak interactions with the strong and weak forces [33]. It was originally predicted that the axion would have a mass around 100 keV [8]. However, this prediction has been ruled out experimentally [8, 29]. Alternatively, the searches have been focused on ”invisible” axion models [8]. These particles can interact via an axio-electric effect, which is similar to the photoelectric effect [29]. They can also interact through a coupling between the axion and two photons, mediated by a presence of a magnetic field. Searches for axions were made on experiments such as CAST, ADMX CASPER, LUX and XENON [18].

The most popular candidates for dark matter are the Weakly Interacting Massive Particles, WIMPs [4, 40]. They consist of stable particles that interact with ordinary matter through weak and gravitational forces [29, 40]. In addition to their stability, WIMPs have a mass in the order of 10-1000 GeV, which means that the WIMPs are heavy enough to be non-relativistic in the early universe [29]. It is believed that WIMPs were in thermal and chemical equilibrium in the early universe [4, 38]. During this phase, the temperature was higher than the mass of the WIMPs, and they frequently annihilated with one another, being continuously produced by interactions between lighter particles. As the universe cooled and expanded, the WIMPs were no longer able to annihilate rapidly enough to maintain equilibrium [4, 16, 38]. As a consequence, they become thermally decoupled from other particle species in a process called ”freeze-out” [19]. The quantity of WIMPs that were left behind by this process is known as relic abundance of WIMPs [38].

In spite of their popularity as dark matter candidates, the WIMPs have not yet been discovered [28]. However, their detection is expected as the current and next generation experiments will test the limits of the WIMP parameter space. This will be tested for several models, such as the lightest Supersymmetric particle, LSP.

Examples of other WIMP candidates are dark photons, neutralinos from supersymmetry theories, lightest Kaluza-Klein particle from theories with Universal Extra Dimensions (UED) and other theories beyond the Standard Model of particle physics [41, 42]. In this work we will explore Magnetic inelastic Dark Matter, assuming that the WIMP follows an inelastic kinematics and has a non-zero magnetic moment [3].

1.3 Dark Matter detection methods

There are three possible methods to detect dark matter particles, which correspond to couplings between dark matter and the standard model particles [19]. These methods consist of: particle production in colliders, indirect detection through annihilation and direct detection via low energy recoil dark matter experiments [43].

The production of WIMPs in colliders is a result of the annihilation of two Standard model particles [19]. As a result of this annihilation, the production of WIMPs can be accompanied by jets, a photon, a Z or W boson, a lepton, or even nothing at all [25]. Rather than being detected directly, the WIMPs produced in the colliders appear as missing energy and momemtum, enabled by the reconstruction of event energies [16, 44]. This event reconstruction would allow for direct determination of the WIMP mass, considering the missing energy greater than twice of the WIMPs mass [8]. So far the search of events with missing momentum and energy was not able to detect dark matter [28]. This is due the signal of excess beyond the standard model has yet to be observed at collider experiments [28, 44]. Some of the searches of WIMP production in colliders have been performed at the LHC at CERN and at the Tevatron at Fermilab [10, 19].

Indirect detection consists of two WIMPs annihilating each other, resulting on the creation of standard model particle-antiparticle pairs with high energy, such as gamma ray photons, neutrinos, or electron-positron pairs. [4, 10, 28]. These searches often focus on regions where dark matter is expected to be high, such as the galactic center, the sun or dwarf galaxies [4, 7]. This is due the annihilation rate being proportional to the square number of density of WIMPs [4]. Dark matter indirect searches have the potential to detect the decay products from the hypothesised dark matter particles [17]. To observe these decay products, they must be stable and distinguishable from the background. It is very difficult to known if an observed decay corresponds to an indirect Dark Matter signal, because of potential backgrounds from astrophysical sources, which nature is unknown [31]. Some examples of indirect dark matter experiments are Fermi-LAT and ANTARES and IceCube [10, 33].

The direct detection consists on the detection of interactions between hypothesised dark matter particles and target materials and is processed via energy recoils between 1 and 100 keV [40, 43]. As examples of target materials, there are crystal scintillators, semiconductor crystals, liquefied noble gases and superheated liquid [40].

For this method of detection, the interactions with the target materials lead to heat, scintillation light and ionization electrons. One or more of these signals are detected by direct detection experiments, such as DAMA/LIBRA, PICO, CDMS, LUX, LZ, PandaX and XENON1T among other experiments. These experiments are known for operating in an extremely low background regime, with less than 1 evt/kg/year as a current limit for WIMP recoils, as shown in the figure 1.4 [43, 45]. In this figure, it is shown an overview over the current spin-independent limits on the cross-section for various dark matter direct detection experiments [45, 46]. The most sensitive limits on the WIMP mass have been achieved by the XENON1T experiment, comparing with other direct detection experiments [45].

The XENON1T experiment consists of a dual-phase Xenon detector, located at the Laboratori Nazionali del Gran Sasso, with a total volume of 3.2 tonnes and 2

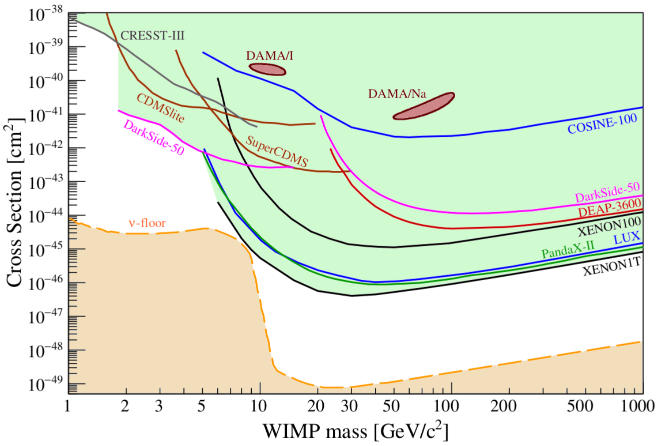

Figure 1.4: Spin-independent limits on the cross-section for various dark matter direct detection experiments [45].

tonnes of active volume [47, 48]. This experiment operations occurred between 2011 and 2018, reaching to a limit on the WIMP-nucleon spin-independent cross section of 1×10^{-47} cm^2 for a mass of 30 GeV/c^2 [48].

As a part of the XENON project, the work developed on the XENON1T experiment will continue with the XENONnT and DARWIN experiments [48, 49]. As XENONnT and DARWIN operations will occur during the next decade, they are known as next generation experiments [45, 48, 49].

XENONnT consists in an update of the XENON1T experiment, having a total mass of 8.4 tonnes and a active volume mass of 5.9 tonnes. Its projected limit for the WIMP-nucleon spin-independent cross section is 1.6×10^{-48} cm^2 for a mass of 50 GeV/c^2 [48, 50]. XENON1T operations are projected to occur between 2019 and 2023 [48, 51]. After the end of the XENONnT operations, DARWIN will begin its operations in 2025, with a total mass of 50 tonnes, and an active volume mass of 40 tonnes [49]. Among other physics goals, this experiment aims to reach a WIMP-nucleon cross sections in the order of 10^{-49} cm^2 for masses of $\sim$ 50 GeV/c^2.

The LUX-ZEPLIN (LZ) is another example of a next generation experiment, consisting in the merge of two previous dark matter direct detection experiments, namely LUX and ZEPLIN [52]. In the figure 1.5, it is shown the LUX-ZEPLIN (LZ) projected sensitivity to spin-independent scattering compared with other direct detection experiments, such as PandaX, XENON1T and LUX. In the next chapter, we will describe the LUX experiment in more detail.

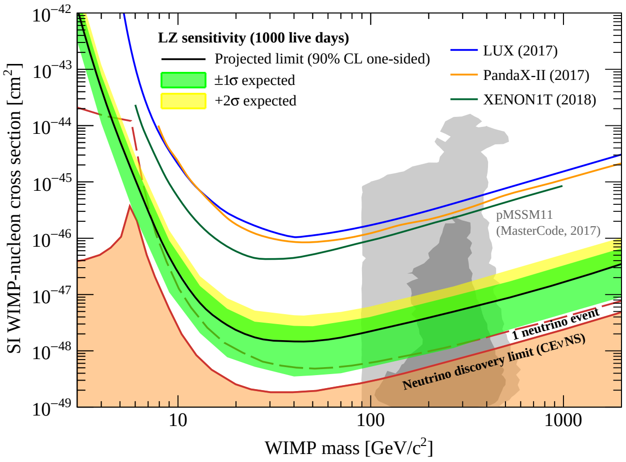

Figure 1.5: Spin-independent limits on the cross-section for LZ comparing with other direct detection experiments [52].

In the next decade, XENONnT, DARWIN, LZ, and other experiments will seek to lower the spin-independent limits on the cross-section, in order to directly detect WIMPs [48, 49, 52].

Chapter 2

Dark Matter Direct Detection: The Liquid Underground Xenon experiment

The LUX detector was a dual phase liquid/gas Time Projection Chamber filled with 380 kg of Liquid Xenon, of which 250 kg were present in the region enclosed by the detector walls between the high voltage grids [4, 29]. LUX operated at the Sanford Underground Research Facility, SURF, in Lead, South Dakota (USA) between 2012 and 2016 [19]. It is located in the Davis Cavern, 1478 m below the surface. LUX was designed and built for direct detection of WIMPs, maintaining a background expectation of less than one WIMP-like background event in 30 000 kg·days [10, 53]. With this overall goal, it was expected the experiment to reach a WIMP-nucleon spin-independent cross-section down to 2×10^{-46} cm^2 for a WIMP mass around 50 GeV/c^2 at a 90 % Confidence Level (C.L.) [10, 53, 54]. During its operations, the LUX experiment achieved a limit on both the WIMP-nucleon spin-independent and WIMP-neutron spin-dependent cross sections of 1.1×10^{-46} cm^2 for a 50 GeV/c^2 at a 90 % C.L., and 1.6×10^{-41} cm^2 for a 35 GeV/c^2 at a 90 % C.L., respectively [54, 55].

In this chapter, we will discuss the advantages of xenon as a target nuclei, the dual phase TPC mechanism, the LUX detector hardware and calibrations and its response model.

2.1 Advantages of Xenon as a target nuclei

One of the advantages of xenon as a target nuclei is its high atomic weight, A, which mean value is around 131.29 [10, 56]. This property enhances spin-independent interactions, which cross section scales with A^2 [56]. This causes also the liquid xenon to be denser than the other liquid noble gases ($\rho_{LXe} = 2.888 \pm 0.005$ g·cm^3), which increases the capacity of a detector to enclose a substantial target mass, resulting in higher WIMP interaction rates [10].

Another advantage of using Xenon is its high atomic number, Z=54, which allows good self-shielding for penetrating radiation, mainly in the form of γ and β particles. Self-shielding is a property of Xenon detectors that allows the outer regions of the xenon volume to absorb much of the external γ radiation, leaving the inner volume with a highly reduced background. As an example, a γ particle with an energy of 100 keV has a mean free path of about 2 mm in liquid xenon, requiring thirty mean free paths to penetrate into the liquid xenon region [23].

Natural Xenon has 9 stable/almost stable isotopes, namely ^{124}Xe, ^{126}Xe, ^{128}Xe, ^{129}Xe, ^{130}Xe, ^{131}Xe, ^{132}Xe, ^{134}Xe and ^{136}Xe [10, 17, 55]. From this set of isotopes, it is known that ^{124}Xe and ^{136}Xe isotopes are unstable, but they have a very long half-life [57, 58]. ^{124}Xe decays with a very long half-life (double electron capture) of 1.8×10^{22} years [57]. ^{136}Xe decays with a very long half-life by double beta decay ($\sim 2.165 \times 10^{21}$ years [58]). The isotopes ^{126}Xe and ^{134}Xe are only observationally stable, but nuclear models predict them to be unstable with a even larger half-life compared to ^{124}Xe and ^{136}Xe [59]. The long half-life of this isotopes does not have a significant impact in the background rate of the detector. The remaining isotopes are stable. From these stable isotopes, the only ones that have an odd spin are ^{129}Xe and ^{131}Xe isotopes, which allows for a competitive sensitivity to spin-dependent WIMP-neutron elastic cross section [28].

Xenon has also very low electronegativity of 2.6, allowing the electrons to drift over large distances, as long as detector's impurities, such as N_2, O_2 and H_2O are minimized [21, 60, 23]. These impurities degrade the free electron attenuation length and they must be removed in order to properly reconstruct the events in the detector [23].

Xenon is a very good scintillator, having the largest light yield comparatively to the other rare gaseous detectors, which varies between 50 and 70 phd/keV for low energy recoils [56, 61]. It produces scintillation at a 175 nm wavelength, in the vacuum ultra violet (VUV) region, which makes xenon transparent to its own scintillation, allowing the photons to travel through the liquid without a significant attenuation [17, 56].

Xenon has the highest boiling point, 169 K, compared with other noble gases, such as Argon which has a boiling point of 87.26 K [56, 62]. Because it is easier to cool the liquid, this high boiling point allows for the use of a more basic detector system, based on a cryogenic system and a nitrogen cooling bath [22].

Liquid Xenon is also highly scalable as a detector medium, which implies that the size of the detector can be increased continually, as long as the the integrity of the detector remains intact and additional target material is available [25]. This is an advantage, because the sensitivity scales with the volume of the detector, while most of the backgrounds come from the detector materials and its event rate scales with the area of the detector's surface [4, 28, 63]. Most of the backgrounds are located in the surface of the detector, and they don't reach the detector's core due to the xenon self-shielding properties [4]. As a noble gas, Argon is also very scalable, but this is not the case for Germanium as a detector medium [64]. The detector's that use Germanium as a target build its tonne-scale, producing an array of many small Germanium crystals [65]. Above $\sim$ 1 kg mass, these crystals have diminishing returns due to heat capacity and cost. In addition to these constraints, each crystal adds background to the detector, mainly in its support structures and readout interfaces. The addition of more Germanium crystals above 1 kg mass will also affect the energy resolution of the experiment, causing difficulties in the measurement of the phonon signal.

2.2 Scintillation and Ionization yields

The energy depositions caused by the particle interactions in the detector's target can be characterised by two different types of recoils: nuclear recoil, NR, or electronic recoil, ER [8, 18, 23]. Nuclear recoils, NR, are the result from interactions with the target atom nuclei [8]. The atom nuclei can interact with hypothetical Dark Matter particles or neutrons [23]. For electronic recoils, ER, the interactions in the target result from interactions with the electrons of the target atoms [8]. These electrons interact with typical backgrounds of the detector, as γs and β particles [23]. For both ER and NR, the energy deposited in the detector is converted to ionization, atomic excitation and heat [23]. This energy deposition is described by the Platzman equation, given by [61, 66]

$$E_0 = N_i\, E_i + N_{ex}\, E_{ex} + N_i\, \epsilon\,, \tag{2.1}$$

where E_i is the mean energy that is spent to ionize an atom, E_{ex} is the mean energy that is spent to excite an atom, N_i is the mean number of ionized atoms, N_{ex} is the mean number of excited atoms, and ϵ is the mean energy of sub-excitation electrons, [61]. In the equation 2.1, the term $N_i\epsilon$ corresponds to the heat, which is more relevant in a NR than an ER energy deposition [67]. The mean number of ionized and excited atoms are given in terms of its work functions, W_i and W_{ex}, as [66]

$$N_i = \frac{E_{dep}}{\alpha W_{ex} + W_i} \quad \text{and} \tag{2.2}$$

$$N_{ex} = \alpha N_i \tag{2.3}$$

where α is the relation between the number of excited atoms and ionized ones [66]. This relation is approximately 0.06 for ER and 1 for NR [67].

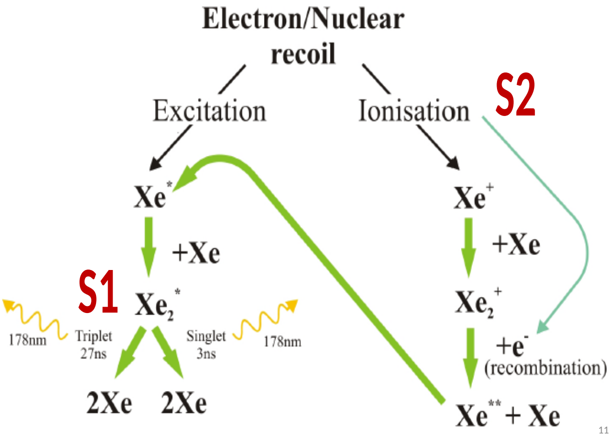

Figure 2.1: Response mechanism of dual phase Time Projection Chamber [68].

Both excitation and ionization can produce primary scintillation through the following process, known as scintillation mechanism [69]:

$$\begin{aligned} \mathrm{Xe}^{*} + \mathrm{Xe} &\rightarrow \mathrm{Xe}_2^{*} \\ &\rightarrow \mathrm{Xe} + \mathrm{Xe} + \gamma\,, \end{aligned} \tag{2.4}$$

$$\begin{aligned} \mathrm{Xe}^{+} + \mathrm{Xe} &\rightarrow \mathrm{Xe}_2^{+} \\ \mathrm{Xe}_2^{+} + e^{-} &\rightarrow \mathrm{Xe}^{**} + \mathrm{Xe} \\ \mathrm{Xe}^{**}\& &\rightarrow \mathrm{Xe}^{*} + \mathrm{heat} \\ \mathrm{Xe}^{*} + \mathrm{Xe} &\rightarrow \mathrm{Xe}_2^{*} \\ &\rightarrow \mathrm{Xe} + \mathrm{Xe} + \gamma\,. \end{aligned} \tag{2.5}$$

The figure 2.1 shows a simplified scheme of the interaction chain in xenon [68]. The incident ionizing radiation produces both excitation and ionization xenon atoms [8].

The initial excitation of xenon atoms results on the production of light emitted through the decay of excited diatomic molecules of xenon, Xe_2^{+} [4, 8]. As shown in the equation 2.4, this light is emitted in the form a photons with wavelength of 175 nm, in the VUV region of the electromagnetic spectrum
[4, 69]. This scintillation light corresponds to prompt scintillation or S1 signal [8]. The ionization of xenon atoms corresponds to the formation of free electrons and a positive ion pair, Xe^{+} [4]. Some of the ionization electrons escape the event site, being drifted by an electric field known as drift field [8]. For a very low drift field, the remaining electrons recombine with ionized xenon atoms at the event site. This process is known as recombination, as described by the equations 2.5 [8, 69]. These equations show the formation of ionized molecules, Xe_2^{+} from the ionized channel [69, 70]. Later, the recombination of electrons results in the production of excited xenon excimers, Xe_2^{*}, and scintillation light [8]. This scintillation light is produced as the excited xenon excimers, Xe_2^{*}, return to ground-state neutral pairs of Xenon atoms, Xe_2. In addition to the scintillation light produced by direct excitation, the scintillation light produced from the recombination process also corresponds to the prompt scintillation or S1 signal [8, 23].

However, the free electrons that escape recombination are drifted upwards under the influence of a stronger electric field [23]. Eventually, these electrons are extracted into the gas phase of the detector when they reach the liquid-gas interface.

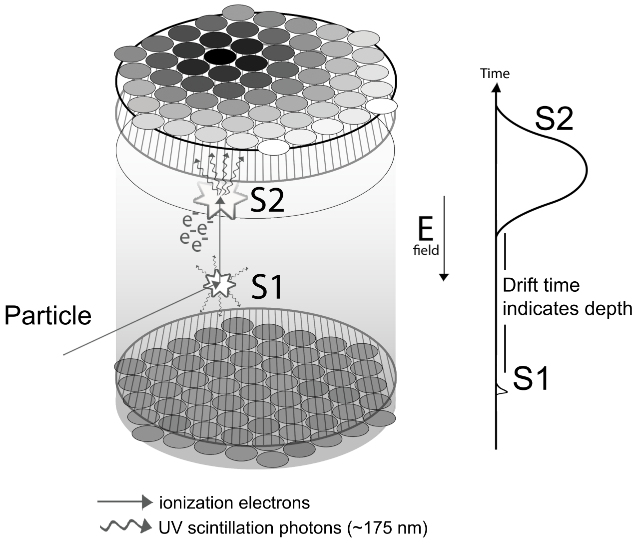

Figure 2.2: Scheme of a dark matter interaction in a dual-phase Time Projection Chamber [53].

During their extraction to the gas phase, the electrons are accelerated, producing a scintillation light known as secondary scintillation light or S2 signal [8, 23].

For short particle tracks, the recombination probability is given by the Thomas-Imel box model as [66]

$$r = 1 - \frac{\ln(1+\xi)}{\xi}, \quad \xi \equiv \frac{N_i \alpha'}{4a^2 v} \tag{2.6}$$

where α' is is a constant dependent on ionization electron and hole mobilities and the dielectric constant, v is the mean ionization electron velocity and a is a length scale defining ionization density volume. As such, the number of photons N_{ph} and the number of ionization electrons N_e are given by

$$N_{ph} = N_{ex} + rN_i \quad \text{and} \tag{2.7}$$

$$N_e = N_i(1-r) \tag{2.8}$$

"Short tracks" are defined to be those that are shorter than the mean ionization electron-ion thermalization distance, 4.6 μm in liquid xenon.

The figure 2.2 shows a scheme of cryogenic dual-phase TPC with a noble gas [29, 53]. As shown in the figure, an incoming particle interacts in the liquid volume, depositing energy either through direct atomic excitation or ionization [21]. The energy deposited through excitation leads to the creation of a dimer in the excited state, which produces primary scintillation or S1 signal [21, 55]. The ionization of xenon atoms produces charge, namely free electrons. These electrons are drifted towards the surface, by applying an electric field in the liquid surface [55]. For a very low electric field, the released electrons recombine with a xenon ion and also produce a prompt scintillation signal [29]. Alternatively, the electrons are extracted to the gas phase, applying another electric field in the surface region. These extracted electrons interact in the gas, producing electroluminescence light or S2 signal. To produce the S2 signal, it is applied another electric field in the surface that separates the gas and liquid phase of the detector, which extracts the electrons to the gas phase [21, 55].

This configuration allows for the calculation of the depth of the interaction, z [29]. This depth is obtained by the difference in the arrival time between the S2 and S1 signal, which corresponds to the time that electrons take to drift upwards in the detector, known as drift time [29, 55]. The depth of interaction is obtained from measurements of the electron drift velocities as a function of the applied field [8].

This scintillation signal also gives the location of the collected charge in the (x,y) plane of the detector, known as (x,y) position [55]. This position is obtained from a pattern analysis of the S2 light distribution in the top PMT array of the detector. Together, the length of the drift time and the collected charge in the (x,y) plane of the detector give a three-dimensional position reconstruction.

The reconstructed energy for electronic recoils (ER) can be written as [55]

$$E(\mathrm{keV_{ee}}) = W \cdot (N_e + N_\gamma) = W \cdot \left(\frac{S1}{g_1} + \frac{S2}{g_2}\right) = W \cdot \left(\frac{S1}{g_1} + \frac{S2}{SE \cdot EE}\right) \tag{2.9}$$

where g_1 and g_2 are the conversion factors between the quanta released at the interaction site and S1, S2 measured signals. EE stands for extraction efficiency, which is the fraction of electrons that promptly cross the liquid-gas interface [54]. For the final operations of the LUX detector, the obtained extraction efficiency was $(73 \pm 4)\%$. SE is the average response on the number of detected photons (phd) from a single extracted electron [55]. The size of a single electron depends on both drift and electron extraction fields, and detector geometry and pressure of the gaseous xenon [28]. For a given single electron size, it can be estimated the number of electrons per deposited energy [21]. From LUX measurements, SE varies between 25.3 and 26.4 phd [16]. To perform the corrections on EE and SE, it was used the source

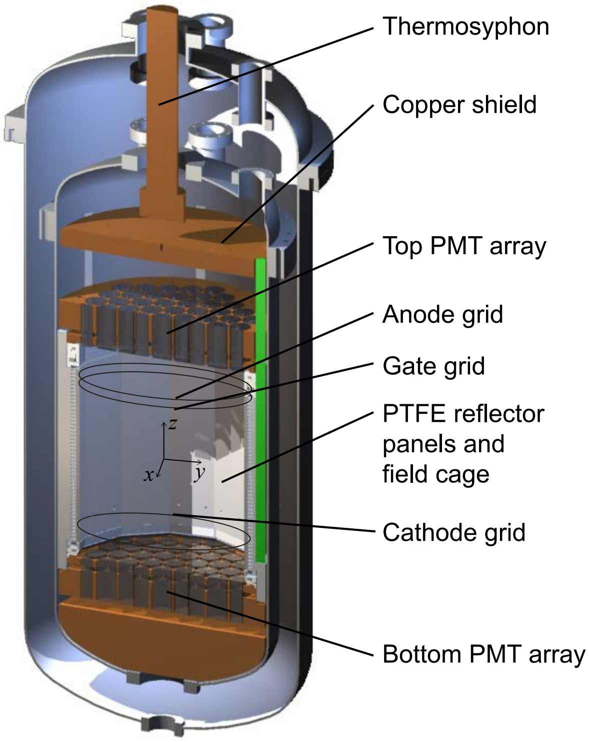

Figure 2.3: Cross sectional view of the LUX cryostats [53].

^{3}H, as described in the section 2.1 [71].

For a nuclear recoil, the reconstructed energy is obtained by dividing the ER reconstructed energy by a quenching factor, L, as [72]

$$E(\mathrm{keV_{nr}}) = \frac{E(\mathrm{keV_{ee}})}{L(\mathrm{keV_{nr}})} \tag{2.10}$$

where the Lindard factor, $L(\mathrm{keV_{nr}})$, determines the fraction of energy of a recoiling nucleus that goes into scintillation and ionization. The dependence of L with the energy is measured using the Deuterim-Deuterim calibrations, as described in the section 2.1.

2.3 The LUX detector

The figure 2.3 shows a scheme of the LUX Time Projection Chmaber, TPC, and the internal and external cryostats [53].

The LUX detector had two cylindrical cryostat vessels that contained the xenon target and detection components [10]. The outer vessel is immersed in a 7.6 m diameter by 6.1 m high water tank [10, 29, 73]. This water tank was used as a shielding from external radiation as cosmic rays from muons, γs and neutrons [29]. The water tank is held by a cryostat with 101 cm tall and a 61.6 cm diameter [10]. The outer vessel also houses the inner vessel, which holds the detector's TPC.

The LUX TPC had an internal maximum diameter of 49 cm, a dodecagonal shape and the inner surfaces of the detector were covered by PTFE Teflon reflector panels [53, 55, 74]. The PTFE panels increased the amount of reflected light events near the TPC walls due to their very good reflectance properties for the Xenon scintillation light. As measured by Neves *et al.* the PTFE reflectance for liquid xenon is about 97 % or more [75].

To detect the S1 and S2 signals, there were used two photomultiplier (PMT) arrays placed in the top and bottom of the volume and each one with 61 Hamamatsu R8778 PMTs [29, 55]. The top PMT array was located in the gas phase of the detector and collects a major fraction of the S2 light, being used for (x,y) position reconstruction [10, 29].

The bottom PMT array was located in the liquid phase of the detector and detects most of the S1 light [29].

In order to have several regions with different electric fields, the LUX TPC included several wire grids at a constant potential and attached to the PTFE pannels [29]. The first grid was located 2 cm above the bottom PMT array. It shielded the PMT's from the high voltage of the cathode [29, 53].

The cathode grid was located 4 cm above the bottom PMT array and operated with a potential of -10 kV [29, 54]. Below the cathode is located the reverse field region. In this region grid the potential decreases, which allows the PMTs to operate near ground [29]. Any interaction that occurs in this region, implies that the electrons drift downwards, not producing an S2 signal.

The gate grid is located 49 cm above the cathode, with a drift field of 180 V/cm in the liquid [29, 72]. This field defined the active region of the TPC, corresponding to the WIMP target [29]. In this region, the gate allows an higher extraction field of $\sim$ 5 kV/cm, that is the field between the gate and the liquid surface [29, 53, 74]. The gate also allows a higher electroluminescence field of $\sim$ 10 kV/cm in the gas region. Between the cathode and the gate, it is applied an electric field that generates the S1 signal [54].

The anode grid is located 1 cm above the gate grid [29]. There is a field between the anode and the top PMT array, which was set to be below the electroluminescence threshold. This low electric field was set that interactions do not produce light in that region of the detector.

The liquid surface is located 5 mm above the gate and 5 mm below anode [4]. Between the anode and the gate, it is created an extraction field that pulls electrons from the liquid surface, generating the S2 signal.

2.4 Calibrations of the LUX detector

Table 2.1: Calibrations operated in the LUX detector for energy and position-dependent corrections.

	Band	Energy (keV)	Type of particle	Used for
^{3}H	ER	0-18	β	Energy calibration
^{14}C	ER	0-12.3	β	Energy calibration
^{83m}Kr	ER	32.1 +9.4	Electron Conversion	Position-dependent corrections
DD	NR	2450	neutrons	Calibrate the NR band
^{127}Cs	ER	0-662	γ	Calibrate the ER band
^{252}Cf	NR	6216.87	neutrons	Calibrate the NR band

For both ER and NR recoils, there were performed several calibrations to understand the response of the detector for different energies and different drift fields [55]. In the table 2.1 are summarised some of these calibrations [23, 28, 33, 76, 77].

ER calibrations were performed during and after the LUX collection data [71]. To perform these calibrations, there were used the sources ^{3}H and ^{14}C. These isotopes are "naked" β emitters, which means that they emit electrons via β decay without any γ emissions [10, 71]. They have endpoint energies of 18.1 keV and 156 keV, and a half-life of 12.3 and 5730 years, respectively [78, 79]. During and after the

LUX collection data, the ^{3}H isotope was used as an internal source that was injected in LUX detector in the form of CH_3T and was removed latter by the getter of the detector [71]. Similarly, the ^{14}C isotope was also injected in the LUX detector in the form of radio-labeled methane, chemically identical to CH_3T. This calibration was performed after the LUX collection data.

NR calibrations were conducted during the LUX operations and using Deuterium-Deuterium as the source of the neutrons [21, 55]. This source is a neutron generator that was located outside the LUX water shield [21]. It emitted neutrons isotropically distributed with an energy of 2.45 MeV. These neutrons were conducted through an air-filled tube in the water tank, between the DD generator and the LUX detector [21, 55]. The emission of neutrons from a Deuterium-Deuterium source is based on a fusion reaction given by [80]

$$^2\mathrm{D} + {}^2\mathrm{D} \rightarrow {}^3\mathrm{He} \; + \mathrm{n}\ . \tag{2.11}$$

This reaction described by the equation 2.11 can produce multiple scatter neutrons. One advantage of double scatter events is that we can measure the scattering angle, θ, of the first recoil using the position of the two scatters, as shown in detail on Akerib *et al.* [81]. From that we can obtain the energy deposited in the first scatter, E_{nr}, given by [4, 81]

$$E_{\mathrm{nr}} = E_n \frac{4m_n m_{\mathrm{Xe}}}{(m_n + m_{\mathrm{Xe}})^2} \frac{1-\cos\theta}{2}\,, \tag{2.12}$$

where E_r is the energy deposited at the first recoil, E_n is the energy of the incident neutron, m_n is the mass of the neutron and m_{Xe} is the mass of the Xenon atom [4].

An example of other source of neutrons used in LUX calibrations is ^{252}Cf [76, 77]. ^{252}Cf is an emitter of neutrons by spontaneous fission, with a probability of emission of 81.7 %, and a Q-value of 6216.87 keV [77].

To reconstruct the positions of the detector, it was used the $^{83\mathrm{m}}$Kr, a metastable isotope, as a calibration source [55]. As shown in the figure 2.4, this source is produced from the parent isotope ,^{83}Rb, β decay [82, 83]. ^{83}Rb decays with an energy of and half-life of 86.2 days.

After the first decay, $^{83\mathrm{m}}$Kr can decay to ^{83}Kr with a total energy release of 41.5 keV [21, 84]. This decay is an internal conversion two stage process, which have

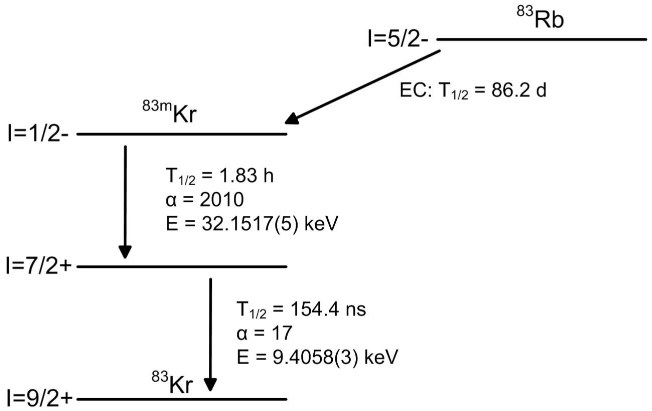

Figure 2.4: Simplified decay scheme of ^{83}Rb to ^{83}Kr. ^{83}Rb decays to $^{83\mathrm{m}}$Kr, which further decays via two transitions to ^{83}Kr [82].

a first transition of 32.1 keV with an half-life of 1.83 hours, followed by a 9.4 keV transition with an half-life of 154 ns [21, 84].

$^{83\mathrm{m}}$Kr was used as calibration source because it can be considered a monoenergetic source for most of practical uses, which allows the correction of both S1 and S2 signal differences in the light collection [55]. This source also allows position reconstruction, which is a necessary step to generate light response functions.

Some external calibration sources have also been used in LUX, such as the mono-noenergectic source ^{137}Cs with 662 keV γ rays [19, 76]. These γ ray sources are placed in the tubes of the detector to calibrate the electron recoil response, to the illumination of the walls for position reconstruction and studies on background modeling [33] . However some issues on getting many single scatters in the fiducial volume are caused by the self shielding of the xenon in the detector, being deployed a calibration source in the xenon itself [19].

2.5 NEST response model

To obtain the response model for the ER and NR recoils, it was used the software package "Noble Element Simulation Technique", NEST [66]. NEST is a set of libraries for use with Geant4 and it was developed to simulate the scintillation, recombination and electroluminescence properties of particle-Xenon interactions [21].

NEST used a detector model for the LUX operations that occurred between April and August, 2013, namely the Run III [54, 66]. During this run, it was observed a mostly-uniform distribution on the electric field of the detector [19, 55].

Alternatively, NEST used 16 different detector models during the LUX operations that occurred between September 11th, 2014 and May 2nd, 2016, namely the Run IV [54]. During these operations, it was observed a non-uniform electric field, which had a dependence on the drift time and the strength was increasing during the run [55, 85]. This dependence was caused by an effect of electrically charging the active volume's PTFE walls during the preparations for the Run IV operations [19, 85]. This effect happened when VUV photons induced electron-hole pairs in the PTFE [19]. Under an applied electric field, the electrons on the PTFE are less mobile than holes, causing the production of a negative charge.

The drift field dependencies were included in the analysis by dividing the complete Run IV exposure into 16 ”exposure segments”, each one with a constant and uniform field magnitude [54]. From these segments, four of them corresponded to different time acquisition periods, known as time bins [55]. The time bins boundaries occurred in September 11th, 2014, January 1st, 2015, April 1st, 2015, October 1st, 2015 and May 2nd, 2016 [54, 55]. Also, each of these time bins were divided into four equal bins in drift time with 40, 105, 170, 235 and 300 μs as boundaries in the drift time values.

In terms of the drift time, the fiducial volume is defined between 40 and 300 μs [54]. Also, its radial boundary is 3.0 cm from the PTFE surface position for the four time bins, in terms of their S2 coordinates x_{S2}, y_{S2}, z_{S2}. Because of a radial dependence on the electric field, these coordinates differ from the S1 signal coordinates, originated by the positions of energy depositions in the detector.

To obtain the mass of the fiducial volume, the 250 kg of active volume of liquid Xenon were scaled by the acceptance fraction of $^{83\mathrm{m}}$Kr events. For the four date bins, the obtained time-averaged fiducial masses were 105.4, 107.2, 99.2 and 98.4 kg, respectively.

A fifth time bin was also used in NEST ER/NR calibrations, which corresponded to ^{14}C calibrations that occurred in August 2016, after the Run IV operations were finished [19].

Chapter 3

Magnetic Inelastic Dark Matter

In this chapter, we will present a theoretical approach for inelastic Dark Matter (iDM) and Magnetic inelastic Dark Matter (MiDM) [2, 3]. We will also build a signal model for Magnetic inelastic Dark Matter, using LUX data [55, 86]. From this signal model, we will compare our results with the ones obtained by other authors for the same model [2, 86].

3.1 inelastic Dark Matter (iDM)

In most of the Dark Matter searches, the WIMP is assumed to scatter elastically with the atomic nuclei [87]. This approach is based on a conservation of momentum and kinetic energy between the incident particle and the target nuclei [88]. Nonetheless, DAMA's discrepancies with other dark matter experiments might be addressed by a change from elastic to inelastic kinematics approach [3]. In this case, the incident particle loses kinetic energy when interacting with the target nuclei [89]. This approach leads to the spectrum being dramatically changed, allowing a signal at DAMA and suppressing or eliminating the signals at sufficiently low recoil energies for other dark matter experiments [3, 90]. This change in the kinematics results in a spectrum which can peak at 20 keV$_{nr}$ or above [90]. This approach also enhances significantly the annual modulation of the signal [3, 90]. Comparing with the elastic kinematics approach, the annual modulation can be much higher for inelastic Dark Matter [90]. This difference is explained by sampling a higher velocity component of the hypothesised Dark Matter particle velocity distribution for inelastic Dark

Matter. Other of the changes caused by this kinematic modification consists on on heavier targets being favoured over lighter targets [3, 90]. It will be shown further below, that an inelastic scattering approach allows a greater range for heavier target nuclei than for lighter target nuclei [90].

The inelastic scattering between the dark matter particle, χ_1, and a nucleus, N, is represented in the figure 3.1, where χ_2 is the dark matter particle in an excited state, q is the transfer momentum between χ_1 and χ_2 and $\delta = m_{\chi_2} - m_{\chi_1}$ is the mass splitting between the excited state dark matter particle (m_{χ_2}) and the dark matter ground state (m_{χ_1}) [86, 91].

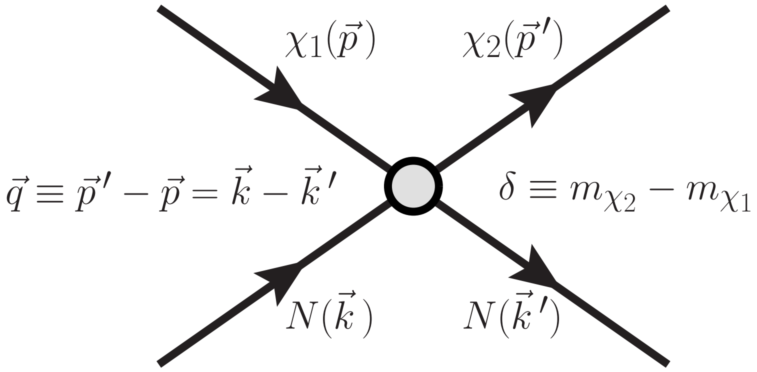

Figure 3.1: Inelastic Dark Matter scattering off of a nucleon [86].

For both elastic and inelastic scattering, the general expression for the differential scattering rate, $\frac{dR}{dE_R}$, of a WIMP-nucleus system is given by [91]

$$\frac{dR}{dE_R} = \frac{\rho_{\chi_1}}{m_{\chi_1}} \frac{1}{m_N} \int_{v_{min}}^{\infty} v f_{\oplus}(\vec{v}, \vec{v}_e) \frac{d\sigma}{dE_R} d^3 v, \tag{3.1}$$

where E_R is the recoil energy of the nucleus, m_{χ_1} is the mass of the hypothesised DM particle, ρ_{χ_1} is the local dark matter density, m_N is the mass of the target nuclei, $f_{\oplus}(\vec{v}, \vec{v}_e)$ is the local dark matter velocity distribution in the detector rest frame, $|v| \equiv |\vec{v}|$ is the WIMP's velocity and $\vec{v}_e = 232$ km/s is the Earth's average velocity relative to the galactic frame, $\frac{d\sigma}{dE_R}$ is the differential cross-section of the WIMP-nucleus system and v_{min} is the minimum velocity required for a DM particle to deposit energy in the detector [25, 91].

The miminum velocity, v_{min}, is derived from the energy conservation condition, as shown in Barello *et al.* [86]. This condition requires that

$$\delta + \vec{v} \cdot \vec{q} + \frac{|\vec{q}|^2}{2\mu_N} = 0, \tag{3.2}$$

leading to

$$|\vec{v}| \geq \frac{1}{|\vec{q}|}\left|\frac{|\vec{q}|^2}{2\mu_N}+\delta\right|. \tag{3.3}$$

From the condition defined on 3.3, it is possible to write the minimum velocity, v_{min}, in terms of the energy recoil. If we consider that $|\vec{q}| = \sqrt{2m_N E_R}$, we get v_{min} in its standard form, given by

$$v_{min} = \sqrt{\frac{1}{2m_N E_R}}\left|\frac{m_N E_R}{u_{\chi_1 N}}+\delta\right| \tag{3.4}$$

where $u_{\chi_1 N} \equiv m_{\chi_1} m_N/(m_{\chi_1}+m_N)$ is the reduced mass of the DM-nucleus system [43]. The interaction between the nucleus and the target is elastic for $\delta = 0$. Otherwise, it follows an inelastic scattering kinematics approach [43].

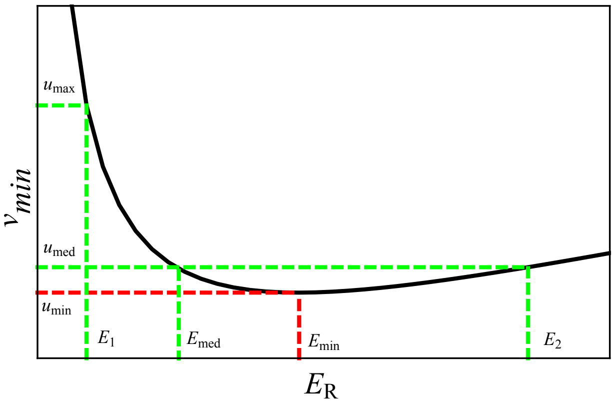

Figure 3.2: WIMP-nucleus scattering minimum velocity as a function of the nuclear recoil energy [92].

Figure 3.2 describes the minimum velocity required for a dark matter particle (χ_1) to scatter with a target nucleus as a function of the recoil energy [92]. It shows that each value of the nuclear recoil energy (E_R) corresponds to a minimum velocity (v_{min}) value. However, it also shows that the v_{min} values don't always correspond to the E_R values. Some of the v_{min} values can correspond to two or none of the E_R values.

For the local Dark Matter velocity distribution, we considered the Standard Halo Model (SHM) [91]. This model describes a dark matter halo with an isotropic and isothermal spherical distribution. From this distribution, it was considered that the rotation curve of the dark matter halo is approximately flat at large radii, as observed in the Milky way [93]. This model is mainly characterized by two quantities: local dark matter density, ρ_{χ_1}, and the velocity distribution in the galactic frame, $f(\vec{v})$ [25]. SHM has a local dark matter density of 0.3 GeV/cm^3 and follows a Maxwellian distribution in the galactic frame, given by [76, 91].

$$f(\vec{v}) = \begin{cases} \frac{1}{N}\left(e^{-v^2/v_\odot^2} - e^{-v_{esc}^2/v_\odot^2}\right) & v < v_{esc} \\ 0 & v > v_{esc} \end{cases} \tag{3.5}$$

where N is the normalization factor, $v_\odot = 220$ km/s is the orbital velocity of the Sun about the center of the galaxy and $v_{esc} = 550$ km/s is the galactic escape velocity that truncates the SHM velocity distribution [2, 25, 91].

SHM also assumes that the relation between the local dark matter velocity distribution in the detector rest frame $f_\oplus(\vec{v}, \vec{v}_e)$, is related to the Maxwell-Boltzmann distribution in the galactic frame $f(\vec{v} + \vec{v}_e)$, by $f_\oplus(\vec{v}, \vec{v}_e) = f(\vec{v} + \vec{v}_e)$.

3.2 MiDM signal model

Magnetic inelastic Dark Matter (MiDM) is based on the same kinematics approach as iDM, but with an extra assumption of a non-zero magnetic moment of the DM particle [3]. This approach was motivated by the large magnetic moment of the Iodine which is the target nuclei of the DAMA experiment.

The magnetic properties of a detector target are characterised by the weighted dipole moment ($\bar{\mu}$) [3]

$$\bar{\mu} = \left(\sum_{\text{isotope}} f_i \mu_i^2 \frac{S_i + 1}{S_i}\right)^{1/2}, \tag{3.6}$$

where f_i is the isotope abundance, μ_i is the nuclear magnetic moment of the isotope, and S_i is its spin. Figure 3.3 compares dipole moments with different elements atomic mass [3]. As shown, Iodine has a larger magnetic momentum compared to other heavy nuclei, such as Xenon [20]. In this model, the WIMP-nuclei cross section has a dependence on the magnetic momentum of the target. As a consequence, the signal rate of Xe target experiments is suppressed comparing with the one expected from the Iodine target.

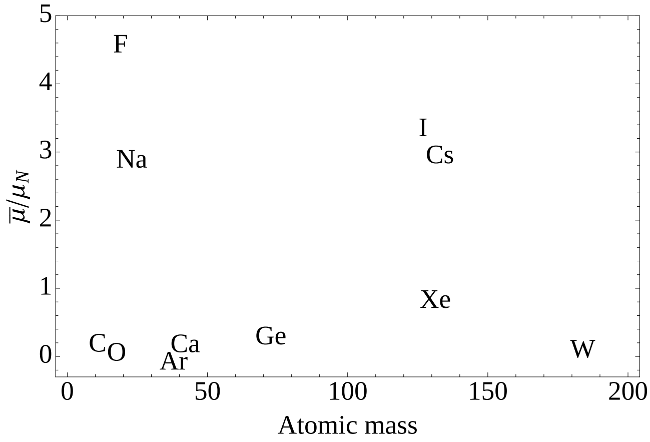

Figure 3.3: Dipole moments for different elements atomic mass in units of the nuclear magneton, μ_N [3].

3.2.1 MiDM differential event rate

For the coupling between dark matter and the standard model through a magnetic moment, it is considered a dark sector that contains a massive gauge field, A'_μ, that mixes kinetically with the photon [94]. For this coupling, the kinetic missing term, $\mathcal{L}_{mix}$ is given by

$$\mathcal{L}_{mix} \supset \epsilon F'_{\mu\nu} F^{\mu\nu}, \tag{3.7}$$

where ϵ is the kinetic mixing parameter, and $F_{\mu\nu}$ and $F'_{\mu\nu}$ are the field strengths for the Standard Model photon and dark sector photon or "dark photon", respectively [95]. The equation 3.7 describes the interaction of the dark matter particle, χ_1, with the gauge field, A'_μ is through a magnetic moment interaction [94].

In the non-relativistic limit, the magnetic moment interaction is a coupling between the χ spin $\vec{S}_\chi$ and the dark magnetic field $\vec{B}' = \vec{\nabla} \times \vec{A}$, as

$$\mathcal{L} \supset 2 m_\chi \mu_{\mathrm{DM}} \frac{\vec{S}_\chi}{|S_\chi|} \cdot \vec{B}'. \tag{3.8}$$

MiDM is based on an inelastic coupling between dark matter and the standard model through a magnetic moment [94, 96]. The MiDM lagrangian is defined by a naturally off-diagonal operator, Majorana fermion, that mediates the transitions between the WIMP ground state, χ_1, and its excited state, χ_2 [3, 97]. The MiDM interaction lagrangian is given by

$$\mathcal{L}_{\mathrm{dipole}} = \frac{\mu_{\chi_1}}{2} \bar{\chi}_2 \sigma_{\mu\nu} F^{\mu\nu} \chi_1 + \mathrm{h.c.}, \tag{3.9}$$

where μ_{χ_1} is the magnetic dipole strength, $\sigma_{\mu\nu} = i[\gamma_\mu, \gamma_\nu]/2$ is a commutator of two Dirac matrices and $F^{\mu\nu}$ is the electromagnetic field-strength tensor.

The MiDM interaction lagrangian is also described as a function of the electromagnetic current j^μ_{EM}. Integrating out the massive A'_μ, the interaction between χ_1 and χ_2, and standard model matter [3, 94]

$$\mathcal{L} \supset \frac{\epsilon \mu_{\mathrm{DM}} e}{2m_A^2} (\bar{\chi}_2 i\sigma^{\mu\alpha} q_\alpha \chi_1) j^\mu_{\mathrm{EM}}, \tag{3.10}$$

The electromagnetic current, j^μ_{EM}, is decomposed in terms of the Gordon's identity, as [94, 98]

$$j^\mu_{\mathrm{EM}} = \bar{p}(k') \left(\frac{(k+k')^\mu}{2m_N} + \frac{g_p}{2} \frac{i\sigma^{\mu\nu} q_\nu}{2m_N} \right) p(k) + \bar{n}(k') \left(\frac{g_n}{2} \frac{i\sigma^{\mu\nu} q_\nu}{2m_N} \right) n(k), \tag{3.11}$$

where the Gordon's identity is given by [98]

$$\bar{N}(k') \left(\frac{(k+k')^\mu}{2m_N} + \frac{g_p}{2} \frac{i\sigma^{\mu\nu} q_\nu}{2m_N} \right) p(N) \tag{3.12}$$

where $N = n, p$ are the nucleon particles, protons and neutrons, respectively.

The electromagnetic current is split in two interactions [94, 99]. From the first term of Gordon's identity, it is given the coupling between the nuclear momentum and the photon through a current-like interaction, known as dipole-nuclear interaction. [3, 98, 99]. The inelastic dipole-nuclear interactions, DZ, were considered by E. Masso *et al.* to explain DAMA's results [100]. However, these interactions doesn't change significantly the relative strength of the various experiments compared with charge-charge interactions [3]. The second term of Gordon's identity gives the dipole-dipole interaction terms, which couples the nuclear momentum to the photon in a dipole-like interaction. In Chang *et al.* it was assumed that DAMA results can be explained both by dipole-charge and dipole-dipole interactions [3].

From a general perspective, the differential cross section, $\frac{\mathrm{d}\sigma}{\mathrm{d}E_R}$, is given by [98, 101]

$$\frac{\mathrm{d}\sigma}{\mathrm{d}E_R} = \frac{1}{32\pi v^2} \frac{1}{m_{\chi_1}^2 m_N} \frac{1}{2S_{\chi_1}+1} \frac{1}{2S_N+1} \sum_{\mathrm{spins}} |\mathcal{M}|^2, \tag{3.13}$$

where $|\mathcal{M}|$ is the WIMP-nucleus scattering amplitude and $S_{\chi_1} = 1/2$ and S_N are the spins of the WIMP and the nucleus.

For MiDM, the equation 3.13 can be decomposed as the sum of two interaction components, as [97, 3]

$$\frac{d\sigma}{dE_R} = \frac{d\sigma_{DD}}{dE_R} + \frac{d\sigma_{DZ}}{dE_R}, \tag{3.14}$$

where $\frac{d\sigma_{DD}}{dE_R}$ is the differential cross-section for dipole-dipole interactions and $\frac{d\sigma_{DZ}}{dE_R}$ is the differential cross-section for dipole-nuclear interactions. For DAMA's Iodine target, the dipole-dipole cross section is dominant over dipole-nuclear scattering, which is the opposite compared with other targets as Xenon, used in XENONnT, LUX and LZ experiments [1, 53].

From the equations 3.13 and 3.14, we can derive the differential cross-sections for dipole-dipole, $\frac{\mathrm{d}\sigma_{DD}}{\mathrm{d}E_R}$, and dipole-current, $\frac{\mathrm{d}\sigma_{DZ}}{\mathrm{d}E_R}$, interactions [1]. From these derivations, the dipole-dipole (DD) differential cross-section is given by [3, 97]

$$\begin{aligned} \frac{\mathrm{d}\sigma_{DD}}{\mathrm{d}E_R} = \frac{16\pi\alpha^2 m_N}{v^2}\left(\frac{\mu_i}{e}\right)^2\left(\frac{\mu_{\chi_1}}{e}\right)^2\left(\frac{S_{\chi_1}+1}{3S_{\chi_1}}\right) \\ \times\left(\frac{S_N+1}{3S_N}\right)F_D^2(E_R), \end{aligned} \tag{3.15}$$

and the dipole-current (DZ) differential cross section given by

$$\begin{aligned} \frac{\mathrm{d}\sigma_{DZ}}{\mathrm{d}E_R} = \frac{4\pi Z^2\alpha^2}{E_R}\left(\frac{\mu_{\chi_1}}{e}\right)^2\Bigg[1 - \frac{E_R}{v^2}\left(\frac{1}{2m_N}+\frac{1}{m_{\chi_1}}\right) - \frac{\delta}{v^2} \\ \times\left(\frac{1}{\mu_{\chi_1 N}}+\frac{\delta}{2m_N E_R}\right)\left(\frac{S_{\chi_1}+1}{3S_{\chi_1}}\right)\Bigg]F^2(E_R). \end{aligned} \tag{3.16}$$

where v is the velocity of the incoming WIMP, Z is the atomic number of the target nucleus, μ_{χ_1} is the WIMP magnetic moment and m_N and μ_{nuc} are the nucleus mass and magnetic moment. $F^2(E_R)$ is the nuclear form factor and $F_D^2(E_R)$ is the nuclear magnetic dipole form factor.

To calculate the differential cross-section, we noticed that the expressions 3.15 and 3.16 have different velocity dependencies, namely $1/v^2$ and v independent [102, 103]. As such, the MiDM differential cross-section can be described by a Maclaurin series as [104]

$$d\sigma \sim \frac{1}{v_r^2}d\{\sigma_-\} + d\{\sigma_+\} \ , \tag{3.17}$$

where $v_r = |\vec{v}_r| = |\vec{v} - \vec{v}_e|$ is the relative velocity, σ_+ corresponds to the factors from equations 3.15 and 3.16 that are multiplied by $1/v_r^2$ and σ_- corresponds to the to the factors without velocity dependencies.

This series expansion can also be used to obtain the differential event rate [102, 103]. The MiDM event rate was obtained by performing the velocity integrals for $1/v^2$ (η_0) and v independent cases (η_1). The MiDM event rate is given by [102, 104]

$$\frac{dR}{dE_R} = \frac{\rho_{\chi_1}}{m_{\chi_1}} \frac{1}{m_N} \left[\frac{d\{\sigma_-\}}{\mathrm{d}E_R} \frac{1}{v_0} \eta_0 + \frac{d\{\sigma_+\}}{\mathrm{d}E_R} v_0 \eta_1 \right] \tag{3.18}$$

where the generalized definition of the velocity integral,$\eta_n(\vec{v} + \vec{v}_e)$, is given by [102]

$$\eta_n(\vec{v} + \vec{v}_e) \equiv \int_{v_{min}} v^{2n} \frac{f(\vec{v} + \vec{v}_e)}{v} \, \mathrm{d}^3 v \ . \tag{3.19}$$

The η_0 is the only velocity integral used to calculate the event rate for elastic scattering [103]. This velocity integral is given by [102]

$$\eta_0(\vec{v} + \vec{v}_e) \equiv \int_{v_{min}} \frac{f(\vec{v} + \vec{v}_e)}{v} \, d^3 v \ . \tag{3.20}$$

The η_n velocity integral was simplified after some algebraic manipulation and can be decomposed in terms of η_0 [102]. It is given by

$$\eta_n(\vec{v} + \vec{v}_e) = v_{min}^{2n} \eta_0(\vec{v} + \vec{v}_e) + 2n \int_{v_{min}}^{\infty} v^{2n-1} \eta_0(f(\vec{v} + \vec{v}_e)) \, \mathrm{d}v \ . \tag{3.21}$$

The η_0 and η_1 integrals are described numerically by [102, 104]

$$\frac{\eta_0}{N} = \frac{v_0}{2v_e} \left[\mathrm{erf}\left(\frac{v_u}{v_\odot}\right) - \mathrm{erf}\left(\frac{v_d}{v_\odot}\right) - \frac{2}{\sqrt{\pi}} \left(\frac{v_u}{v_\odot} - \frac{v_d}{v_\odot}\right) e^{-v_{\mathrm{esc}}^2/v_0^2} \right] ,$$

and

$$\begin{aligned} \frac{\eta_1}{N} = & \left(\frac{v_d}{2v_e\sqrt{\pi}} + \frac{1}{\sqrt{\pi}} \right) e^{-v_d^2/v_\odot^2} - \left(\frac{v_u}{2\vec{v}_e\sqrt{\pi}} - \frac{1}{\sqrt{\pi}} \right) e^{-v_u^2/v_0^2} \\ & + \frac{v_\odot}{4v_E} \left(\frac{1 + 2v_e^2}{v_\odot^2} \right) \left[\mathrm{erf}\left(\frac{v_u}{v_\odot}\right) - \mathrm{erf}\left(\frac{v_d}{v_\odot}\right) \right] \\ & - \frac{1}{\sqrt{\pi}} \left[2 + \frac{1}{3v_e v_\odot^2} \left((v_{\mathrm{min}} + v_{\mathrm{esc}} - v_d)^3 - (v_{\mathrm{min}} + v_{\mathrm{esc}} - v_u)^3 \right) \right] e^{-v_{\mathrm{esc}}^2/v_\odot^2} , \end{aligned}$$

where v_u is given by $v_u = \min(v_{min} + v_e, v_{esc})$ and v_d is given by $v_d = \min(v_{min} - v_e, v_{esc})$.

The differential cross-section components depend on two different form factors: the Helm form factor, $F^2(E_R)$, and the nuclear magnetic dipole form factor, $F_D^2(E_R)$ for the equations 3.16 and 3.15, respectively [3]. Both form factors are calculated using an Effective field theory (EFT) approach, that will be described in a later section of this chapter [98].

3.2.2 Helm form factor

The dipole-current (DZ) differential cross-section (equation 3.16) was calculated using the Helm form factor, $F(q)$ [3]. This form factor is applied to standard spin-independent interactions, that will be defined in the next section [98, 105].

The spin-independent cross section is linearly related to its squared form factor for a momentum transfer different than zero [105]. This nuclear form factor is characterised by a Fourier transform of the mass distribution, equivalent to its charge distribution [43, 106]. It is parametized by

$$F(q) = 3e^{-q^2 s^2/2} \frac{\sin(qr_n) - qr_n \cos(qr_n)}{(qr_n)^3}\,, \tag{3.22}$$

where q is the transfer momentum, $r_n = 1.13A^{1/2}$ is the spin nuclear radius and s it's the nuclear skin thickness [107].

To compute the Helm form factor, we created a python script that built a MiDM signal model using a spin-independent/spin-dependent approach. The results obtained with this script are shown in the figure 3.4. They compare well with the expected values shown in figure 6 from Gresham and Zurek [108].

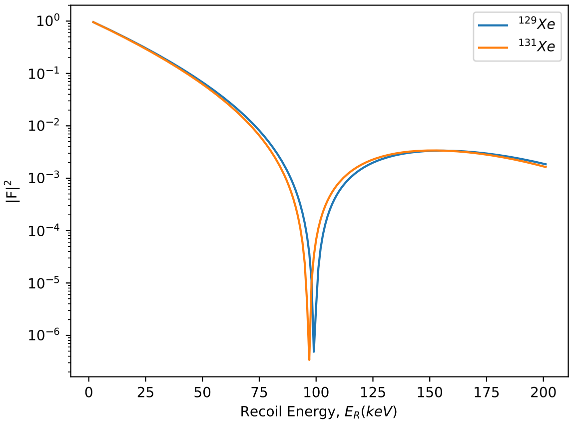

Figure 3.4: Squared helm form-factors as a function of recoil energies.

3.2.3 Magnetic dipole form factor

The dipole-dipole (DD) differential cross-section (equation 3.15) was calculated using the magnetic dipole form factor, $F_D^2(q)$ [3]. From this form factor, there were not found explicit or well documented calculations in the literature. This motivated an approximation on the magnetic dipole form factor made by Chang *et al*. [3]. This approximation consists in weighting the angular momentum and spin contributions to the magnetic dipole moment. For Iodine, the approximation for the magnetic form factor, $F_D^2(q)$ is given by

$$F_D^2[E_R] = \left(0.5\frac{L_{2d}(E_R)}{L_{2d}(0)} + 0.5\sqrt{\frac{S_{pp}(E_R)}{S_{pp}(0)}}\right)^2 \tag{3.23}$$

where $S_{pp}(E_R)$ is proton-only structure factor, $S_{pp}(0)$ is structure factor for a null transfer moment, $L_{2d}(E_R)$ and $L_{2d}(0)$ are the angular momentum contribution for the dipole form factor.

3.2.4 Introduction to Effective Field Theory

EFT is based on a set of WIMP-nucleon operators that are subject of two basic symmetries, conservation of momentum and Galilean invariance [101]. These symmetries are represented by a framework of 16 operators described on detail by Fitzpatrick *et al.* [98]. They are associated with different types of nuclear responses and have their dependencies on: $\vec{v}^{\perp} = \vec{v} + \vec{q}/2u_{N\chi_1}$, where $\vec{v}^{\perp}$ is the relative perpendicular velocity between the WIMP and the nucleon, $\vec{q}$ is the momentum transferred in the scattering event, $\vec{S}_N$ the nucleon spin and $\vec{S}_{\chi_1}$ the spin of the WIMP [109]. From this set of operators, $\mathcal{O}_1$ and $\mathcal{O}_4$ are related to the standard spin-independent/spin dependent (SI/SD) couplings [19]. The SI coupling is described as a scalar coupling in the effective Lagrangian term coupling, while SD coupling is related to an axial coupling between the dark matter particle and quarks in the effective Lagrangian term coupling. The EFT operators $\mathcal{O}_1$ and $\mathcal{O}_4$ are given by

$$\mathcal{O}_1 = \mathbf{1}_{\chi_1}\mathbf{1}_N, \tag{3.24}$$

$$\mathcal{O}_4 = \vec{S}_{\chi_1} \cdot \vec{S}_N. \tag{3.25}$$

For models as iDM and MiDM, the incoming and outgoing WIMPs have different mass states [3, 109]. In this case, the EFT operators are modified in terms of an inelastic perpendicular velocity between the nucleon and the WIMP, $\vec{v}^{\perp}_{inelastic}$ [109]. This velocity is given by

$$\vec{v}^{\perp}_{inelastic} \equiv \vec{v}^{\perp} + \frac{\delta}{|\vec{q}|^2}\vec{q} \tag{3.26}$$

For a set of sixteen basis operators, the WIMP-nucleon interaction is described by [98, 101]

$$\mathcal{L} = \left[\sum_{i=1}^{16} a_i^{(n)}\mathcal{O}_i^{(n)} + a_i^{(p)}\mathcal{O}_i^{(p)}\right], \tag{3.27}$$

where $a_i^{(p)}$ and $a_i^{(n)}$ are the coupling constants for proton and neutrons, respectively, associated with the operator $\mathcal{O}_i$.

For MiDM, the lagrangean given by the equations 3.9 and 3.10 takes the form [94]

$$\begin{aligned}\mathcal{L}_{\text{int}} = \frac{\epsilon\mu_{\chi_1}e}{m_A^2}&[(m_N q^2\mathbf{1} + 4m_N m_{\chi_1} i\vec{S}_{\chi_1}\cdot(\vec{q}\times\vec{v}^{\perp}_{inelastic})\\ &+2g_p m_{\chi_1}(q^2\vec{S}_{\chi_1}\cdot\vec{S}_p - (\vec{q}\cdot\vec{S}_{\chi_1})(\vec{q}\cdot\vec{S}_p)))_{\text{proton}}\\ &+(2g_n m_{\chi_1}(q^2\vec{S}_{\chi_1}\cdot\vec{S}_n - (\vec{q}\cdot\vec{S}_{\chi_1})(\vec{q}\cdot\vec{S}_n)))_{\text{neutron}}]\end{aligned}$$

where $g_p = 5.59$ and $g_n = -3.83$ are the proton and neutron gyro-magnetic factors, respectively [110, 111, 112]. From the equation 3.2.4, the terms that are independent from the the g_n and g_p factors correspond to the dipole-nuclear interactions, while the terms that are dependent from the gyro-magnetic factors correspond to the dipole-dipole interactions [96]. In terms of the equation 3.27, the dipole-charge interaction is due to non-zero coefficients of $\mathcal{O}_1$ and $\mathcal{O}_5$, while the dipole-dipole interaction is through the $\mathcal{O}_4$ and $\mathcal{O}_6$ operators. These EFT operators follow an inelastic kinematics approach, and are given by [86]

$$\begin{aligned}\mathcal{O}_1 &= \mathbf{1}_{\chi_1}\mathbf{1}_N,\\ \mathcal{O}_4 &= \vec{S}_{\chi_1}\cdot\vec{S}_N,\\ \mathcal{O}_5 &= i\vec{S}_{\chi_1}\cdot\left(\frac{\vec{q}}{m_N}\times\vec{v}^{\perp}_{\text{inel}}\right),\\ \mathcal{O}_6 &= \left(\vec{S}_{\chi_1}\cdot\frac{\vec{q}}{m_N}\right)\left(\vec{S}_N\cdot\frac{\vec{q}}{m_N}\right).\end{aligned} \tag{3.28}$$

3.2.5 EFT form factors

From the EFT approach, $F_{ij}^{(N,N')}$ is defined as the EFT form factor [101]. The EFT form factor consists in a linear combination of the nuclear response form factors, $F_{k}^{(N,N')}(q^2)$, and the interference form factors, $F_{k_1,k_2}^{(N,N')}(q^2)$, with k ranging over the nuclear operators, k_1, M, Σ'', Σ', Δ, Φ'' and Φ', and the two interference responses, k_2, (M,Φ'), (Σ', Δ).

M is a spin-independent nuclear response proportional to Z or to (A-Z) for protons and neutrons, respectively. One example of the origin of this nuclear response comes from the scalar interaction that is described by the standard spin-independent operator, $\mathcal{O}_1$, defined in the previous section.

Σ'' and Σ' are related to the spin momentum operator which is proportional to $< S_p >$ or $< S_n >$ the expected proton or neutron spin, respectively. The spin momentum operator was used in the magnetic dipole calculations, described in more detail in the next section [3]. This contribution was obtained from the spin-dependent structure factor calculations [113]. The Structure factor for a transfer momentum different than zero, $S(q)$, is given by [114]

$$S(q) = a_0^2\, S_{00}(q) + a_0 a_1 S_{01}(q) + a_1^2\, S_{11}(q), \tag{3.29}$$

where a_0 is the isoscalar coupling, a_1 is the isovector coupling and S_{00}, S_{01}, S_{11} are the isocalar/isovector structure factors. If $a_0 = a_1 = 1$ the structure factor is defined as ”proton-only” coupling, $S_{pp}(q)$. Similarly, if $a_0 = -a_1 = 1$ the structure factor is defined as ”neutron-only” coupling, $S_{nn}(q)$. The structure factors for proton-only and neutron-only couplings are given by

$$S_{pp}(q) = S_{00}(q) + S_{01}(q) + S_{11}(q),$$
$$S_{nn}(q) = S_{00}(q) - S_{01}(q) + S_{11}(q).$$

Figure 3.5 shows the inelastic spin structure factors as a function of the dimensionless parameter, $u = q^2b^2/2$, where q is the transfer moment and b is the harmonic oscillator length [113].

Δ is the angular-momentum response. It is related to the angular momentum operator, which is proportional to $< L_p >$ or $< L_n >$ the expected proton or neutron angular momentum, respectively.

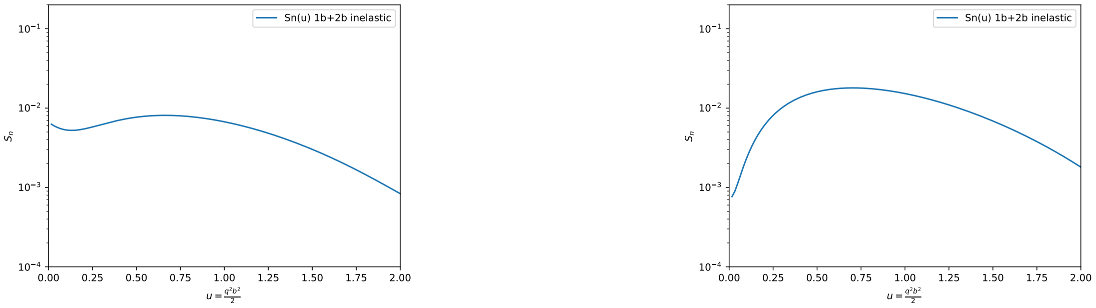

Figure 3.5: $^{129}_{54}$Xe Inelastic Structure Factor (left) and $^{131}_{54}$Xe inelastic structure factor (right). Spin-dependent inelastic structure factors as a function of $u = q^2b^2$, with the transfer moment q and the b the harmonic oscillator length.

Φ'' is the "spin-orbit" coupling (LSD), which is proportional to $< \vec{S_p} \cdot \vec{L_p} >$ and $< \vec{S_n} \cdot \vec{L_n} >$. Φ' is the "spin-orbit" coupling tensor operator (tLSD) that is proportional to Φ'' in the long-wavelength limit.

The form factors, $F_k^{(N,N')}(q^2)$ and $F_{k_1,k_2}^{(N,N')}(q^2)$, are given by

$$F_k^{(N,N')}(q^2) \equiv \frac{4\pi}{2j+1} \sum_{J=0}^{2j+1} \langle j||k_J^{(N)}||j\rangle \langle j||k_J^{(N')}||j\rangle, \tag{3.30}$$

and

$$F_{k_1,k_2}^{(N,N')}(q^2) \equiv \frac{4\pi}{2j+1} \sum_{J=0}^{2j+1} \langle j||k_{1_J}^{(N)}||j\rangle \langle j||k_{2_J}^{(N')}||j\rangle. \tag{3.31}$$

where $(N, N') = (n, n), (n, p), (p, n), (p, p)$ is the explicit sum over the nucleon pairs that takes into account two-body currents in the nucleus. It is possible to numerically calculate the EFT form factors, as shown in Anand *et al.* [101, 115]. With this approach, the form factor for the operators $\mathcal{O}_i$ and $\mathcal{O}_j$ is given by [101]

$$F_{ij}^{(N,N')} = a_{ijk} F_k^{(N,N')} \tag{3.32}$$

where a_{ijk} are coefficients that are simple products of WIMP and nucleon masses and spins, and k ranges over the nuclear operators, k_1, M, Σ'', Σ', Δ, Φ'' and Φ', and the two interference responses, k_2, (M,Φ'), (Σ', Δ).

For MiDM, the lagrangean given by 3.2.4 was normalized in terms of $m_M = \frac{1}{e\mu_{\chi_1}}$ by Barello *et al.* [86]. Written in a four-fermion notation, the MiDM lagrangean is given by

$$\mathcal{L}_{\mathrm{MIDM}} = \frac{1}{q^2}\left[\bar{\chi}_2 i\sigma^{\mu\nu}\frac{q_\nu}{m_M}\chi_1\, \bar{p}\gamma_\mu p\right] + 0.9\frac{m_M}{m_N q^2}\left[\bar{\chi}_2 i\sigma^{\mu\nu}\frac{q_\nu}{m_M}\chi_1\, \bar{p} i\sigma_{\mu\alpha}\frac{q^\alpha}{m_M}p\right]$$
$$- 0.96\frac{m_M}{m_N q^2}\left[\bar{\chi}_2 i\sigma^{\mu\nu}\frac{q_\nu}{m_M}\chi_1\, \bar{n} i\sigma_{\mu\alpha}\frac{q^\alpha}{m_M}n\right].$$

where the relative coefficients set by the proton and neutron magnetic moments are 2.8 and -1.91 nuclear magnetons, μ_N, respectively. In the equation 3.33, the modified inelastic EFT operators are $\mathcal{O}_9$ and $\mathcal{O}_{10}$ in its four-fermion form [86]. They are described by

$$\mathcal{O}_9 = i\vec{S}_\chi \cdot \left(\vec{S}_N \times \frac{\vec{q}}{m_N}\right), \quad \mathcal{O}_{10} = i\vec{S}_N \cdot \frac{\vec{q}}{m_N}. \tag{3.33}$$

where $\mathcal{O}_9$ couples to nucleus through through transverse spin, $\vec{q} \times \vec{\sigma}(i)$ and $\mathcal{O}_{10}$ couples through longitudinal spin, $\vec{q} \cdot \vec{\sigma}(i)$ [115]. For these operators, the form factors are misrepresented, because the transverse and longitudinal couplings are described by distinct form factors

3.3 Differential cross-sections and Event Rates

3.3.1 SI/SD

We obtained the MiDM Event rate using primarily the spin-independent/ spin-dependent approach [113, 105]. After determining the MiDM Event rate, we obtained the MiDM differential cross-section and event rate using the procedure described in the previous sections.

The figure 3.6 shows the differential cross-section of the WIMP-Xenon system as function of the recoil energy (top) and the differential event rate of the WIMP-Xenon system as a function of the recoil energy (bottom). The left figures corresponded to the parameters ($m_{\chi_1} = 122.7$ GeV/c^2, μ_{χ_1}=0.0056 μ_{nuc}, $\delta = 179.3$ keV) [2]. The right figures corresponded to the parameters ($m_{\chi_1} = 58.0$ GeV/c^2, μ_{χ_1}= 0.0018 μ_{nuc}, $\delta = 111.7$ keV) with the nuclear magneton μ_{nuc}. We compared the figures 3.6 (top) with the ones presented on figure 3 from Barello *et al.* and we

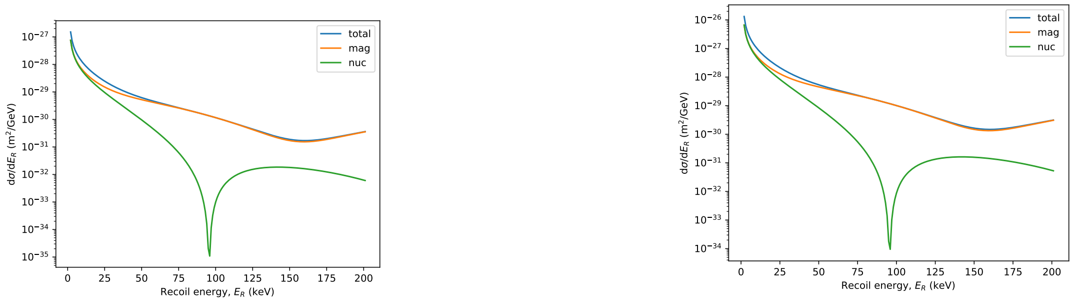

(a) WIMP differential cross section for the parameters ($m_{\chi 1}$ = 122.7 GeV/c^2, $\mu_{\chi 1}$=0.0056 μ_{nuc}, δ = 179.3 keV).

(b) WIMP differential cross section for the parameters ($m_{\chi 1}$ = 58.0 GeV/c^2, $\mu_{\chi 1}$= 0.0018 μ_{nuc}, δ = 111.7 keV).

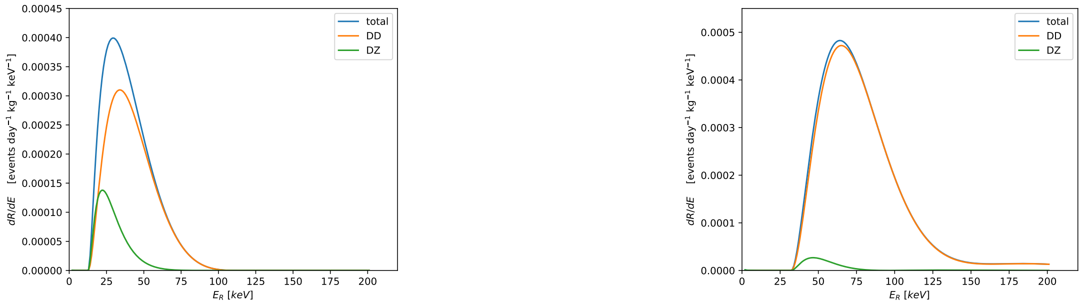

(c) Differential WIMP rate for the parameters ($m_{\chi 1}$ = 122.7 GeV/c^2, $\mu_{\chi 1}$=0.0056 μ_{nuc}, $\delta = 179.3$ keV).

(d) Differential WIMP rate for the parameters ($m_{\chi 1}$ = 58.0 GeV/c^2, $\mu_{\chi 1}$= 0.0018 μ_{nuc}, $\delta = 111.7$ keV).

Figure 3.6: Differential cross-sections and WIMP rates as a function of the nuclear recoil energy.

verified some discrepancies on the obtained normalization factor and on the lower and higher energy limits [86]. These inconsistencies motivated a change from the spin-independent/spin-dependent to the EFT approach [105, 113, 98]. We used the EFT approach, applying a Mathematica package [115] signal model analysis. This analysis will be discussed in more detail in the next section.

3.3.2 inelastic Effective Field Theory signal model

We obtained the signal model for Magnetic Inelastic Dark Matter using the mathematica package "DMFormFactor" created by Anand *et al.* [115]. This package was modified by Barello *et al.* to satisfy the MiDM parameters [86].

The "DMFormFactor" package consists in a set of functions that contribute for the model independent analysis of a direct detection dark matter experiments [98, 115]. This set of functions includes calculation on the differential event rate, $\frac{dR_D}{dE_R}$, and differential cross-section, $\frac{\mathrm{d}\sigma}{\mathrm{d}E_R}$ [115]. The differential event rate, $\frac{dR}{dE_R}$, has a dependence on the differential cross-section, $\frac{\mathrm{d}\sigma}{\mathrm{d}E_R}$, as described by the equation 3.1 [91]. From the "DMFormFactor" package, this equation takes the form [115]

$$\frac{dR}{dE_R} = N_T \left\langle \frac{\rho_{\chi_1}}{m_{\chi_1}} v \frac{d\sigma}{dE_R} \right\rangle \tag{3.34}$$

where the differential cross-section, $\frac{\mathrm{d}\sigma}{\mathrm{d}E_R}$, is unpolarized, as described by the equation 3.13 [101, 116]. This means that the information about the incoming spins is not recorded in the experiment [116]. To allow for scattering in all possible configurations, the equation 3.13 takes the form [115, 116]

$$\frac{\mathrm{d}\sigma}{\mathrm{d}E_R} = \frac{1}{32\pi v^2} \frac{1}{m_{\chi_1}^2 m_N} P_{\mathrm{tot}} \tag{3.35}$$

where P_{tot} is the transition probability density. This probability density represents the total WIMP-nucleus scattering amplitude, being given by [101, 115].

$$P_{\mathrm{tot}} = \frac{1}{2S_{\chi_1}+1} \frac{1}{2S_N+1} \sum_{\mathrm{spins}} |\mathcal{M}|^2_{\mathrm{nucleus-HO/EFT}}, \tag{3.36}$$

where S_N and S_{χ_1} are the incoming spins [115]. The equation 3.36 consists on averaging over the spins of the incoming particles, N and χ_1, and summing over the spins of these particles in the final state [115, 116].

The total WIMP-nucleus scattering amplitude, P_{tot}, consists on the calculation of matrix elements that depend on the the ground state of the atomic nucleus [94, 101]. However, the result of these calculations can be parametized in terms of the form factors of the effective theory operators, $F_{ij}^{(N,N')}(v^2, q^2)$. In the presence of multiple effective interactions, the possible interference terms have a corresponding form factor, resulting in the equation 3.36 to take the form

$$P_{\mathrm{tot}} = \frac{1}{2S_{\chi_1}+1} \frac{1}{2S_N+1} \sum_{\mathrm{spins}} |\mathcal{M}|^2 \equiv \frac{m_N^2}{m_{nuc}^2} \sum_{i,j=1}^{12} \sum_{N,N'=p,n} c_i^{(N)} c_j^{(N')} F_{ij}^{(N,N')}(v^2, q^2), \tag{3.37}$$

where $\frac{m_N^2}{m_{nuc}^2}$ is factored out of the definition of $F_{ij}^{(N,N')}(v^2, q^2)$ for convenience, due to the difference between the relativistic normalization of states for nuclei $\langle k_N | k'_N \rangle =$

$(2\pi)^3(2m_N)\delta^{(3)}(k_N - k'_N)$ and the relativistic normalization of nucleons $\langle k|k'\rangle = (2\pi)^3(2m_{nuc})\delta^{(3)}(k - k')$ [94]. To match the relativistic WIMP-nucleon interaction operators to the corresponding non-relativistic operators, the transition probability density, P_{tot}, is further multiplied in the equation 3.13 by a normalization factor $\frac{1}{(4m_{\chi_1}m_N)^2}$ [101].

Finally, the differential event rate, $\frac{dR}{dE_R}$, can be described in terms of the of the form factors of the effective theory operators, $F_{ij}^{(N,N')}(v^2, q^2)$, as [98]

$$\frac{dR}{dE_R} = N_T \frac{\rho_{\chi_1} m_N}{32\pi m_{\chi_1}^3 m_{nuc}^2} \left\langle \frac{1}{v} \sum_{ij} \sum_{N,N'=p,n} c_i^{(N)} c_j^{(N')} F_{ij}^{(N,N')}(v^2, q^2) \right\rangle, \tag{3.38}$$

where N_T is the number of target nuclei per detector mass.

For the MiDM signal model, we used a modified version of the "DMFormFactor" Mathematica package provided by Barello *et al.* [86, 109]. To build this signal model, we used the MiDM inelastic EFT operators described above and followed the parameters ($\mu_{\chi_1} = 0.0018\mu_N, m_{\chi_1} = 58.0\,GeV, \delta = 111.7\,keV$). We selected these parameters from the two best fit parameters of the DAMA/LIBRA experiment [2].

We calculated the event rate in terms of the MiDM transition probability obtained for each isotope, $\frac{dR_i}{dE_R}$, using the equation 3.38 [98, 115]. Then, we obtained the MiDM total event rate, $\frac{dR}{dE_R}$, from the sum of each isotope event rate, $\frac{dR_i}{dE_R}$, multiplied by its abundance, f_i, as [3]

$$\frac{dR}{dE_R} = \sum_i f_i \frac{dR_i}{dE_R}. \tag{3.39}$$

Detector response for the signal model

We used the curves for the differential rate obtained in the Mathematica script to get the detector response for the parameters ($\mu_{\chi_1} = 0.0018\,\mu_{nuc}$, $m_{\chi_1} = 58.0$ GeV/c^2, $\delta = 111.7$ keV) [2, 115]. As one of the best fit values the DAMA/LIBRA experiment, these parameters were used by Aprile *et al.* for MiDM event rate calculations [2]. We also used them for MiDM event rate calculations, comparing our results with the calculations performed by Aprile *et al.*

To get the expected S1 and S2 signals, we used the NEST software package described in the previous chapter [66]. NEST generated the interaction of the WIMP with the nucleus – a nuclear recoil (NR), and the interaction of the γ generated by de-excitation of χ_2. The γs interact in the liquid mainly via photoelectric effect or Compton scattering. We discarded the Compton scattering from our analysis, because we will simulate only one energy peak. Together with the low energies of the γs considered in this work (lower than 800 keV), this results on the photoelectric effect being dominant. The electron generated by the photoelectric effect interacts in the detector, causing an electronic recoil, ER.

The NEST software does not include the MiDM spectra as a signal. Therefore, we generated the detector response for the NR energy deposition, using a uniform distribution between 0 and 500 keV. We applied a Monte Carlo acception-rejection method to this data, using an uniform distribution according to MiDM. The data obtained from this method (histogram) and the results for the Mathematica script (blue line) are shown in figure 3.7 for the differential event rate with the parameters $(\mu_{\chi_1}, m_{\chi_1}, \delta)$ specified above.

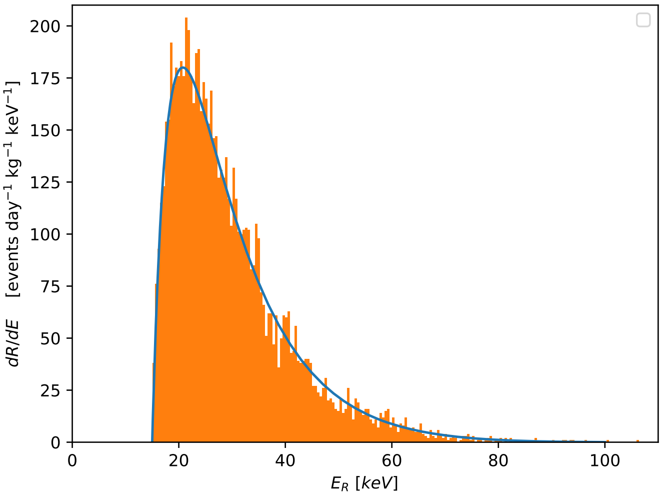

Figure 3.7: Event rate histogram for the parameters (μ_{χ_1}= 0.0018 μ_{nuc}, m_{χ_1} = 58.0 GeV/c^2, δ = 111.7 keV).

For both NR and ER, we used NEST to generate the detector response for each data bin and drift time bin [72]. Both the data binning and drift time binning were described in the previous chapter [54, 55].

The figure 3.8 shows the signal model results for the nuclear recoil. The blue and cyan lines represent the ER band mean obtained for the top and the bottom of the detector, respectively [54, 72]. The NR band mean was also taken from this data bin, and is represented by the filled red curve and the 80 % contours represented by the dashed red curves from the figure 3.8.

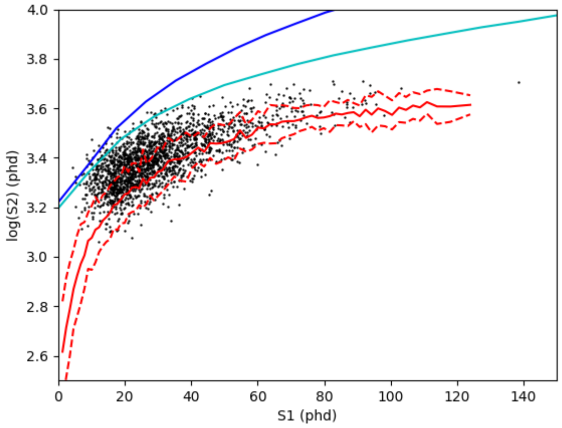

Figure 3.8: Distribution of the nuclear recoil signal generated by the MiDM as a function of S1 signal for the top (blue) and for the bottom of the detector (cyan), with drift bins of 40-105 μs and 235-300 μs, respectively.

The response of the detector for the γ decay is shown in the figure 3.9. Both blue and cyan lines represent the ER band mean obtained from ^{14}C calibrations acquired after the end of LUX operations [11, 19]. They represent two different depth bins that correspond to the top and bottom regions of the detector, respectively [54, 72].

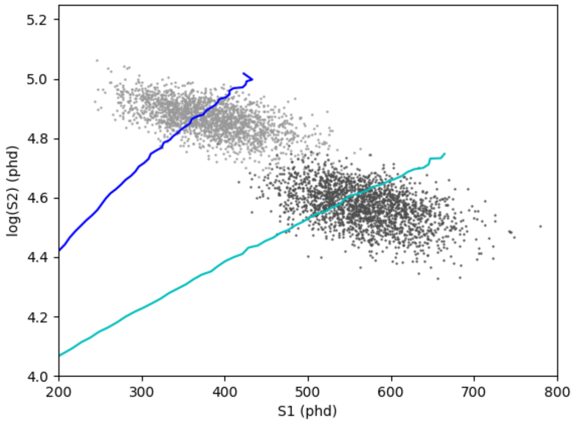

Figure 3.9: ER bands as a function of S1 signal at the end of LUX. Blue: ER mean band for the top of the detector (40-105 μs); Cyan: ER mean band for the detector's bottom (235-300 μs).

Limit on the WIMP magnetic moment

The MiDM signal is composed both by nuclear and electronic energy recoils and, as such, it would be very difficult to be mimetized by a background. In this conditions, it is expected that the background condition would be negligible. As described by Feldman and Cousins, the no background limit on the number of events is 2.44 at a 90 % Confidence Level [117]. A more detailed analysis on the MiDM background sources will be discussed in the next chapter of this thesis.

There is a direct correlation between the differential cross-section, $\frac{d\sigma}{dE_R}$, and the squared magnetic moment of the WIMP, $\mu^2_{\chi_1}$, as shown in the equations 3.15 and 3.16, which is described by

$$\frac{dR}{dE_R} \propto \mu^2_{\chi_1} \tag{3.40}$$

We verified this relation using the modified "DMFormFactor" package with MiDM parameters [86]. From a set of μ_{χ_1} values, we evaluated a maximum event rate value that corresponded to each of these μ_{χ_1} values. From this evaluation, we verified and proved the relation present in the equation 3.40.

The correlation between the event rate and μ_{χ_1} means that setting a limit to the differential event rate is equivalent to set a limit on $\mu^2_{\chi_1}$. The squared WIMP magnetic moment limit, $\mu^2_{\chi_{1limit}}$, is given by

$$\mu^2_{\chi_{1limit}} = \frac{2.44}{T}\mu^2_{\chi_1} \tag{3.41}$$

where $\mu_{\chi_1} = 0.0018\mu_N$ is the WIMP magnetic moment for a mass splitting, $\delta = 111.7$ keV [2, 117]. T is the total number of observed events in the detector for the signal of a specific μ_{χ_1} and δ, being given by

$$T = \sum_{TB} R m_{Xe_{TB}} \tau_{TB} \tag{3.42}$$

where $m_{Xe_{TB}}$ is the Xenon mass for each time bin, τ_{TB} is the duration of each time bin and R is the energy-integrated event rate, given by [100, 102].

$$R = \int_{E_1}^{E_2} dE_R \, \epsilon(S1, S2) \frac{dR}{dE_R}. \tag{3.43}$$

where ϵ is the detector's efficiency, and E_1 and E_2 are the initial and final energies, respectively.

We used the parameters (m_{χ_1} = 58.0 GeV/c^2, μ_{χ_1}= 0.0018 μ_{nuc}, δ = 111.7 keV) in the equation 3.43, obtaining an integrated event rate, R, of 0.00415 evts/kg/d. Using the same parameters, we obtained a total number of observed events, T, of 1413 events.

We obtained the WIMP magnetic moment, $\mu_{\chi_{1limit}}$, on the no background limit of 2.44 events at a 90 % Confidence Level (C.L) [117]. We used the equation 3.41 for those calculations, employing the total number of observed events in the detector, T, obtained from the equation 3.42. From that, we obtained a limit on the WIMP magnetic moment, $\mu_{\chi_{1limit}}$, of $2.098 \times 10^{-5} \mu_{nuc}$. This limit was better by a factor of 100 comparing with $\sim$ 0.0015 μ_{nuc} obtained from XENON100 [2]. In a future analysis, we would need to obtain the limit on the WIMP magnetic moment, $\mu_{\chi_{1limit}}$, for different WIMP masses, m_{χ_1} and mass splittings, δ. These calculations would allow us to obtain the exclusion limit (at a 90 %) for MiDM interactions for a wide range of WIMP masses, m_{χ_1}, and mass splittings, δ.

We performed the calculations from the equations 3.40 and 3.41 assuming and efficiency of 100 % ($\epsilon(S1, S1) = 1$). This 100 % efficiency implies that the threshold on the S1 and S2 signals doesn't have an impact on the efficiency, because there is an amount of energy that is transferred to the nucleon. For the MiDM signal model, the threshold energy of the MiDM spectra is about 17 keV of nuclear recoil, well above the 6.6 keV limit defined by XENON100 for the 100 % efficiency [2, 54, 72].

In spite of not expecting the S1 and S2 thresholds to have a significant impact in the efficiency, there are other factors that will affect the efficiency and they must be included in these results. In these factors are included a minimum time difference between the 2 pulses of 2 μs and the finite size of the LUX detector that limits the chance to detect γ rays from the WIMP de-excitation, meaning that some of these γ rays can escape from the fiducial volume of the detector [2, 54]. These factors have not been studied in this analysis, by they will be studied in a further analysis. Nonetheless, we assumed a zero background rate for this analysis results. In the next chapter we will analyse in more detail the background sources of the detector.

Chapter 4

MiDM Analysis

Magnetic inelastic Dark Matter, MiDM, was proposed to explain the inconsistencies between the DAMA/LIBRA experiment and other dark matter experiments [2, 3]. As explained in the chapter 3, MiDM is based in an inelastic kinematics approach, assuming a non-zero magnetic moment for the Dark Matter particle [3].

In this chapter, we will focus on Magnetic Inelastic Dark Matter analysis, using data from LUX WIMP search science run [2, 72]. Magnetic Inelastic Dark Matter analysis follows a different event selection criteria compared with the traditional WIMP search analysis. For the MiDM analysis, instead of selecting only one S1 pulse followed by an S2 pulse, the event typology requires to select events with two S1s and two S2s [2]. In the figure 4.1, it is represented an example of a chronological sequence of pulses observed in a typical MiDM event [2]. It shows the first S1 pulse, $S1_{ER}$, followed by a second S1 pulse, $S1_{NR}$. These pulses are chronologically followed by two S2 pulses, $S2_{ER}$ and $S2_{NR}$. Alternatively, there is another possibility for a chronological sequence of S1, S2 pairing for the MiDM event typology, namely the

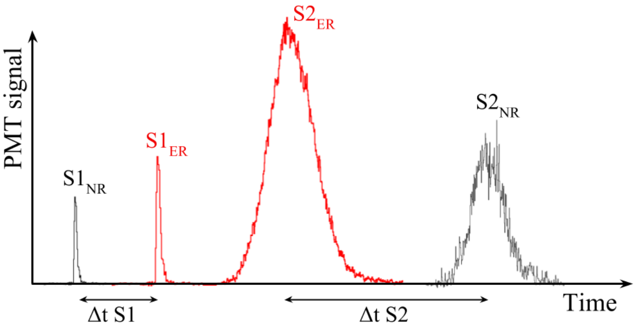

Figure 4.1: Example of the event topology for MiDM [2].

sequence $S1_{ER}$ $S2_{ER}$ $S1_{NR}$ $S2_{NR}$. The possible S1, S2 pairings that correspond to a MiDM signal will be discussed later in this chapter.

4.1 Event selection

For MiDM analysis, we used the data collected by the LUX detector between September 11, 2014 and May 2, 2016, corresponding to the Run IV dark matter search. We started by selecting the events from the Run IV LUX data that had more than one S1 and more than one S2 pulses [54, 72]. From this event selection, we obtained 10 pulses and 397990 events.

These events represent only 10 % of the events initially observed in the LUX detector. We performed this event selection, because some of these pulses are identified as S1s and S2s, but don't correspond to the energy depositions of "true" S1 or S2 pulses. These pulses occur after the first S1 or S2 pulses and have very small areas relative to the main S1 or S2 pulse, being designated as "spurious" pulses. Among other possible causes, they are mainly caused by [118, 119]:

- PMT After-pulsing: it consists of smaller pulses that appear after the "true" S1 pulse [118, 120]. For each PMT, the pulses due to afterpulsing are usually larger than the original pulse [121]. In spite the afterpulses being larger than a normal pulse from the PMT, the S1 signal is detected by many PMTs, resulting in an S1 signal generated from an afterpulsing to be smaller than the "true" S1 pulse [73]. Afterpulses that follow the "true" S1 pulse within several nanoseconds are the result of elastic electron scattering in the first dynode of the PMT [120, 122]. Beyond this interval of time, the afterpulses are caused by the ionization of residual gas atoms between the dynodes [120]. Accelerated by an electric field, the resulting ions drift towards the photocathode where they release additional photoelectrons, which cause the secondary signal [120, 122].

- Dark Counts on the PMTs: It consists of fake signals created by the spontaneous emission of photoelectrons from the PMT photocathode material, leakage current from the electronics, field emission noise, and other sources [120, 122]. The average rate of registered counts without any incident light is called dark count [120, 123]. According to the measurements made by LUX, this quantity varies between 8.2 and 18.8 counts/s and between 8.0 and 17.2 counts/s for Tritium and for the WIMP search data, respectively [124].

- Fluorescence on the PTFE: it consists on delayed light emission caused by contaminants on the PTFE walls of the detector [119, 125]. It is expected the PTFE to reflect photons impinging on the detector walls until they hit a PMT [119]. However, the PTFE walls are contaminated with volatile impurities from hydrocarbons, such as toluene and naphthalene [125]. Instead of being reflected, these photons are absorbed by the PTFE contaminants that latter re-emit them, through a type of photoluminescence called fluorescence [119].
- Electron trains following large S2 pulses: electron trains are mainly caused by S2 delayed signals, such as photo-ionization on PMTs, grids and PTFE contaminants, or delayed electron extraction [126, 127]. The delayed electron extraction consists on the electron release of electronegative impurities [127]. Those are well known to capture electrons from the primary ionization event and then drifting slowly to the liquid-gas surface.

In the following sections, it will be explained how we removed these "spurious" pulses for the S1 and S2 signals.

4.1.1 Spurious S1s

To identify the spurious S1s, we used the following quantity

$$f_{S1}^{i} = \frac{S1_i}{\sum_i S1_i} \tag{4.1}$$

where $S1_i$ is the area of the pulses identified as S1s and $\sum_i S1_i$ is the sum of all the areas of the pulses identified as S1s in an event.

The figure 4.2 shows the fraction f_{S1}^{i} as a function of the S1 pulse area, $S1_i$. The first pulses are represented by the black or magenta dots, while the second and following pulses are represented by the red and blue dots. From these pulses, all of the first pulses and following S1s with a fraction on the S1 pulse area, f_{S1}^{i}, above 0.02 are considered to be "true" S1s. The second and following pulses with a fraction on the S1 pulse area, f_{S1}^{i}, below 0.02 are considered as "spurious" S1s.

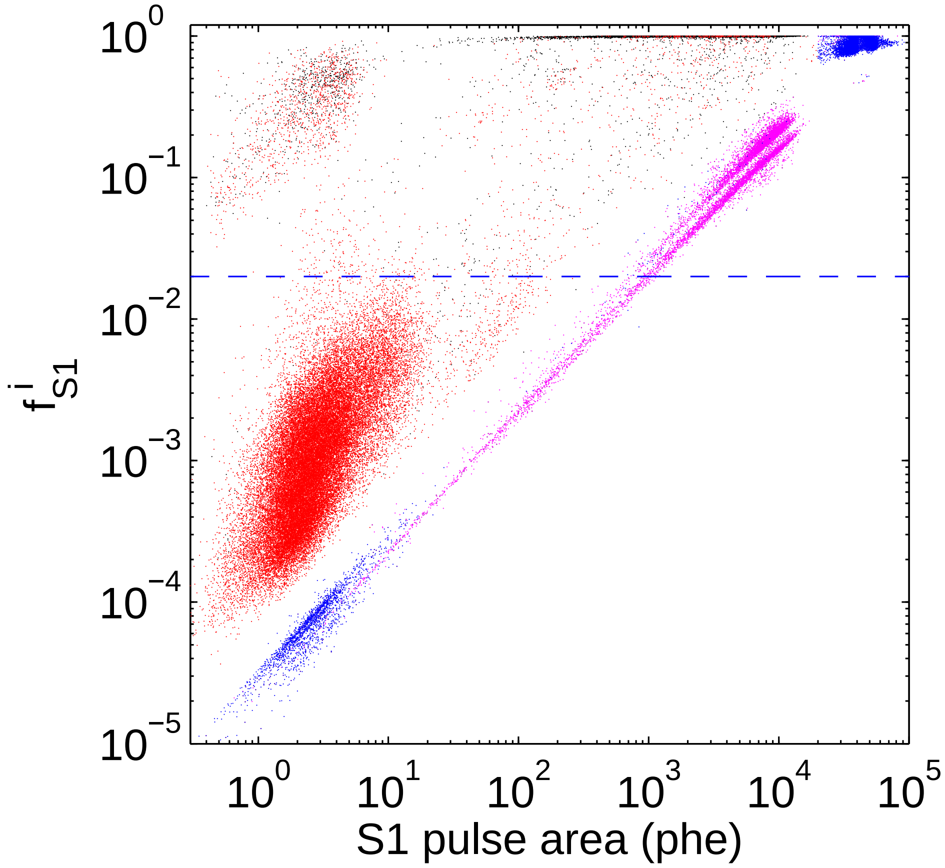

Figure 4.2: f^i_{S1} fraction as a function of the S1 area (phd). The black and magenta dots represent the first pulses, while the red and blue dots represent the second and following pulses.

In this figure, the black and red dots represent the events which sum of all the areas of the pulses identified as S1's, $\sum_i S1_i$, is lower than 20000 phd. The events with the sum of all the areas of the pulses identified as S1's, $\sum_i S1_i$, higher than 20000 phd, are represented by the magenta and blue dots. In LUX, only α depositions are able to produce such a large S1. The α particles are emitted in a range of energy between 4 and 8 MeV, which corresponds to a S1 area between 20000 and 100000 phd. We attributed this combination of signals to the β–α coincidences from the ^{214}Bi–^{214}Po decays from the ^{238}U decay chain and, in minor scale, from the ^{212}Bi–^{212}Po decays from the ^{222}Rn decay chain, shown in the figure 4.3 [128]. As a β- decay source, ^{214}Bi is one of the daughter isotopes from the ^{238}U decay chain that produces an ER background in LUX [29]. The ^{214}Bi isotope has a β decay with Q-value of 3270 keV, with a probability of 99.97 % and an half-life of 19.8 minutes

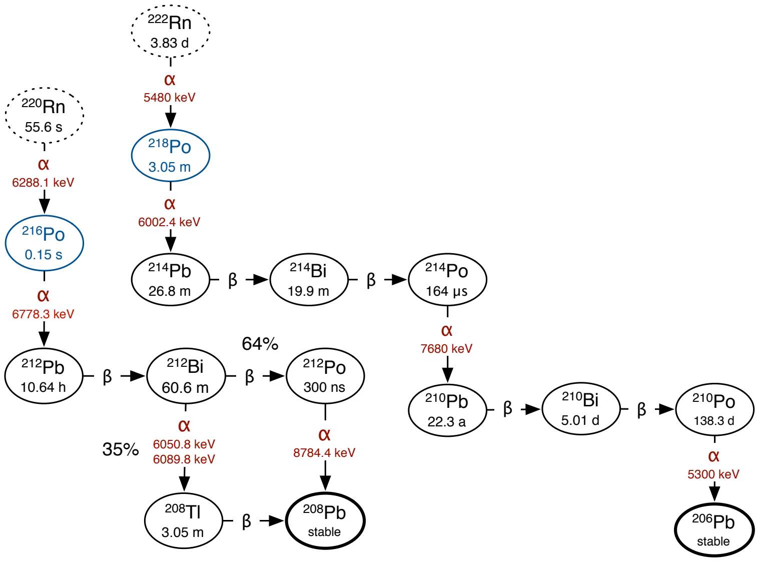

Figure 4.3: Decay chains of ^{220}Rn and ^{222}Rn from [128]

[10, 129, 130]. A fraction of 19.67 % of the ^{214}Bi isotope decays via β emission to the ground state of the ^{214}Po isotope [10, 129]. For the remaining cases, the ^{214}Bi isotope decays via β emission to the excited state of the ^{214}Po isotope, being followed by γ transition [10, 21, 129]. This γ emission is produced from many energy levels, having its most intense emission at an end-point energy of 610 keV with a probability of 46 % [129, 131, 132].

These βs and γs are represented by the magenta dots in the figure 4.2, corresponding to the first pulse of the ^{214}Bi-^{214}Po decays from the ^{222}Rn decay chain. ^{214}Po has a half-life of 164 μs before decaying into ^{210}Po via α decay, with a probability of 99.98 % and an energy of 7833.24 keV [10, 21, 132]. In the figure 4.2, the αs are represented by the blue dots with a S1 area between 10^4 and 10^5 phd.

From the two S1s that we obtained, one of them corresponds to the ^{214}Bi and the other S1 pulse corresponds to the ^{214}Po. These S1 pulses are detected both by the top and bottom PMT arrays of the detector, with more light being detected by the bottom PMT array. Some of these large S1s are detected below the cathode, in the reverse field region of the detector [7, 29]. In this region, the electrons will go downwards with no S2 signal being generated. These S1s will be detected mostly by the bottom PMT array, which will saturate due to the its high light yield.

The half-life of the ^{214}Po isotope is 164 μs, which is very short compared with the LUX 1 ms event window [10, 133]. Thus, the probability of the αs and βs being recorded within the same event is of 98.5 % for the LUX event window [10, 132].

4.1.2 Spurious S2

To identify the spurious S2's, we used the following identity

$$f^i_{S2} = \frac{S2_i}{\sum_i S2_i} \tag{4.2}$$

where $S2_i$ are the pulses identified as S2's and $\sum_i S2_i$ is the sum of all the pulses of an event identified as S2's.

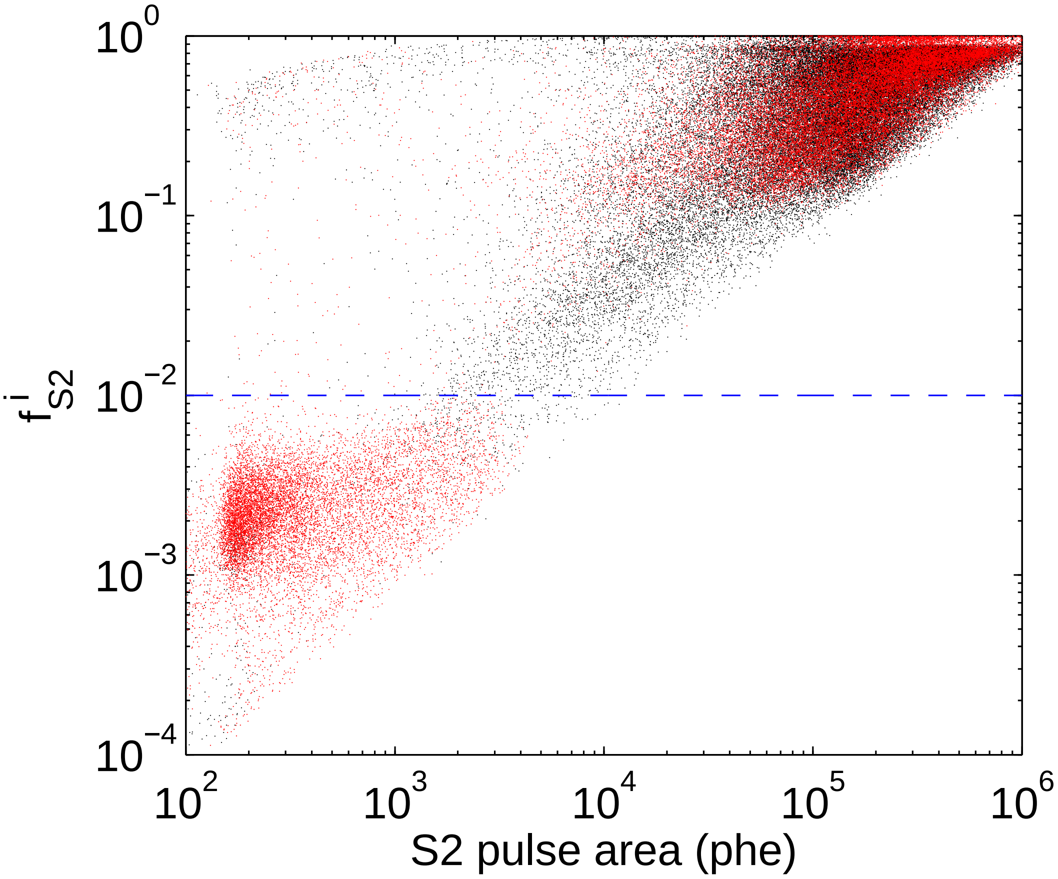

Figure 4.4: f^i_{S2} fraction as a function of the S2 area (phd). The S2 spurious pulse are represented at red, while the black dots represent the "true" S2 pulses.

The figure 4.4 shows the fraction f^i_{S2} as a function of the S2 pulse area. The black dots represent the first S2 pulses, while the second and following pulses are represented by the red dots. The red dot events located in the region where the fraction f^i_{S2} is below 0.01 are known as S2 spurious, because these S2s have a very small area and follow a large S2. To confirm that these pulses are S2 spurious, we used the Visual LUX event viewer and verified the time distribution of the spurious pulses relatively to the larger S2 pulse. As stated in the section 4.1, the spurious S2s are mainly caused by photo-ionization on PMTs, grids and PTFE contaminants, or delayed electron extraction [126, 127]. These pulses appear following large S2 pulses, as electron trains [118]. From these electron trains, the pulses with the smallest areas are identified as spurious S2s, while the other electron train pulses will be removed by a quality cut, as we will explain latter in this chapter.

4.1.3 2S1s and 2S2s Event Selection

After the identification of the pulses with a fraction f^i_{S1} below 0.02 for the S1s and a fraction f^i_{S2} below 0.01 for the S2s, we reclassified these pulses as ”spurious” pulses in the datasets obtained from the Run IV LUX data. Then, we selected the events with an event typology of two S1s and two S2s. The reclassification of the ”spurious” pulses and the two S1s and two S2s event selection lead to a reduction from 10 pulses and 397990 events to 4 pulses and 13415 events.

4.2 Electron train cut

After the identification and removal of the spurious pulses, we removed some problematic events created artificially in the tail of a very large S2, also called S2 electron trains, among other anomalies. In the tail, single electrons can be grouped together in an S2 and coupled with a random pulse identified as an S1. To remove this events, we applied a quality cut named electron train cut or bad area cut. This cut is based on the total area of the pulses of the S1, S2 pair, corresponding to the ”good area” of an event, relative to the total area of the pulses other than S1 or S2 corresponding to the ”bad area” of an event [19].

The figure 4.5 shows the bad area cut as a function of the good area for the WIMP search data. For MiDM analysis, the bad area cut, BA cut, is represented

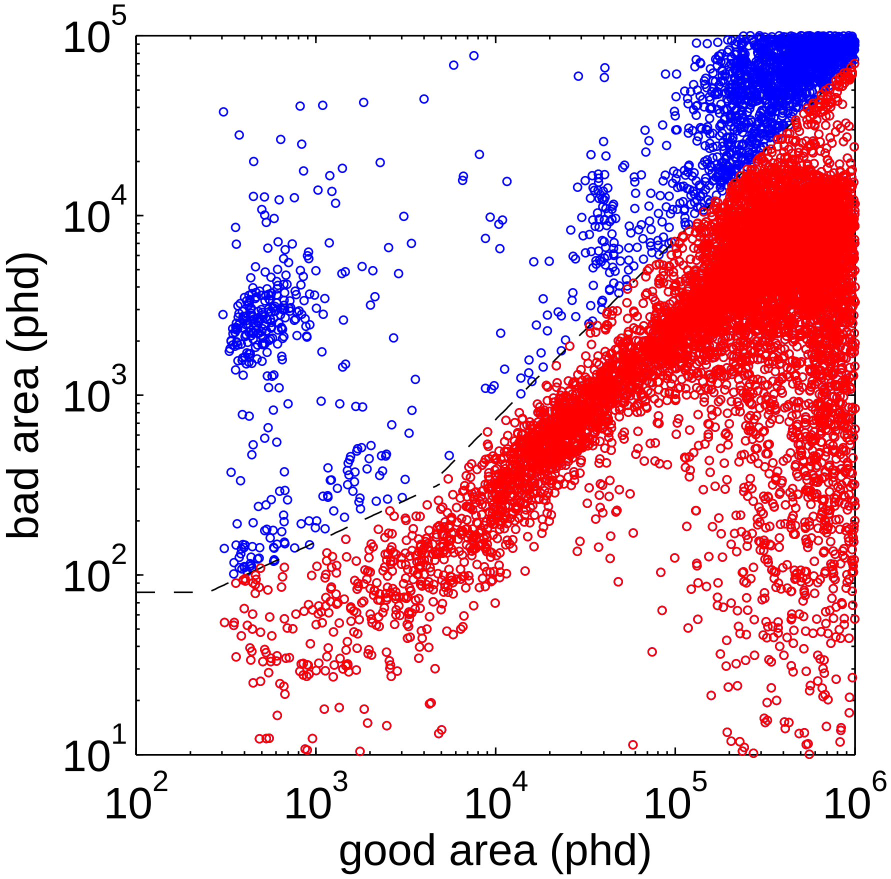

Figure 4.5: Bad area as a function of the good area. The events with too much bad area are represented by the blue dots above the black dashed line threshold and are intended to be removed.

by the black dashed line in the figure, being given by

$$\text{BA cut} = \begin{cases} 80, & \text{if } A_{\text{good}} < 253 \text{ phd} \\ 80 \times (0.0398 \times A_{\text{good}})^{0.4668}, & \text{if } 253 \text{ phd} < A_{\text{good}} < 5000 \text{ phd} \\ 100 \times (0.000732 \times A_{\text{good}}), & \text{if } A_{\text{good}} > 5000 \text{ phd} \end{cases}$$

The blue dots represent the events with too much bad area for a given good area. We identified them as "bad area", because most of the events that we observed in the LUX event viewer are present in the tail of a large S2 due to the presence of multiple single electrons. The red dots represent the events that remain in the MiDM analysis after applying the "bad area cut".

In order to finish applying this cut for the analysis, we would need to apply it to the calibration data, that would be used for the calculation of the efficiencies of this cut. This process is not trivial, because we don't have calibration data with two S1s and two S2s, but it would be possible to merge events from these calibration sources in order to have four different pulses.

4.3 Pulse pairing

For MiDM analysis, we defined the first and second pulses observed in an event, a and b, for the S1 and S2 signals as $S1_a$, $S1_b$, $S2_a$ and $S2_b$. However, for an event typology of two S1 and two S2 pulses it is not clear which S1 is paired with which S2. Specifically, both $S1_a$ and $S1_b$ pulses are not necessarily paired with $S2_a$ and $S2_b$, respectively. To solve this issue, we studied two possible S1, S2 pairings, in which the pulses could appear in the detector. From these pairings, the possible chronological sequence of the pulses observed in the timeline of an event in LUX that would correspond to a candidate event are

- $A : S1_a S2_a S1_b S2_b$
- $B : S1_a S1_b S2_a S2_b$

As for a traditional WIMP search analysis, it is rather trivial to pair the two S1 pulses with the correct S2 pulses for the chronological sequence A. This is not the case for the chronological sequence B, because the first S1 pulse, $S1_a$, is chronologically followed by the second S1 pulse, $S1_b$.

Apart from the chronological sequences, A and B, the S1 and the S2 pulses can also be paired without being related to a possible signal event, which occurs only for background events. These events can be generated by β decays followed by a γ transition, where the first S1, $S1_a$, generates the 2 S2s. The background events can also be generated by β decays without emission of γs, where the second S1, $S1_b$, generates the 2 S2s. For both cases, one of the S1s is located in the bulk of the detector. The other S1 pulse is located in other regions of the detector, such as the reverse field region. This region is located above the anode, and doesn't have any collection of S2s. We applied a cut that accepted events with the first S1 before the first S2 and the second S1 before the second S2. Together with the electron train cut, we implemented these cuts to remove events that do not follow these chronological sequences, considering only positive values for the time differences $t_d(S1_a, S2_a)$ and $t_d(S1_b, S2_b)$, respectively. The table 4.1 summarises the impact of each cut in the MiDM analysis, after removal of the events caused by S1s and S2s spurious. It shows the remaining events after applying the Bad Area Cut, the first S1 before the first S2 cut, the second S1 before the second S2 cut, all the cuts combined, excluding Bad Area Cut and all of the cuts combined.

Table 4.1: Summary of the cuts applied in the analysis, after the removal of the spurious S1s and S2s.

Cuts	Remaining events
After spurious	13415
Bad Area Cut	9851
1st S1 before 1st S2	12894
1st S1 before 1st S2	12325
All cuts excluding Bad Area Cut	11969
All cuts	8728

4.3.1 Calculation of the drift time

To characterise the chronological sequences of the 2S1s and 2S2s event selection, we considered four different possible drift times corresponding the first and second pulses, a and b, of the S1 and S2 signals, namely t_{S1_a}, t_{S1_b}, t_{S1_a} and t_{S2_b}. From these drift times, the drift time difference for the S1, S2 pairing, $t_d(S_{1j}, S_{2l})$, is given by

$$t_d(S_{1j}, S_{2l}) = t_{S_{2l}} - tS_{1j}, \tag{4.3}$$

where j, l indices stand the for first pulse, a, or for the second pulse, b.

From the equation 4.3, we obtained four different time differences for the S1, S2 pairing, $t_d(S_{1j}, S_{2l})$, but only two of them are possible for a MiDM signal, namely $t_d(S_{1a}, S_{2a})$ and $t_d(S_{1b}, S_{2b})$ or $t_d(S_{1a}, S_{2b})$ and $t_d(S_{1b}, S_{2a})$. The time difference between the second S1 and the first S2, $t_d(S1_b, S2_a)$ was used in order to distinguish the S1, S2 pairing chronological sequences described in the previous section. When the time difference $t_d(S1_b, S2_a)$ has a positive value, it corresponds to the chronological sequence A, corresponding to the chronological sequence B, when the time difference $t_d(S1_b, S2_a)$ has a negative value.

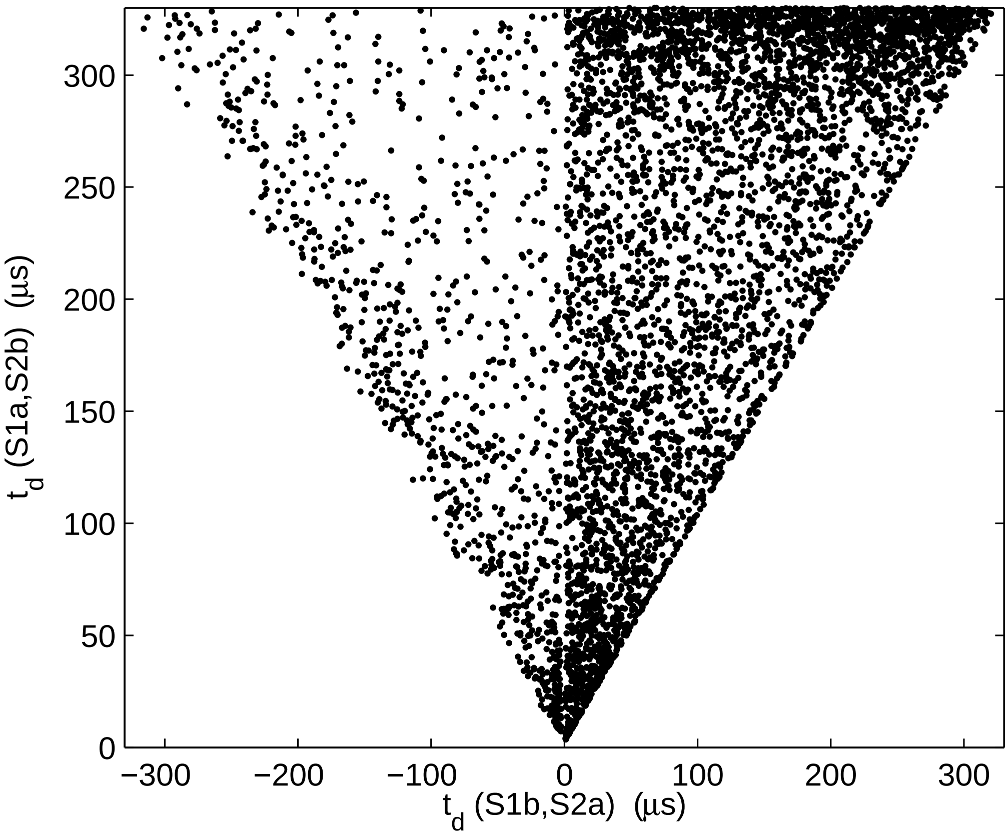

Figure 4.6: Time difference between the $S1_a$ and $S2_b$ pulses, $t_d(S1_a, S1_b)$, as a function of the time difference between the $S1_b$ and $S2_a$ pulses, $t_d(S1_b, S2_a)$.

The figure 4.6 shows the time difference between $S2_a$ and $S1_b$, $t_d(S2_a, S1_b)$, as a function of the time difference between $S2_b$ and $S1_a$, $t_d(S2_b, S1_a)$. It shows more events with a positive time difference $t_d(S1_b, S2_a)$ than events with a negative time difference $t_d(S1_b, S2_a)$. The events with a positive drift time difference $t_d(S1_b, S2_a)$ correspond to the chronological sequence, A, while the events with a negative drift time difference $t_d(S1_b, S2_a)$ correspond to the chronological sequence, B. This is caused by the condition that states that the second S2 pulse, $S2_b$, must appear after than the second S1 pulse, $S1_b$.

The figure 4.7 shows the time difference between $S1_a$ and $S2_a$, $t_d(S1_a, S2_a)$ as a function of the time difference between $S1_b$ and $S2_b$, $t_d(S1_b, S2_b)$. The time

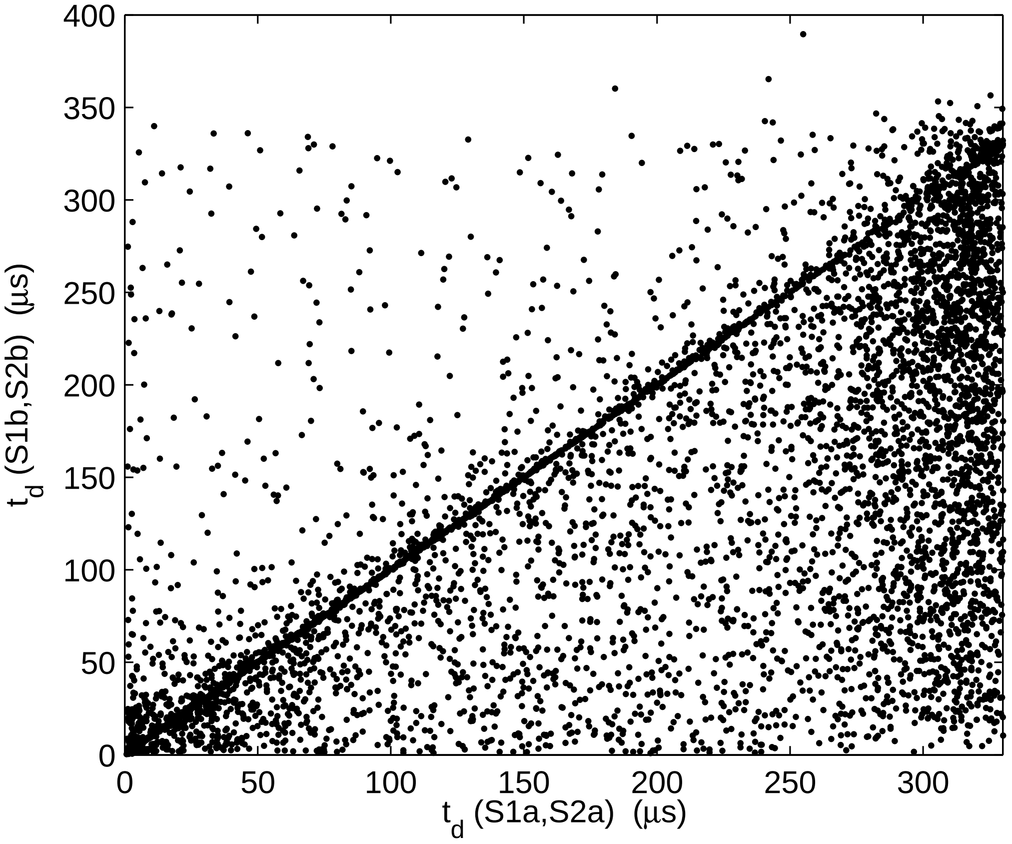

Figure 4.7: Time difference between the $S1_b$ and $S2_b$ pulses, $t_d(S1_b, S2_b)$, as a function of the time difference between the $S1_a$ and $S2_a$ pulses, $t_d(S1_a, S2_a)$.

difference $t_d(S1_a, S2_a)$ is equal to the time difference $t_d(S1_b, S2_b)$ for most of the events, because these events have two decays occurring at the same depth, z. For the events at the same depth, z, we would verify the pairing between the S1 and S2 pulses by obtaining the time difference between S1s, $t_d(S1_a, S1_b)$, in a further analysis. For a large time difference between the S1 pulses, we can affirm that the first S1 pulse, $S1_a$, is paired with the first S2 pulse, $S2_a$, being the second pulse, $S1_b$, necessarily paired with the pulse, $S2_b$. For a small time difference between the S1 pulses, the first and second S1 pulses, $S1_a$ and $S1_b$, can be crossed with the S2 pulses, with $S1_a$ being paired with $S2_b$ and the $S1_b$ being paired with $S2_a$. This means that events at the same depth, z, and a large time difference between S1 pulses correspond to the first S1, S2 chronological sequence, A. The events at the same depth, z, and a small time difference (in the order of μs) between S1 pulses, can correspond to one of the S1, S2 chronological sequences, A or B.

We observed that a significant fraction of 16 % of the events with a time difference $t_d(S1_a, S2_a)$ is consistent with the detector's bottom, while a fraction of 57 % of the events with a time difference $t_d(S1_b, S2_b)$ is consistent with the bulk of the detector. This event typology is consistent with ^{214}Bi-^{214}Po decays from the ^{222}Rn decay chain, when the ^{214}Bi isotope decays for the excited state of ^{214}Po. After this decay, ^{214}Po will take few picoseconds to decay from the excited state to its ground state with the emission of γ particles. This γ transition is then followed by an α decay from the ^{214}Po isotope to the ^{210}Pb isotope. Initially, ^{214}Bi is located in the detector's grids. For the α particles detected on the fiducial volume, they decay in the direction of the reverse field region, while the β and γ particles decay into the fiducial volume.

The β and γ particle decays correspond to the first S1 pulse, $S1_a$, because their energy depositions are consistent with the size of $S1_a$. These decays occur together, because the γ decay from the excited to the ground state of the ^{214}Po isotope occurs within a few picoseconds. The second S1 pulse, $S1_b$, corresponds to the α, because the very large size of this S1 pulse is consistent with the energy depositions of the α particles. Although, the first S2 pulse, $S2_a$, corresponds to the β particle energy depositions that occur near the grids of the detector, while the second S2 pulse, $S2_b$, correspond to the γ particle energy depositions that occur above the grids. This happens because of the two S2s being very near from each other. This means that the two S2s have a very small time difference, which is consistent with the γ particle energy depositions. These two S2s are generated by the first S1 pulse, $S1_a$, because the other S1, $S1_b$, has a very large size, being consistent with energy depositions of the α particles. This S1 is originated below the cathode, in the reverse field region of the detector [7, 29]. In this region, the electrons will go downwards with no S2 signal being generated.

4.3.2 The depth of the event from S1 top bottom asymmetry and S2 pulse shape

It is possible to estimate the depth of a pulse with high uncertainty, using the top-bottom asymmetry of the S1 pulse, TBA, and the S2 pulse width, σ_{S2}. We will use this information to exclude some of the combinations of pulses described in the previous section.

The top-bottom asymmetry, TBA, is used to pair the chronological sequence A, relating $S1_a$ and $S1_b$ with their respective S2s, $S2_a$ and $S2_b$. The top-bottom asymmetry, TBA, is given by

$$TBA = \frac{t-b}{t+b} \tag{4.4}$$

where t and b are the light read out of the top and bottom PMT arrays, respectively. In order to use the S1 top-bottom asymmetry, TBA, to extract the drift time, $t_d(TBA)$, from the WIMP search data, we need to understand how the S1 top bottom-asymmetry, TBA, varies with the drift time, $t_d(TBA)$. To study this dependence, we used data from WIMP search events with $^{83\mathrm{m}}$Kr and ^{14}C as calibration sources.

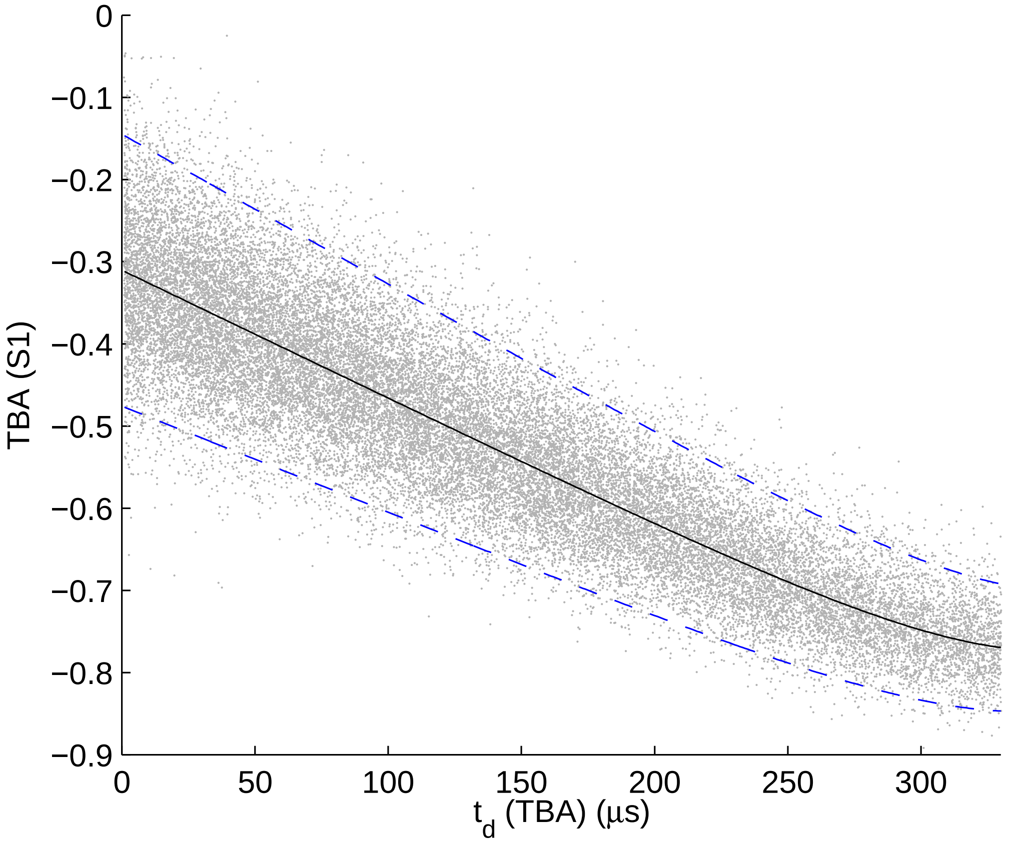

Figure 4.8: S1 Top bottom ratio as a function of the drift time of WIMP search data from $^{83\mathrm{m}}$Kr calibrations.

The figure 4.8 shows the S1 top bottom asymmetry, TBA, as a function of the drift time, $t_d(TBA)$, for the $^{83\mathrm{m}}$Kr calibration data. We used $^{83\mathrm{m}}$Kr to obtain the drift time, $t_d(TBA)$, from the S1 top-bottom asymmetry, TBA, because we need to known the correspondent S1 top-bottom asymmetry, TBA , for a given drift time, $t_d(TBA)$. The black line represents the mean value of the top bottom asymmetry as function of the drift time. This mean value was obtained by applying a fit function, $y_{^{83\mathrm{m}}\mathrm{Kr}}$, to the top-bottom asymmetry associated with WIMP search data calibrated with $^{83\mathrm{m}}$Kr. This fitted function, $y_{^{83\mathrm{m}}\mathrm{Kr}}$, is given by

$$y_{^{83\mathrm{m}}\mathrm{Kr}} = b + mDT + A\exp^{-\frac{330-DT}{\tau}} \tag{4.5}$$

where m= -0.1, b= 55 μs, A= 30 μs and τ= 10 μs are the coefficient parameters for the fitted function $y_{^{83\mathrm{m}}\mathrm{Kr}}$, and DT is the drift time for the WIMP search data calibrated with $^{83\mathrm{m}}$Kr. The blue dashed lines correspond to the 1 σ band, representing the fluctuations on the S1 top-bottom asymmetry. These fluctuations depend on the size of the S1 signal and we obtained them using the data from WIMP search ^{14}C calibrations.

Figure 4.9 shows the uncertainty associated to S1 top bottom asymmetry in WIMP search events from the ^{14}C calibrations, $\sigma_{TBA(^{14}\mathrm{C})}$, as a function of the S1 area. These events correspond to ^{14}C calibrations that occurred in August 2016, after the end of Run IV LUX operations [19]. The red line in the figure represents this uncertainty normalized to the average S1 pulse, obtained from $^{83\mathrm{m}}$Kr calibrations. This normalization factor was used to obtain the corrected response of the detector to the center of the active region [73]. For this uncertainty, we also applied a fit function, $y_{^{14}\mathrm{C}}$, represented by the blue line in the figure 4.9 and given by

$$y_{^{14}\mathrm{C}} = b + A\exp^{-\frac{PA}{\tau}} + B\exp^{-\frac{PA}{\tau_2}} \tag{4.6}$$

where b= 1.0 μs, A=2 μs, B= 0.2 μs, τ=5 μs and τ_2=50 μs are the coefficient parameters for the fitted function $y_{^{14}\mathrm{C}}$, and PA is the uncertainty on the drift time for the WIMP search data calibrated with ^{14}C.

The depth, z, can be obtained using the S2 pulse width from the $^{83\mathrm{m}}$Kr calibration data. We obtained some information about the drift time from the S2 pulse width, σ_{S2}, because of the diffusion of the electron cloud caused by the repulsive force between the electrons. For uniform electric field conditions, the S2 pulse width, σ_{S2}, is given by

$$\sigma_{S2}^2 = k_0 + k_1 DT \tag{4.7}$$

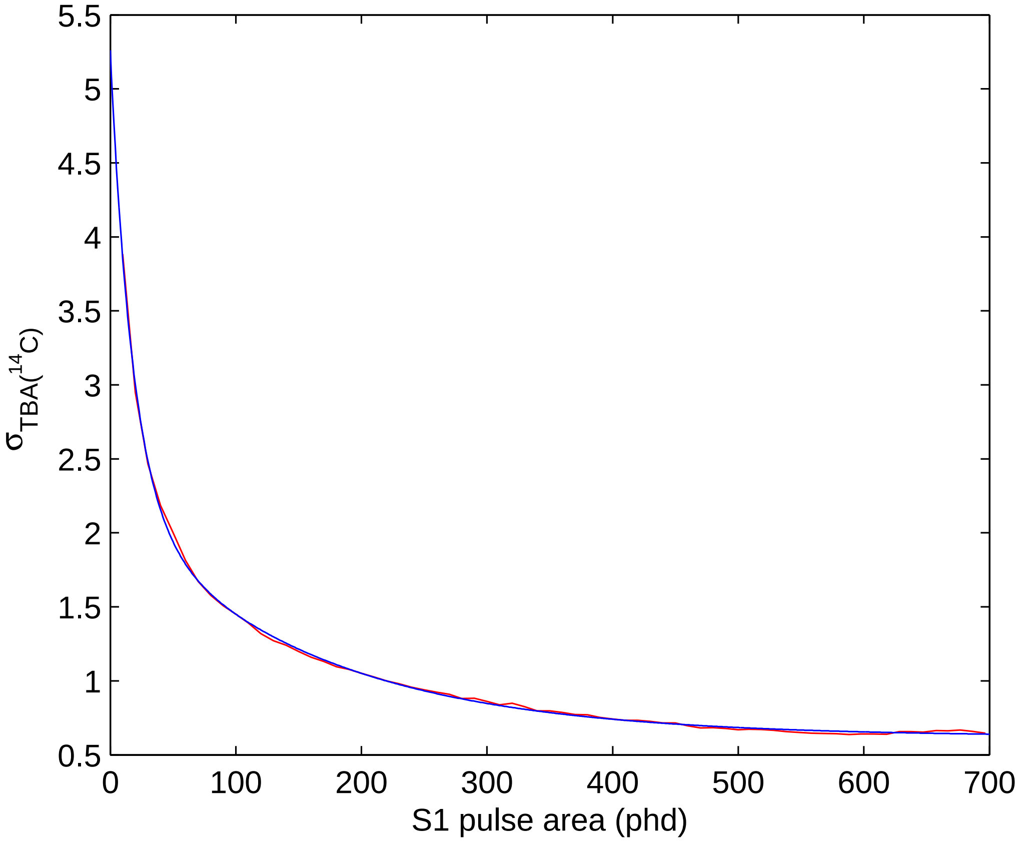

Figure 4.9: Uncertainty associated with the top-bottom asymmetry, $\sigma_{TBA(^{14}\mathrm{C})}$, as a function of S1 pulse area for the WIMP search data calibrated with ^{14}C as a source.

where k_0 and k_1 are independent and dependent parameters on the drift time for the WIMP search data calibrated with $^{83\mathrm{m}}$Kr. To evaluate the relation between the S2 pulse width, σ_{S2}, and the drift time, we used the WIMP search events from $^{83\mathrm{m}}$Kr calibrations data.

In the figure 4.10, it is shown the S2 pulse width, σ_{S2}, as a function of the drift time of WIMP search data from $^{83\mathrm{m}}$Kr. From this figure, the S2 pulse width, σ_{S2}, is approximately linear for a drift time below 150 μs, while the S2 pulse width, σ_{S2}, becomes sensitively higher for a drift time higher than 150 μs.

To have a better evaluation of the S2 pulse width, σ_{S2}, on the drift time, we will need to apply an exponential fit function to the the S2 pulse width, σ_{S2}. We didn't apply this function to the S2 pulse width, but this should be done in a further analysis.

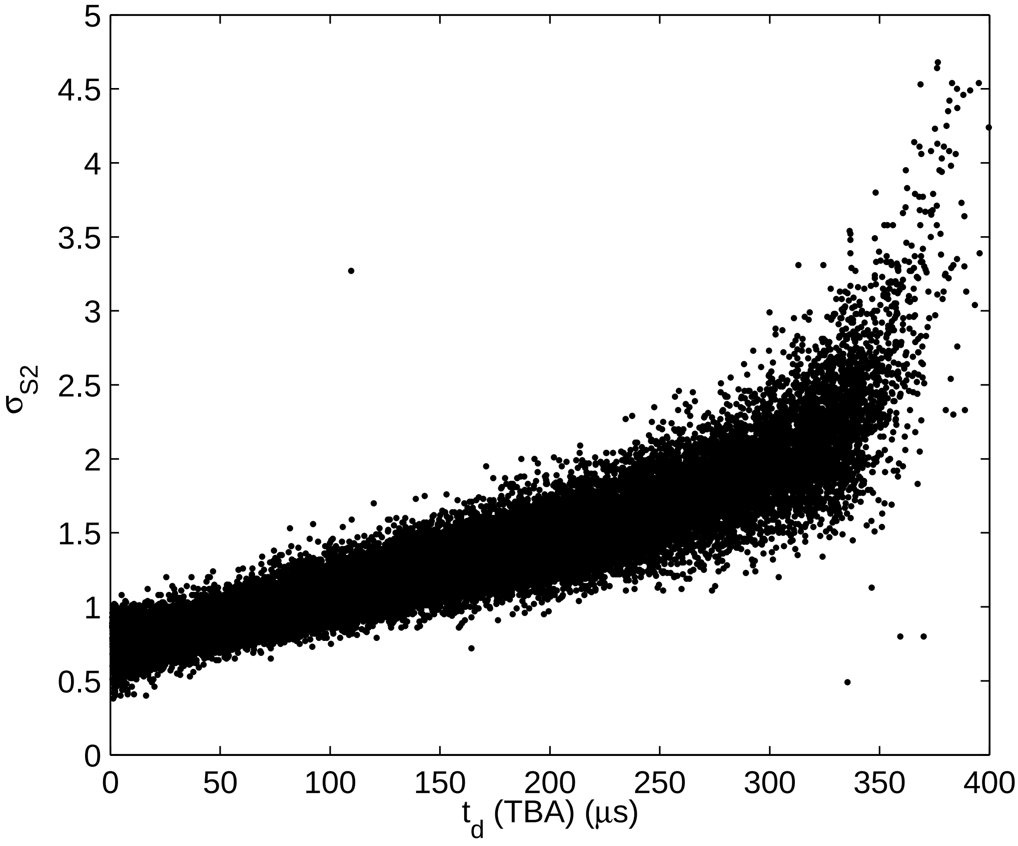

Figure 4.10: S2 pulse width, σ_{S2}, as a function of the drift time of WIMP search data from ^{83m}Kr.

4.3.3 Pairing probability

After the study of the dependence of the S1 top-bottom asymmetry and the S2 pulse width on the drift time, we used the S1 top- bottom asymmetry and the S2 pulse width to test the pairing between the S1 and S2 pulses. To study the pairing between the S1 and S2 pulses, we used the number of standard deviations from the average value, namely pulls. The amount of pulls, $g(S1_i, S2_j)$, corresponds to a quantity centered at zero, $t_d(S1_i, S2_j) - t_{d(TBA)}(S1_i)$, normalized to the width of the S1 top-bottom asymmetry, $\sigma_{TBA}(S1)$, for a given drift time. For the pairing between of the first S1 and S2 pulses, $S1_a$ and $S2_a$, the amount of pulls, $g(S1_a, S2_a)$, is given by

$$g(S1_a, S2_a) = \frac{t_d(S1_a, S2_a) - t_{d(TBA)}(S1_a)}{\sigma_{TBA}(S1)}, \tag{4.8}$$

where $t_d(S1_a, S2_a)$ is the drift time between $S1_a$ and $S2_a$, $t_{dTBA}(S1_a)$ is the drift time associated to the top-bottom asymmetry of the $S1_a$ pulse and $\sigma_{TBA}(S1_a)$ is the width of the top-bottom asymmetry of the $S1_a$ pulse.

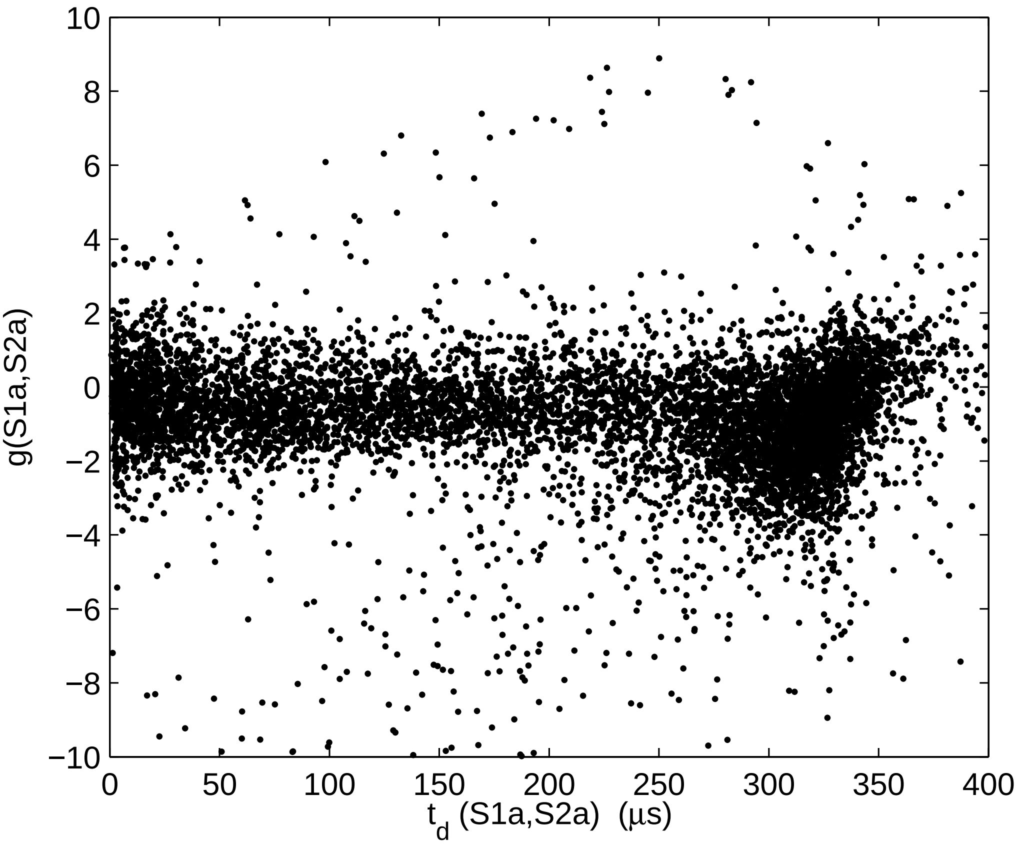

Figure 4.11: First pulse pulls, $g(S1_a, S2_a)$, as a function of the time difference between the $S1_a$ and $S2_a$ pulses, $t_d(S1_a, S2_a)$.

The amount of pulls for the first and second pulses, $g(S1_a, S2_a)$ and $g(S1_b, S2_b)$, as a function of the drift time, is represented in the figures 4.11 and 4.12. To remove the α particle events, we selected the events with an S1 pulse area lower than 10000 photo-electrons detected (phd) for both first and second pulses. These events are originated from ^{214}Bi-^{214}Po decays, and are represented by the magenta dots in the figure 4.2 from the section 4.1.1, while the events originated by βs and γs are represented by the blue dots in the same figure. In the table 4.2, there are represented the number of events before and after the removal of the α particles for the first and second pulses. For the first pulse, a fraction of 97 % of the initial events represent the remaining events after the removal of the αs. This fraction is

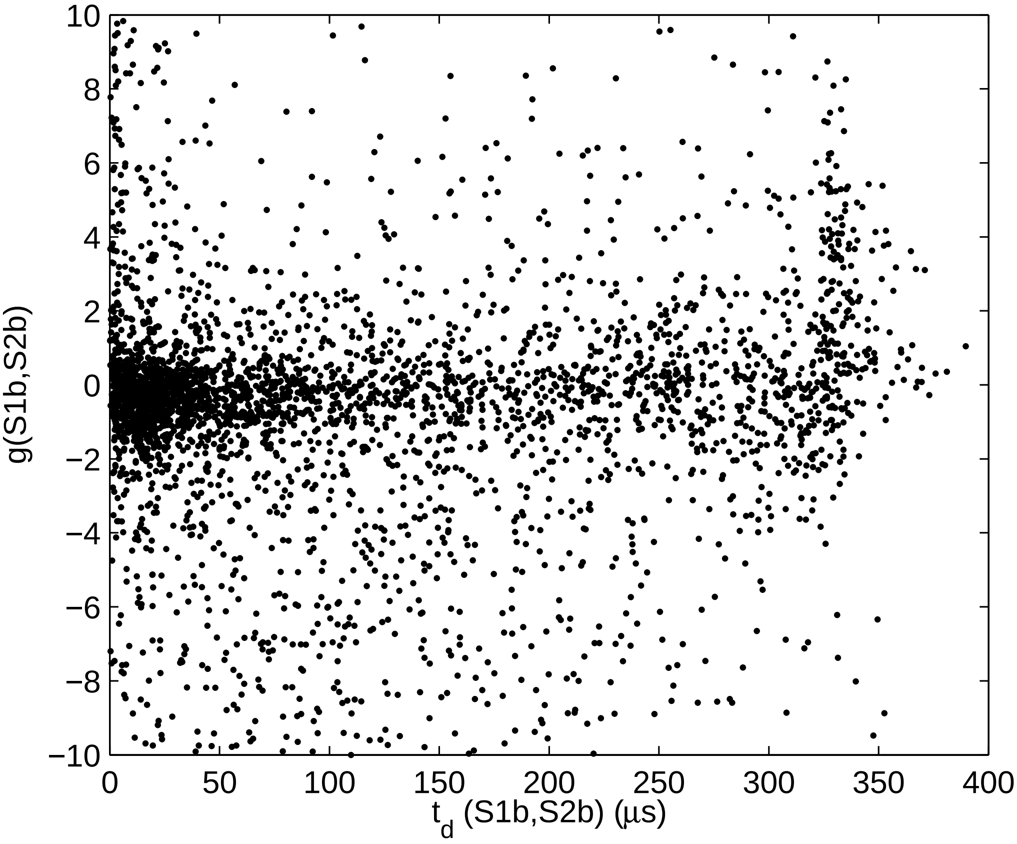

Figure 4.12: Second pulse pulls, $g(S1_b, S2_b)$, as a function of the time difference between the $S1_b$ and $S2_b$ pulses, $t_d(S1_b, S2_b)$.

Table 4.2: Number of events before and after the removal of the α particles for the first and second pulses.

	Events with α's	Events without α's
First pulse	8728	8434
Second pulse	8728	4068

much lower for the second pulse, representing 47 % of the initial events.

In the figure 4.11, the probability of the pulls located in the interval between -2 and 2 σ is 95 % for the ($S1_a$, $S2_a$) pairing. For a time difference, $t_d(S1_b, S2_b)$, lower than 300 μs, a fraction of 82 % of the ($S1_a$, $S2_a$) pair is located in the interval between -2 and 2 σ. For a time difference, $t_d(S1_b, S2_b)$, higher than 300 μs, a fraction of 81 % of the ($S1_a$, $S2_a$) pair is located in the interval between -2 and 2 σ.

In the figure 4.12, the probability of the pulls located in the interval between -2 and 2 σ is 95 % for the ($S1_b$, $S2_b$) pairing. For a time difference, $t_d(S1_b, S2_b)$, below 300 μs, a fraction of 61 % of the pulses ($S1_b$,$S2_b$) is located in the interval between -2 and 2 σ. A significant amount of these events is located in the region where $t_d(S1_b, S2_b)$ is lower than 50 μs, representing a fraction of 68 % of the pulses ($S1_b$,$S2_b$) located in this region.

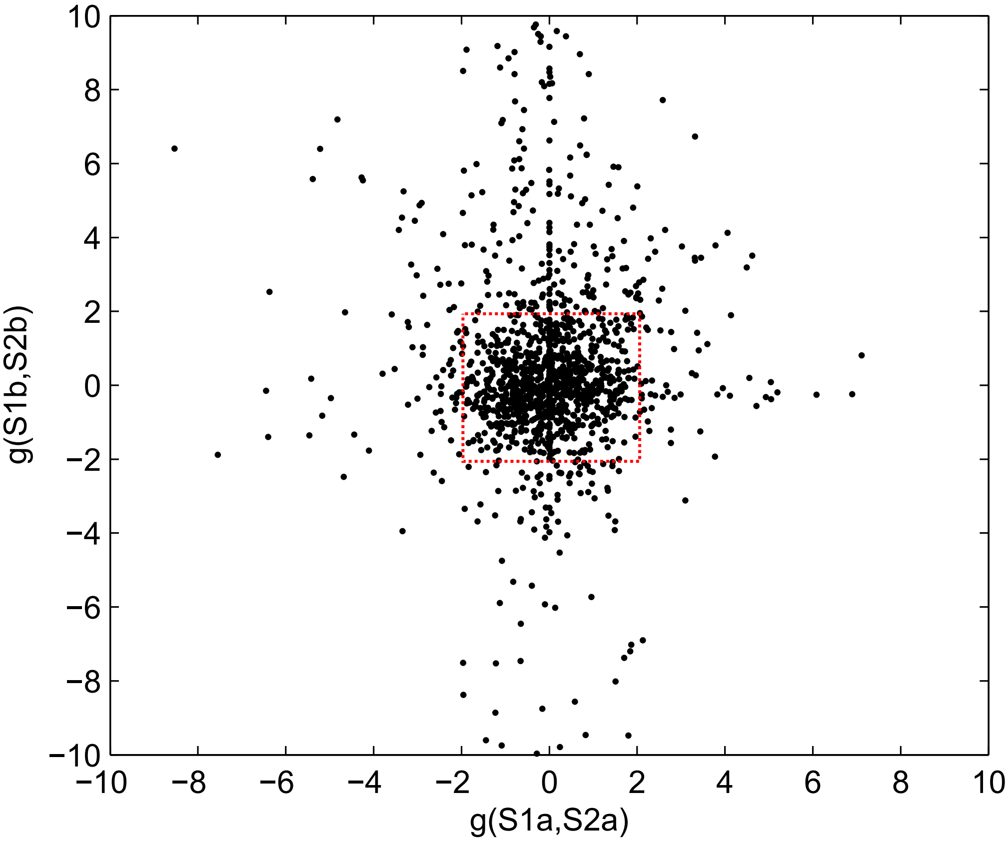

Figure 4.13: First pulse pulls as a function of the second pulse pulls

The figure 4.13 shows the pulls from the ($S1_b$, $S2_b$) pairing, $g(S1_b, S2_b)$, as a function of the pulls from the ($S1_a$, $S2_a$) pairing, $g(S1_a, S2_a)$. We draw a red dotted square in the figure, to study the compatibility between the S1 top-bottom asymmetry, TBA and the ($S1_a$,$S2_a$) and ($S1_b$,$S2_b$) pairings. This red dotted square is limited by the region between -2 σ and 2 σ for the pulls of both ($S1_a$,$S2_a$) and ($S1_b$,$S2_b$) pairings. For this region, we expected the S1s, $S1_a$ and $S1_b$, to have a probability of 95 % to be paired with S2s, $S2_a$ and $S2_b$, according to the gaussian distribution. However, we obtained a fraction of 12 % of the events for the region outside the red dotted square, which is higher than the expected fraction of 5 % for a gaussian distribution, suggesting that a fraction of the $S1_a$ pulses is not paired with the corresponding $S2_a$ pulse.

For the first chronological sequence, A, the total amount of pulls, g_D, is given by

$$g_D = \sqrt{g^2(S1_a, S2_a) + g^2(S1_b, S2_b)}, \tag{4.9}$$

where $g^2(S1_a, S2_a)$ are the squared pulls between the $S1_a$ and $S2_a$ pulses and $g^2(S1_b, S2_b)$ are the squared pulls between the $S1_b$ and $S2_b$ pulses.

We can also perform this analysis for the chronological sequence B, characterizing the total amount of pulls, g_X, as

$$g_X = \sqrt{g^2(S1_a, S2_b) + g^2(S1_b, S2_a)}, \tag{4.10}$$

where $g^2(S1_a, S2_b)$ are the squared pulls between the $S1_a$ and $S2_b$ pulses and $g^2(S1_b, S2_a)$ are the squared pulls between the $S1_b$ and $S2_a$ pulses.

The figure 4.14 shows the total amount of pulls for the first chronological sequence, g_D, as a function of the total amount pulls for the second chronological sequence, g_X. In this figure, the black dots represent the events with a positive drift time difference $t_d(S_{1b}, S_{2a})$. The red rots represent events with a positive drift time difference $t_d(S_{1b}, S_{2a})$ and a pulse area lower than 10000 photo-electrons detected (phd) for both first and second S1 pulses, $S1_a$ and $S1_b$. The table 4.3 shows the number of events for event typologies associated with a MiDM signal, and the number of events for event typologies different than a signal produced by MiDM. For

Table 4.3: Number of events that describe the S1, S2 pairing for the chronological sequences A and B.

	All events	S1 area < 10000 phd
$g_D > 2$ & $g_X > 2$	4200	1756
$g_D < 2$ & $g_X > 2$	796	221
$g_D > 2$ & $g_X < 2$	405	114
$g_D < 2$ & $g_X < 2$	1825	868

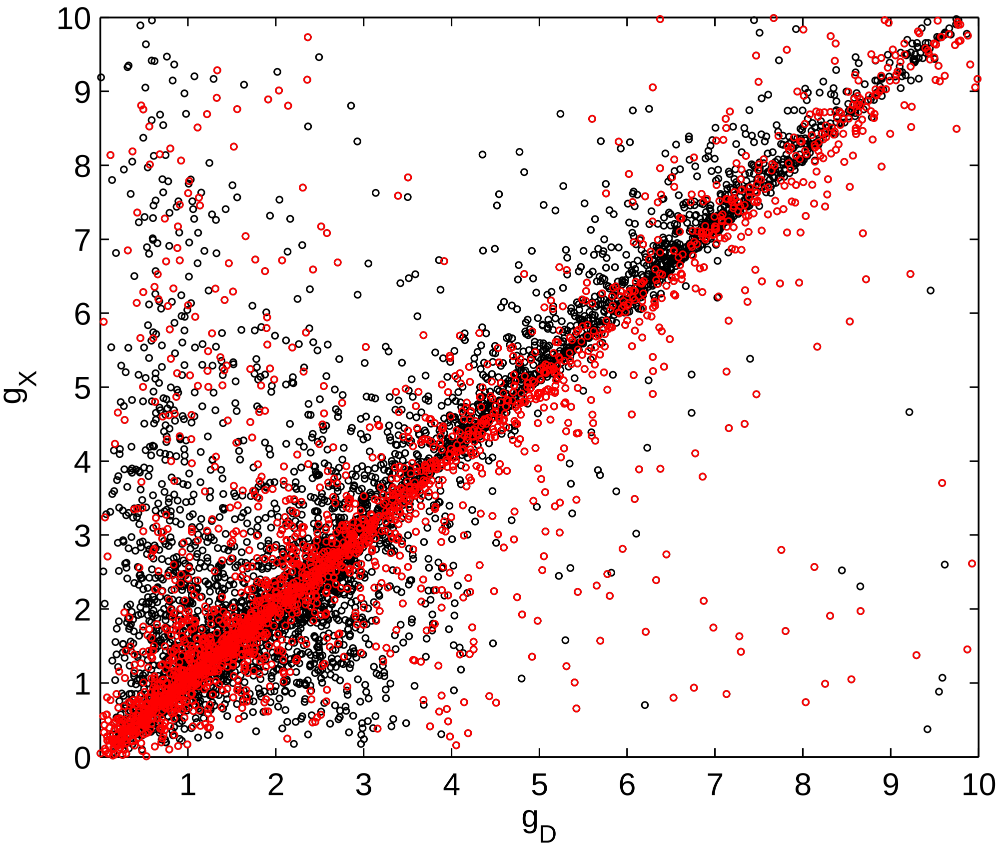

Figure 4.14: Total amount of pulls, g_D, as a function of total crossed pulls, g_X.

most of the events, g_D and g_X is lower than two, meaning that each event has a very high probability of belonging to one of the chronological sequences, A or B, and it is not possible to distinguish between the chronological sequences, A and B, using this method. An important fraction of the events have a g_D lower than two and g_X higher than two, implying that those events have a very high probability of belonging to the chronological sequence, A, excluding the second chronological sequence, B. Another fraction of the events have a g_D higher than two and g_X lower than two, meaning that those events have a very high probability of belonging to the chronological sequence, B, excluding the first chronological sequence, A. Some of the events have a g_D higher than two and a g_X higher than two, being incompatible with both first and second chronological sequences. These events are most probably coincidences from ^{214}Bi-^{214}Po decays, having a different event typology than a signal produced by MiDM.

We could easily add the S2 pulse width contribution to this analysis, obtaining the amount of pulls for the S2 pulse width and add this contribution as a quadratic term to the equations 4.9 and 4.10.

In order to finish this analysis, we would need to apply a cut on the energies of the first and second pulses, E_a and E_b, considering a nuclear recoil, NR, for the energy of the first pulse. Although, this cut must be applied after the conclusion of the remaining analysis. In the following sections, we will study the possible background sources that can produce a signal in the region of interest.

4.4 Backgrounds in the MiDM Analysis

The classic WIMP search and MiDM analysis follow different event typologies [2, 54, 72]. WIMP search focuses on NR single-scatter events with one S1 pulse and one S2 pulse [54, 72], while MiDM focuses on a NR single scatter followed by an ER single scatter, which should produce two S1 pulses and two S2 pulses [2]. Our main goal was to show that the number of backgrounds from these sources was low enough to assume a background free experiment, rather than estimating a specific value for the contributions of the background sources associated with MiDM. To perform that, we considered a maximum value of 0.1 events for the background sources and we also applied some of the cuts used in the main analysis, as we will explain further below.

There are not many background sources that produce such a characteristic signal. We identified the following possible background sources that can produce a signal in the detector similar to the MiDM interactions:

- β-γ coincidences from ^{85}Kr decays;
- Pile-up of two single scatter non correlated events from background sources;
- Pile-up between a double scatter with one S1 and two S2, produced mainly from γ rays, and a S1 pulse without any correlated S2;
- $\beta^- - \alpha$ coincidences from ^{214}Bi- ^{214}Po and ^{212}Bi – ^{212}Po decays.

The β^--α coincidences from ^{214}Bi- ^{214}Po and ^{212}Bi- ^{212}Po decays are Radon related backgrounds [2, 128]. These background sources occur in the ^{232}Th and ^{238}U decay chains, as we briefly described in the section 4.1.1 [128]. Although, an analysis on this background sources will be considered in the future.

4.4.1 β-γ coincidences from ^{85}Kr decays

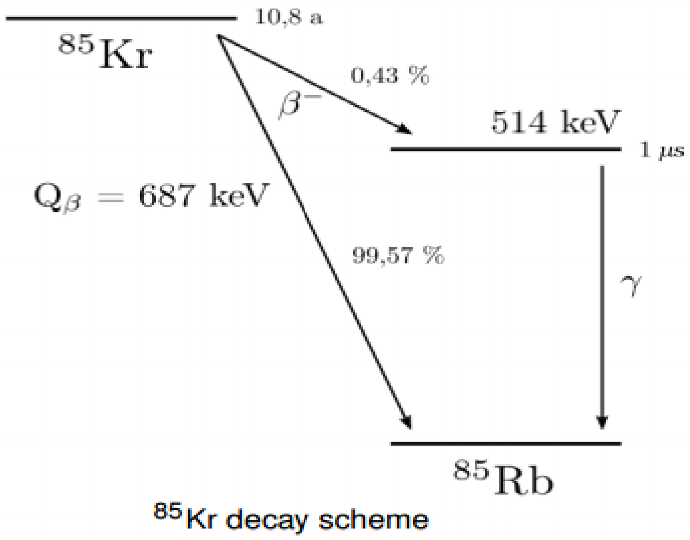

Figure 4.15: ^{85}Kr decay scheme from [29]

The radioactive decay scheme for the ^{85}Kr isotope is represented in the figure 4.15 [29]. This isotope decays via β^- decay to the ground state of ^{85}Rb with a probability of 99.57 % and an endpoint energy of 687 keV [134]. ^{85}Kr also decays via another β decay to ^{85m}Rb with a probability of 0.434 % and 173 keV of endpoint energy. This last β decay is followed by a γ transition that releases 514 keV of energy between the ^{85m}Rb and ^{85}Rb isotopes.

The decay to the ground state of ^{85}Rb is the most problematic for the WIMP search analysis, because it can create low energy single scatter events. In contrast, the most problematic decay for MiDM Analysis is the decay for the excited state ^{85m}Rb followed by a γ transition, because it can create double scatters.

^{85}Kr in RunIV

In order to include the ^{85}Kr decay in our region of interest, the energy deposited by the γs and βs in detector must be low, and the γs can only interact once in the detector, being unable to deposit all of its energy in the detector. The number of background events from β^--γ delayed coincidences, N_{bckg} in ^{85}Kr is given by

$$\begin{aligned} N_{bckg} = N_{^{85}\mathrm{Kr}} P_\beta(E_\beta < 50keV) P_\gamma(SS) P_\gamma(E_\gamma < 200keV) \times \\ \times P_{\Delta t}(\Delta t > 2\mu s) \end{aligned} \tag{4.11}$$

where $N_{^{85}\mathrm{Kr}}$ is the number of ^{85}Kr decays to the excited state $^{85\mathrm{m}}$Rb, $P_\beta(E_\beta < 50$ keV) corresponds to the fraction of β events with an energy less than 50 keV, $P_\gamma(SS)$ is the fraction of γ events that scatter only once in the detector, $P_\gamma(E_\gamma < 200$ keV) is the fraction of single-scatter (SS) γ events with an energy less than 200 keV and $P_{\Delta t}(\Delta t > 2\mu s)$ is the fraction of events with a drift time higher than 2 μs. We considered this value for LUX, because it consists on the minimum time difference between the 2 S1 pulses that is required to separate those 2S1s efficiently [2, 54, 72].

We should have a nuclear recoil, NR, for the reconstructed energy of the first pulse, E_a, as expected for MiDM. Instead, we used an electronic recoil, ER, for the reconstructed energy of the first pulse, E_a, which has a different energy reconstruction than the nuclear recoil. The nuclear and electronic recoil energies, E_{nr} and E_{ee}, don't have an exact correspondence, but they are described approximately as [45, 67]

$$E_{nr} = Q(E_{nr}) \times E_{ee} \tag{4.12}$$

where $Q(E_{nr}) = 0.2$ is the quenching factor that relates the two recoil energies, E_{nr} and E_{ee}, that correspond to the first and second pulse energies, E_a and E_b, respectively [135]. Considering the equation 4.12 and a maximum energy of 300 keV$_{nr}$ (where the subscript nr means that the energy was reconstructed assuming a nuclear recoil, NR), we concluded that would be best to apply a cut in the S1 for an energy of 100 keV$_{ee}$ (where the subscript ee means that the energy was reconstructed assuming an electronic recoil, ER) rather than 50 keV$_{ee}$, as we did in this analysis. This should be corrected in further analysis.

We created a python script based on [11] to obtain the fractions of single-scatter, γ and β events, and then N_{bckg}.

From Rachel Mannino's thesis [11], the number of events obtained from delayed coincidence between β- γ from ^{85}Kr decays is $N_{^{85}\mathrm{Kr}}$= 38.0. These events represent the total number of ^{85}Kr events during all Run IV operation. We used events with more than two multiple scatters to account for the γs than interact multiple times in the detector.

To get the fraction of events with an energy less than 50 keV, $P_\beta(E_\beta < 50\text{ keV})$, we used the Fermi theory for β decay, developed by Enrico Fermi in 1934 [136, 137]. Following this approach, the shape of the energy distribution is approximately given by

$$N(p) = C\sqrt{T_e^2 + 2T_e m_e c^2}(Q - T_e)^2(T_e + m_e c^2)F(Z', p) \tag{4.13}$$

where T_e is the kinetic energy of the electron, $m_e c^2$ is the rest energy of the electron and $F(Z', p)$ is the Fermi function. The Fermi function is approximately given by [138]

$$F(E, Z') = \frac{2\pi\eta}{1 - exp(-2\pi\eta)} \tag{4.14}$$

with the Sommerfeld parameter given by $\eta = \alpha Z'/\beta$.

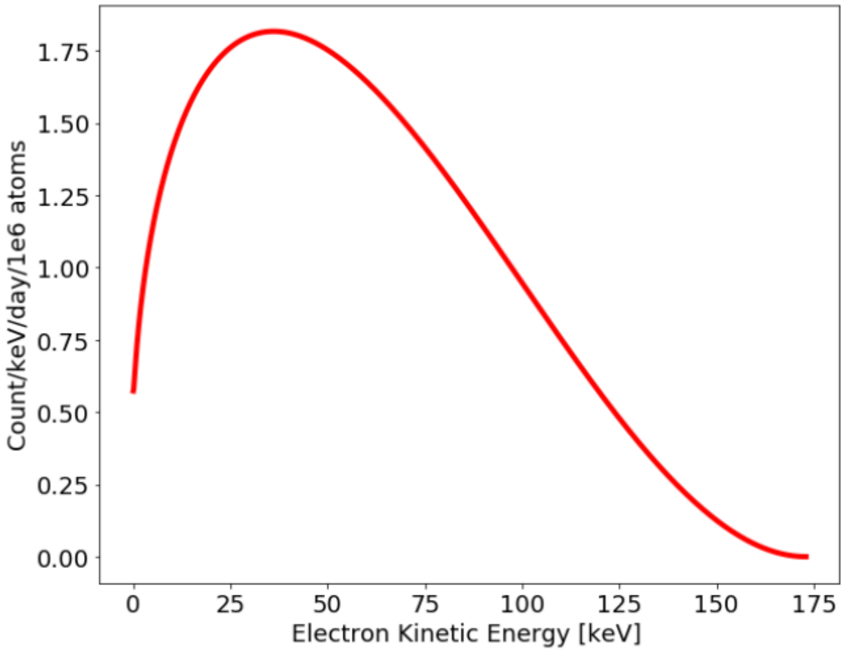

Figure 4.16: ^{85}Kr β spectrum with 173 keV of endpoint energy [11].

The figure 4.16 shows the β spectrum for ^{85}Kr with an endpoint energy of 173 keV [11]. The 50 keV limit on the β corresponds approximately to an S1 of 500 keV, which is a bit larger than our upper limit of 300 phd. Therefore this approach is conservative. From this spectra, we obtained a fraction of β events with an energy less than 50 keV, $P_\beta(E_\beta < 50keV)$, of 0.76.

The fraction of single scatter γ events, $P_\gamma(SS)$, is given by

$$P_\gamma(SS) = \frac{N_\gamma(SS)}{N_\gamma} \tag{4.15}$$

where $N_\gamma(SS)$ is the number of γ single scatter events and N_γ is the total number of γ events. From the equation 4.15, we obtained a fraction of single scatter γ events, $P_\gamma(SS)$, of 0.61.

Similarly, we obtained a fraction of single-scatter (SS) γ events with an energy less than 200 keV, $P_\gamma(E_\gamma < 200$ keV), of 0.16.

The fraction of events with drift time higher than 2 μs, $P_{\Delta t}(\Delta t > 2\mu s)$, is given by [11]

$$P_{\Delta t}(\Delta t > 2\mu s) = \frac{\int_2^\infty \exp^{\frac{-2}{\ln(2)}} \mathrm{d}x}{\int_0^\infty \exp^{\frac{-2}{\ln(2)}} \mathrm{d}x}$$

We obtained a fraction of these events, $P_{\Delta t}(\Delta t > 2\mu s)$, of 0.25.

From all of these measurements, we arrived to the number of background events, N_{bckg}, of β- γ coincidences from ^{85}Kr decays. We obtained a number of background events, N_{bckg}, of 0.087 events, a very low value below the 0.1 event limit for a no background experiment [2, 139]. Based on this value, we could also include the ER/NR discrimination in the MiDM background source analysis.

4.4.2 Pile-up of two single scatter events

The second background source considered corresponds to the pile-up of two single scatter events [2]. This is defined as the coincidence between two single scatter (SS) events, within the 0.250 ms total drift length used in LUX [2, 54, 140]. We used this time difference, because only the events with a time difference lower than 250 μs can mimetize an event with a MiDM event typology. We selected the events from the Run IV WIMP search data with one S1 and one S2, and calculated the event rate for those events [2, 139].

We applied the same quality cuts used in the main analysis, namely the bad area cut and the fiducial cut. The fiducial cut is a combination of a radial and a drift time cut. It is a cut in the volume of the detector that includes only events with a distance to the wall larger than 3 cm in S2 coordinates and a drift time between 50 and 300 μs [54, 53].

Additionally, we applied a cut on the S1 area, selecting the events with an S1 area lower than 300 phd and 1000 phd for the first and second pulses, respectively. For the first pulse, a cut on the S1 area of 300 phd roughly corresponds to an energy of 100 keV$_{ee}$, being consistent with a nuclear recoil, NR. For the second pulse, a cut on the S1 area of 1000 phd roughly corresponds to an energy of 200 keV$_{ee}$, being consistent with an electronic recoil, ER.

We also applied a spike count cut on the S1 area, accepting only the events with a minimum of two detected photons for two different PMTs [7, 78].

Finally, we also removed the datasets with an elevated rate of $^{83\mathrm{m}}$Kr events. To identify those datasets, we measured the rate of events with reconstructed energy between 37.5 and 45.5 keV for each dataset, once the average energy for a $^{83\mathrm{m}}$Kr is 41.5 keV [84]. Datasets with an event rate larger than 0.01 evts/s were not considered within this region.

The single scatter event rate is given by

$$\frac{\Delta R_{1S1,1S2}}{\Delta t} = \frac{N_{SSi}}{\tau_{total}} \tag{4.16}$$

where $\tau_{total} \sim 293$ days, is the total livetime and N_{SSi} is the number of single scatter events for the first and second pulses, respectively. For the first pulse, we obtained a number of single scatter events, N_{SS_a}, of 18386 events. For second pulse, we obtained a number of single scatter evts, N_{SS_b}, of 69148 evts.

From the equation 4.16, we obtained a single scatter event rate obtained for the first and second 1S1 1S2, $\frac{\Delta R_{1S11,1S21}}{\Delta t}$ and $\frac{\Delta R_{1S12,1S22}}{\Delta t}$, of 7.2×10^{-4} evts/s and 2.7×10^{-3} evts/s , respectively. For two single scatter events, the coincidence rate, $R_{coincidence}$ is given by

$$R_{coincidence} = \frac{\Delta R_{1S1,1S2}}{\Delta t}\frac{\Delta R_{1S1,1S2}}{\Delta t}\tau \tag{4.17}$$

where τ=250 μs and n=1, for the single scatter event case. The τ= 250 μs is in the interval of the drift time cut, between 50 and 300 μs. We obtained a coincidence rate, $R_{coincidence}$, of 4.8×10^{-10} evts/s.

The total number of coincidence events during the Run IV, $N_{coincidence}$, is given by

$$N_{coincidence} = R_{coincidence}\tau_{total} \tag{4.18}$$

From the equation 4.22, we obtained a number of coincidence events for two single scatter events, $N_{coincidence}$, of 1.2×10^{-2} events for the Run IV data. Once this is a very low value, we wouldn't need to consider the contributions from this background source in an eventual MiDM background model.

4.4.3 Pile-up between one S1 and two S2s and a S1 peak without any correlated S2

The third background source considered corresponds to the pile-up between a double scatter with one S1 and two S2 pulses and a S1 peak without any correlated S2 [2]. A double scatter with one S1 and two S2 pulses is mainly created by γ rays. The event with one S1 and zero S2 pulses is mainly caused by energy depositions in "dead" zones of the detector, which means regions in the detector with no applied electric field. In these regions, the applied electric field is not enough to drift the charge to the surface that separates the liquid and the gas phase, which means that no S2 signal is observed. Those pulses can also be caused by PMT after-pulsing and dark counting on the PMTs [120, 122].

The individual contributions from this background source were estimated in a similar way that the one used in the previous section. Although, this time we selected events with one S1 and without any correlated S2s and events with one S1 and two S2 pulses. To reconstruct the energy for each pair, we associated randomly an S2 pulse from an event with two S2s, with the S1 pulse from an event without S2 pulses.

We defined an upper value for the contributions from this background source, by applying some quality cuts on he reconstructed energies, E_a and E_b, in order to obtain a number of background events below the limit of 0.1 evts to be able to still assume a background free experiment [2, 139]. Most of these cuts were also used in the section 4.4.2, such as the fiducial cut, the bad area cut, the spike count cut and a cut on the datasets with an elevated rate of ^{83m}Kr events. Additionally, we also applied a quality cut on the S2 pulse area for the first and second S2 pulses, $S2_a$ and $S2_b$, limiting their pulse areas to 200 phd.

We also applied a cut on the region of interest of the reconstructed energies of the first and second pulses, E_a and E_b, excluding events with a S1 signal higher than 100 keV for the first pulse (E_a < 100 keV) and an energy value higher than 200 keV for the second pulse (E_b < 200 keV). In spite of expecting a nuclear recoil, NR, for MiDM's first pulse, we reconstructed the energy of the first pulse, E_a, as an electronic recoil, ER, and the energy of the second pulse, E_b, as a nuclear recoil, NR [2]. Using the equation 4.12 from the section 4.4.1, and considering a maximum energy for the first pulse, E_a, of 300 keV, we obtained a maximum of 60 keV for the maximum value of the energy of the second pulse, E_b. Although, we used a maximum value of 100 keV for E_b to have some interval of confidence, since we are interested in a upper value of this background.

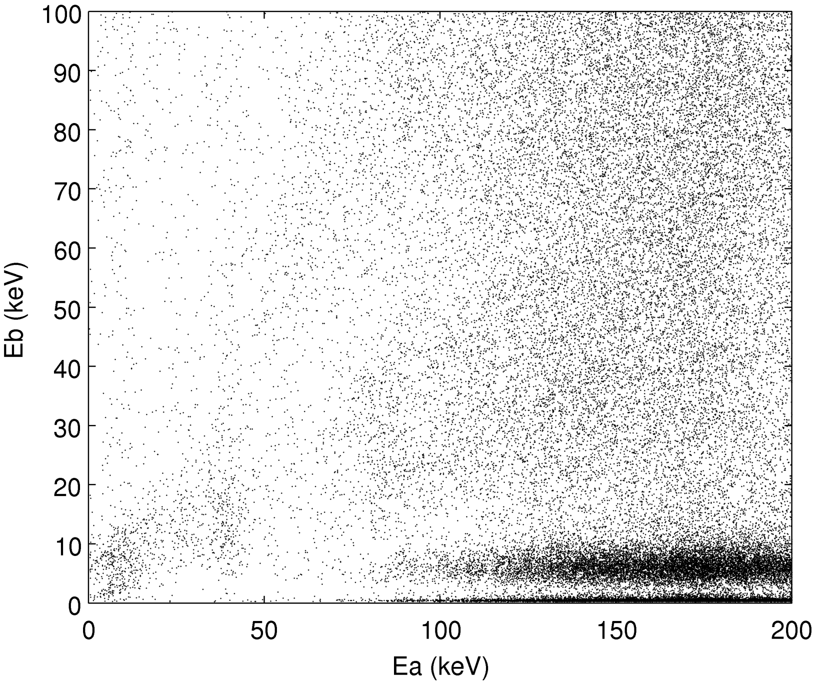

Figure 4.17: Second pulse reconstructed energy, E_b, as a function of the first pulse reconstructed energy, E_a.

The figure 4.17 shows the second pulse reconstructed energy, E_b, as a function of the first pulse reconstructed energy, E_a. Most of the coincidence events is located in the range of first pulse reconstructed energies, E_a, between 100-200 keV. For the nuclear recoil, we considered a region of interest between 0 and 100 keV, roughly corresponding to 300 phd for the non-corrected S1 pulse. For the electronic recoil, we considered a region of interest between 0 and 200 keV, roughly corresponding to 1000 phd for the non-corrected S1 pulse.

The event rates for one S1 without any correlated S2, $\frac{\Delta R_{1S10S2mi}}{\Delta t}$, and one S1 and two S2, $\frac{\Delta R_{1S1,2S2mi}}{\Delta t}$, are given by the following equations

$$\frac{\Delta R_{1S10S2mi}}{\Delta t} = \frac{N_{SSmi}}{\tau_{0S2}} \tag{4.19}$$

and

$$\frac{\Delta R_{1S1,2S2mi}}{\Delta t} = \frac{N_{SSmi}}{\tau_{total}} \tag{4.20}$$

where $\tau_{0S2} \sim 92$ days, and $\tau_{total} \sim 293$ days. N_{SSmi} are the number of single scatter events for $i=$ 300 and 1000 phd, corresponding to the nuclear and electronic recoils, respectively. For both NR and ER, we applied a cut on the area of the S1 pulse of 300 and 1000 phd, respectively. The obtained number of single-scatter events for NR and ER, N_{SSm300} and $N_{SSm1000}$, is 27455 and 116622 evts respectively. The table 4.4 shows the event rates in the region of interest of nuclear and electronic recoils, respectively. For both recoils, the energy cuts in the region of interest were taken from XENON100 [2]. We used the event rates shown in the table 4.4 to obtain the coincidence rates between one S1 and zero S2, and one S1 and two S2, $R_{coi(m_i m_j)}$, as

Table 4.4: Event rate for one S1 and zero S2, and one S1 and two S2.

	Event Rate (evts/s) 1S1 + 0S2	Event Rate (evts/s) 1S1 + 2S2
< 300	0.58	1.1×10^{-3}
< 1000	0.89	4.6×10^{-3}

$$R_{coi(m_i m_j)} = \tau \frac{\Delta R_{1S1,2S2mi}}{\Delta t} \frac{\Delta R_{1S1,2S2mi}}{\Delta t} \tag{4.21}$$

where $i, j = 300$ or 1000 and $\tau = 250$ μs. We obtained a coincidence rate, $R_{coi(m_{300} m_{1000})}$, of 6.6 $\times 10^{-7}$ evts/s and a coincidence rate, $R_{coi(m_{1000} m_{300})}$, of 2.4 $\times 10^{-7}$ evts/s.

$$N_{coi(m_i m_j)} = R_{coi(m_i m_j)} \tau_{total} \tag{4.22}$$

We obtained a number of coincidences, $N_{coi(m_{300} m_{1000})}$ and $N_{coi(m_{1000} m_{300})}$, of 16.9 and 6.1 evts, respectively. Finally, we obtained the total number of coincidence events, N_{total}, given by

$$N_{total} = 0.5[N_{coi(m_i m_j)} + N_{coi(m_i m_j)}] \tag{4.23}$$

We obtained a total number of pile-up events, N_{total}, of 11 evts. This high value implies that the experiment is not background free, because it is well above the limit of 0.1 evts to be able to still assume a background free experiment [139, 2]. Although, we could solve this by considering the first pulse as a nuclear recoil, NR. In LUX, there is a 99.8 % probability of one electronic recoil pulse to have an S2 above the median of the nuclear recoil, meaning that 0.2 % of the first pulse can be mistaken with an NR. If we had applied this condition, we would obtain a negligible background, with a total number of coincidence events, N_{total}, less than 0.1.

Chapter 5

Conclusion

The work presented in this thesis explored the direct detection of dark matter, studying the inelastic scattering between dark matter and standard model particles [1, 2, 3]. We used data from the LUX experiment to study Magnetic inelastic Dark Matter (MiDM), one of the proposed models to explain the discrepancies between DAMA/LIBRA and other direct detection dark matter results [2, 3].

In this context, we focused on the theoretical predictions for the MiDM event rate. For that purpose, we used an Effective Field Theory approach, which is based on a set of WIMP-nucleon operators that are subject of two basic symmetries, conservation of momentum and Galilean invariance [101]. Then, obtained a limit of $2.098 \times 10^{-5} \mu_{nuc}$ for the WIMP magnetic moment of an experiment with a negligible background, using the parameters ($m_{\chi_1} = 58.0$ GeV/c^2, $\mu_{\chi_1} = 0.0018$ μ_{nuc}, $\delta = 111.7$ keV) with the nuclear magneton μ_{nuc}, one of the two best fit parameters from the DAMA/LIBRA experiment [2, 139].

We also used the LUX data to study the possible event typologies for MiDM, using some quality cuts to remove events that represented a fake signal and studying some of the properties of the S1 and S2 pulses. We studied these pulses properties to distinguish between the different event typologies that could represent a signal produced by MiDM, and also to exclude event typologies caused by background sources. To study the background sources associated with MiDM, and for all the backgrounds studied we obtained a number of events during all the run IV of less than 0.1 and thus these contributions can be discarded.

We can complete the work presented in this thesis in several ways: we considered an efficiency of 100 % for this analysis, but we still need to study the factors that affect the efficiency, namely the minimum time difference between the 2 S1 pulses of 2 μs, the finite size of the LUX detector that limits the chance to detect γ rays from the WIMP de-excitation, γ rays can escape from the fiducial volume of the detector and the efficiencies of the quality cuts applied in the MiDM Analysis [2, 54]. We should also add the S2 pulse width contribution to the calculations on the pulse pairing analysis, and apply a cut on the first pulse reconstructed energy, E_a, considering a nuclear recoil ($E_a < 200$ keV), as expected for MiDM. This is in contrast with our analysis, as we applied a cut on the first pulse reconstructed energy, E_a, considering a electronic recoil ($E_a < 100$ keV) instead. We can also use the number of background events from ^{85}Kr to include the ER/NR discrimination in the MiDM background source analysis.

Most of the operations of the next generation experiments will occur during the next decade, and they will initiate their activity with masses that will be much higher than the total detector mass of 370 kg, and and a fiducial volume mass of 100 kg used during LUX operations [47, 50, 52, 53]. Examples of these experiments are LUX-ZEPLIN (LZ) and XENONnT, with total detector masses of 10 and 8.4 tonnes, and active volume masses on the detector of 7 and 5.9 tonnes, respectively [48, 52]. These experiments have an expected limit on the WIMP-nucleon spin-independent cross-section $\sim 1.4 \times 10^{-48}$ cm^2 for a 40 GeV/c^2 mass and 1.6×10^{-48} cm^2 for a 50 GeV/c^2, respectively, at a 90 % Confidence Level (C.L.) [48, 52]. This expected limits are much lower than the expected for LUX, with an expected limit on the WIMP-nucleon spin-independent cross-section of 2×10^{-46} cm^2 for a WIMP mass around 50 GeV/c^2 [53]. For future analysis, the data from these experiments will be very useful to test models as Magnetic inelastic Dark Matter [2, 50, 52, 53].

List of Figures

List of Tables

Bibliography

[1] Lin Tongyan. "Signals of Particle Dark Matter". PhD Dissertation. Harvard University, 2012. URL: http://nrs.harvard.edu/urn-3:HUL.InstRepos:9527316.

[2] E. Aprile et al. "Search for magnetic inelastic dark matter with XENON100". In: *Journal of Cosmology and Astroparticle Physics* 2017.10 (Oct. 2017), pp. 039–039. ISSN: 1475-7516. DOI: 10.1088/1475-7516/2017/10/039. URL: http://dx.doi.org/10.1088/1475-7516/2017/10/039.

[3] Spencer Chang, Neal Weiner, and Itay Yavin. "Magnetic inelastic dark matter". In: *Physical Review D* 82.12 (Dec. 2010). ISSN: 1550-2368. DOI: 10.1103/physrevd.82.125011. URL: http://dx.doi.org/10.1103/PhysRevD.82.125011.

[4] Chang Lee. "Mitigation of backgrounds for the Large Underground Xenon Dark Matter experiment." PhD Dissertation. Case Western Reserve University, May 2015. URL: http://rave.ohiolink.edu/etdc/view?acc_num=case1427482791.

[5] Guillaume Plante. "The XENON100 Dark Matter Experiment: Design, Construction, Calibration and 2010 Search Results with Improved Measurement of the Scintillation Response of Liquid Xenon to Low-Energy Nuclear Recoils". PhD Dissertation. Columbia University (main), 2012. URL: https://inspirehep.net/literature/1515420.

[6] Ernst Fischer. *The properties of dark matter*. 2011. arXiv: 1104.2525 `[physics.gen-ph]`. URL: https://arxiv.org/abs/1104.2525.

[7] Sally Shaw. "Dark Matter Searches with the LUX and LZ Experiments". PhD Dissertation. University College London, Nov. 2016. URL: https://discovery.ucl.ac.uk/id/eprint/1532174/4/SallyShaw_Thesis_UCL_2016.pdf.

[8] Patrick Phelps. "The LUX Dark Matter experiment: Detector performance and energy calibration." PhD Dissertation. Case Western Reserve University, Aug. 2014. URL: http://rave.ohiolink.edu/etdc/view?acc_num=case1404908222.

[9] Eryk Filip Druszkiewicz. "Digital Advances in Triggering and Data Acquisition Systems for Large Scale Dark Matter Search Experiments". PhD Dissertation. University of Rochester, Jan. 2017. URL: https://ui.adsabs.harvard.edu/abs/2017PhDT.......125D.

[10] Paulo Bras. "Finding a needle in a haystack: Background studies & WIMP detection efficiency in LUX". Master Thesis Dissertation. Coimbra: University of Coimbra, 2015. URL: https://estudogeral.sib.uc.pt/handle/10316/29834.

[11] Rachel Louise Mannino. "Measuring Backgrounds From 85Kr and 210Bi to Improve Sensitivity of Dark Matter Detectors". PhD thesis. Texas A&M University, Jan. 2017. URL: https://ui.adsabs.harvard.edu/abs/2017PhDT.......331M.

[12] Salma Alrasheed. *Principles of Mechanics: Fundamental University Physics*. Berlin, Germany: Springer, 2019.

[13] Michael Richmond. *Using the virial theorem: the mass of a cluster of galaxies*. 2003. URL: http://spiff.rit.edu/classes/phys440/lectures/gal_clus/gal_clus.html.

[14] F. Zwicky. "On the Masses of Nebulae and of Clusters of Nebulae". In: *The Astrophysical Journal* 86 (Oct. 1937), p. 217. DOI: 10.1086/143864.

[15] K. Freese. "Review of Observational Evidence for Dark Matter in the Universe and in upcoming searches for Dark Stars". In: *EAS Publications Series* 36 (2009), pp. 113–126. ISSN: 1638-1963. DOI: 10.1051/eas/0936016. URL: http://dx.doi.org/10.1051/eas/0936016.

[16] Nehrkorn Curt. "Testing the WIMP hypothesis with the LUX dark matter detector." PhD Dissertation. Santa Barbara (main): University of California, 2019. URL: https://inspirehep.net/literature/1771764.

[17] John Kwong. "The Development of Two-Phase Xenon Dark Matter Detectors". PhD Dissertation. Princeton University, June 2009. URL: http://inspirehep.net/record/1465895/files/J.Kwongthesis.pdf.

[18] Ricardo Peres. "Contributions to the Xenon dark matter experiment: Simulations of detector response to calibration sources and electric field optimization". Master Thesis Dissertation. Coimbra: University of Coimbra, 2018. URL: https://estudogeral.uc.pt/handle/10316/86267?mode=full.

[19] Daniel Hogan. "Techniques for Inelastic Effective Field Theory Measurements with the Large Underground Xenon Experiment". PhD Dissertation. Berkeley: University of California, 2018. URL: https://escholarship.org/uc/item/6p9899hw.

[20] Fabio Valerio Massoli. "The XENON1T experiment:Monte Carlo background estimation and sensitivity curves study". PhD Dissertation. Universitá di Bologna, 2015. URL: http://amsdottorato.unibo.it/6776/1/Massoli_FabioValerio_tesi.pdf.

[21] J. A. Mock. "A Search for Dark Matter with the Large Underground Xenon Detector". PhD Dissertation. 2008.

[22] Federica Agostini. "The XENON project: backgrounds and new results". PhD Dissertation. Scuola Internazionale Superiore di Studi Avanzati, Aug. 2017. URL: https://web.bo.infn.it/xenon/sito_web_Bologna/tesi/tesi_agostini_dottorato.pdf.

[23] Attila Dobi. "Measurement of the electron recoil band of the LUX Dark Matter detector with a Tritium Calibration Source." PhD Dissertation. University of Maryland, 2014. DOI: https://doi.org/10.13016/M24P5P.

[24] Evan Pease. "Rare-event searches in liquid xenon with the LUX and LUX-ZEPLIN detectors". PhD Dissertation. Yale University, 2017. URL: http://teacher.pas.rochester.edu/pub/Lux/LuxRequiredReading/2017_EPease_Yale_Thesis.pdf.

[25] Edward Reichard Shayne. "The search for dark matter in xenon: Innovative calibration strategies and novel search channels". PhD Dissertation. Purdue

University, Dec. 2016. URL: https://docs.lib.purdue.edu/cgi/viewcontent.cgi?article=2209&context=open_access_dissertations.

[26] Louis William IV Kastens. "Calibration of Liquid Xenon Time Projection Chambers for the Direct Detection of Dark Matter". PhD Dissertation. Yale University, Jan. 2013. URL: https://ui.adsabs.harvard.edu/abs/2013PhDT.......104K.

[27] Dongqing Huang. "Ultra-Low Energy Calibration of the LUX and LZ Dark Matter Detectors". PhD Dissertation. Brown University, May 2019. URL: https://drive.google.com/file/d/11eL-WPC0FXG4u0ukn92sm9OGt8jMFydO/view.

[28] Elizabeth Magnis Boulton. "Applications of Two-Phase Xenon Time Projection Chambers: Searching for Dark Matter and Special Nuclear Materials". PhD Dissertation. Yale University, 2019. URL: http://hdl.handle.net/10079/bibid/14882148.

[29] Adam Bailey. "Dark Matter Searches and Study of Electrode Design in LUX and LZ". PhD Dissertation. London: Imperial College, 2016. URL: https://spiral.imperial.ac.uk/handle/10044/1/41878.

[30] Gianfranco Bertone and Dan Hooper. "History of dark matter". In: *Reviews of Modern Physics* 90.4 (Oct. 2018). ISSN: 1539-0756. DOI: 10.1103/revmodphys.90.045002. URL: http://dx.doi.org/10.1103/RevModPhys.90.045002.

[31] Katayun Kamdin. "A Search for Lightly Ionizing Particles in the LUX Detector and Research and Development For Future Liquid Xenon Time Projection Chambers." PhD Dissertation. Berkeley: University of California, 2018. URL: https://escholarship.org/uc/item/9ck617mz.

[32] Sabine Hossenfelder. *The Bullet Cluster as Evidence against Dark Matter*. 2017. URL: http://backreaction.blogspot.com/2017/01/the-bullet-cluster-as-evidence-against.html.

[33] Richard Knoche. "Signal corrections and calibrations in the LUX Dark Matter detector." PhD Dissertation. University of Maryland, 2016. URL: http://hdl.handle.net/1903/19300.

[34] Ruth Durrer. "The cosmic microwave background: the history of its experimental investigation and its significance for cosmology". In: *Classical and Quantum Gravity* 32.12 (June 2015), p. 124007. ISSN: 1361-6382. DOI: 10.1088/0264-9381/32/12/124007. URL: http://dx.doi.org/10.1088/0264-9381/32/12/124007.

[35] N. Aghanim et al. "Planck 2015 results. XI. CMB power spectra, likelihoods, and robustness of parameters". In: *Astronomy & Astrophysics* 594 (Sept. 2016), A11. ISSN: 1432-0746. DOI: 10.1051/0004-6361/201526926. URL: http://dx.doi.org/10.1051/0004-6361/201526926.

[36] Jon Balajthy. "Purity monitoring techniques and electronic energy deposition properties in liquid xenon time projection chambers." PhD Dissertation. University of Maryland, 2018. URL: http://hdl.handle.net/1903/20824.

[37] Samuel Joseph Witte. "Dark Matter Signals". PhD Dissertation. Los Angeles: University of California, 2017. URL: https://escholarship.org/uc/item/3ct8q342.

[38] Nicole A. Larsen. "An Effective Field Theory Analysis of the First LUX Dark Matter Search". PhD Dissertation. Yale University, May 2016. URL: https://search.proquest.com/openview/5357701f9b1e1a1955854858e69fa076/1?pq-origsite=gscholar&cbl=18750&diss=y.

[39] R. Adhikari et al. "A White Paper on keV sterile neutrino Dark Matter". In: *Journal of Cosmology and Astroparticle Physics* 2017.01 (Jan. 2017), pp. 025–025. ISSN: 1475-7516. DOI: 10.1088/1475-7516/2017/01/025. URL: http://dx.doi.org/10.1088/1475-7516/2017/01/025.

[40] Mongkol Moongweluwan. "Measurements of the LUX Trigger Efficiency". PhD Dissertation. University of Rochester, 2018. URL: http://hdl.handle.net/1802/34290.

[41] Leszek Roszkowski, Enrico Maria Sessolo, and Sebastian Trojanowski. "WIMP dark matter candidates and searches—current status and future prospects". In: *Reports on Progress in Physics* 81.6 (May 2018), p. 066201. ISSN: 1361-6633. DOI: 10.1088/1361-6633/aab913. URL: http://dx.doi.org/10.1088/1361-6633/aab913.

[42] Thomas Hambye et al. “Dark matter from dark photons: A taxonomy of dark matter production”. In: *Physical Review D* 100.9 (Nov. 2019). ISSN: 2470-0029. DOI: 10.1103/physrevd.100.095018. URL: http://dx.doi.org/10.1103/PhysRevD.100.095018.

[43] Annika H. G. Peter et al. *WIMP physics with ensembles of direct-detection experiments*. 2013. DOI: 10.1016/j.dark.2014.10.006. arXiv: `1310.7039 [astro-ph.CO]`. URL: https://arxiv.org/abs/1310.7039.

[44] Lucie Tvrznikova. “Sub-GeV Dark Matter Searches and Electric Field Studies for the LUX and LZ Experiments”. PhD Dissertation. Yale University, 2019. URL: https://arxiv.org/abs/1904.08979.

[45] Marc Schumann. “Direct detection of WIMP dark matter: concepts and status”. In: *Journal of Physics G: Nuclear and Particle Physics* 46.10 (Aug. 2019), p. 103003. ISSN: 1361-6471. DOI: 10.1088/1361-6471/ab2ea5. URL: http://dx.doi.org/10.1088/1361-6471/ab2ea5.

[46] Gaudenz Kessler. “Inelastic WIMP-Nucleus Interactions in XENON100 and Cables and Connectors for XENON1T”. PhD Dissertation. University of Zurich, 2016. DOI: https://doi.org/10.5167/uzh-127035.

[47] E. Aprile et al. “XENON1T dark matter data analysis: Signal reconstruction, calibration, and event selection”. In: *Physical Review D* 100.5 (Sept. 2019). ISSN: 2470-0029. DOI: 10.1103/physrevd.100.052014. URL: http://dx.doi.org/10.1103/PhysRevD.100.052014.

[48] Julien Masbou. *Latest results from XENON1T and status of the XENONnT-experiment*. 2019. URL: https://indico.cern.ch/event/828038/contributions/3583163/attachments/1956888/3250938/2019_12_05_TeVPA2019_XENON.pdf.

[49] J. Aalbers et al. “DARWIN: towards the ultimate dark matter detector”. In: *Journal of Cosmology and Astroparticle Physics* 2016.11 (Nov. 2016), pp. 017–017. ISSN: 1475-7516. DOI: 10.1088/1475-7516/2016/11/017. URL: http://dx.doi.org/10.1088/1475-7516/2016/11/017.

[50] E. Aprile et al. “Physics reach of the XENON1T dark matter experiment.” In: *Journal of Cosmology and Astroparticle Physics* 2016.04 (Apr. 2016), pp. 027–027. ISSN: 1475-7516. DOI: 10.1088/1475-7516/2016/04/027. URL: http://dx.doi.org/10.1088/1475-7516/2016/04/027.

[51] Kevin Thieme. *DARWIN – a next-generation liquid xenon observatory for dark matter and neutrino physics*. 2019. URL: https://indico.cern.ch/event/577856/contributions/3420279/attachments/1877626/3092486/DARWIN_EPS-HEP2019_Kevin_Thieme.pdf.

[52] D. S. Akerib et al. “Projected WIMP sensitivity of the LUX-ZEPLIN dark matter experiment”. In: *Physical Review D* 101.5 (Mar. 2020). ISSN: 2470-0029. DOI: 10.1103/physrevd.101.052002. URL: http://dx.doi.org/10.1103/PhysRevD.101.052002.

[53] D.S. Akerib et al. “The Large Underground Xenon (LUX) experiment”. In: *Nuclear Instruments and Methods in Physics Research Section A: Accelerators, Spectrometers, Detectors and Associated Equipment* 704 (Mar. 2013), pp. 111–126. ISSN: 0168-9002. DOI: 10.1016/j.nima.2012.11.135. URL: http://dx.doi.org/10.1016/j.nima.2012.11.135.

[54] D. S. Akerib et al. “Results from a Search for Dark Matter in the Complete LUX Exposure”. In: *Physical Review Letters* 118.2 (Jan. 2017). ISSN: 1079-7114. DOI: 10.1103/physrevlett.118.021303. URL: http://dx.doi.org/10.1103/PhysRevLett.118.021303.

[55] Cláudio Frederico Pascoal da Silva. *Dark Matter Searches with LUX*. 2017. arXiv: 1710.03572 `[hep-ex]`. URL: https://arxiv.org/abs/1710.03572.

[56] Cláudio Silva. “Study of the Reflectance Distributions of Fluoropolymers and Other Rough Surfaces with Interest to Scintillation Detectors”. PhD Dissertation. Coimbra: University of Coimbra, 2009. URL: http://hdl.handle.net/10316/14202.

[57] “Observation of two-neutrino double electron capture in 124Xe with XENON1T”. In: *Nature* 568.7753 (Apr. 2019), pp. 532–535. ISSN: 1476-4687. DOI: 10.1038/s41586-019-1124-4. URL: http://dx.doi.org/10.1038/s41586-019-1124-4.

[58] J. B. Albert et al. “Improved measurement of the$2\nu\beta\beta$half-life of136Xe with the EXO-200 detector”. In: *Physical Review C* 89.1 (Jan. 2014). ISSN: 1089-490X. DOI: 10.1103/physrevc.89.015502. URL: http://dx.doi.org/10.1103/PhysRevC.89.015502.

[59] Various Authors. *Xenon isotopes.* 2019. URL: https://en.wikipedia.org/wiki/Isotopes_of_xenon.

[60] Todd Helmenstine. *Periodic table electronegativity.* 2017. URL: https://sciencenotes.org/wp-content/uploads/2017/10/PeriodicTableElectronegativity.pdf.

[61] V Chepel and H Araújo. “Liquid noble gas detectors for low energy particle physics”. In: *Journal of Instrumentation* 8.04 (Apr. 2013), R04001–R04001. ISSN: 1748-0221. DOI: 10.1088/1748-0221/8/04/r04001. URL: http://dx.doi.org/10.1088/1748-0221/8/04/R04001.

[62] E. Aprile and T. Doke. “Liquid xenon detectors for particle physics and astrophysics”. In: *Reviews of Modern Physics* 82.3 (June 2010), pp. 2053–2097. ISSN: 1539-0756. DOI: 10.1103/revmodphys.82.2053. URL: http://dx.doi.org/10.1103/RevModPhys.82.2053.

[63] E. Dahl. “The physics of background discrimination in liquid xenon, and first results from Xenon10 in the hunt for WIMP dark matter.” PhD Dissertation. Princeton University, Sept. 2009. URL: http://inspirehep.net/record/1374815/files/E.Dahlthesis.pdf.

[64] Angel Manzur. “Relative scintillation efficiency of liquid xenon in the XENON10 direct dark matter search”. PhD Dissertation. Yale University, Jan. 2009. URL: https://ui.adsabs.harvard.edu/abs/2009PhDT........33M.

[65] Alastair Edward Currie. “Direct searches for WIMP dark matter with ZEPLIN-III”. PhD Dissertation. Imperial College London, July 2012. URL: http://hdl.handle.net/10044/1/9980.

[66] M Szydagis et al. “NEST: a comprehensive model for scintillation yield in liquid xenon”. In: *Journal of Instrumentation* 6.10 (Oct. 2011), P10002–P10002. ISSN: 1748-0221. DOI: 10.1088/1748-0221/6/10/p10002. URL: http://dx.doi.org/10.1088/1748-0221/6/10/P10002.

[67] Peter Sorensen and Carl Eric Dahl. “Nuclear recoil energy scale in liquid xenon with application to the direct detection of dark matter”. In: *Physical Review D* 83.6 (Mar. 2011). ISSN: 1550-2368. DOI: 10.1103/physrevd.83.063501. URL: http://dx.doi.org/10.1103/PhysRevD.83.063501.

[68] Henrique Araújo. *Shedding light on Dark Matter with LUX*. 2014. URL: http://www.ep.ph.bham.ac.uk/general/seminars/slides/Henrique-Araujo-2014.pdf.

[69] D. S. Akerib et al. “Liquid xenon scintillation measurements and pulse shape discrimination in the LUX dark matter detector”. In: *Physical Review D* 97.11 (June 2018). ISSN: 2470-0029. DOI: 10.1103/physrevd.97.112002. URL: http://dx.doi.org/10.1103/PhysRevD.97.112002.

[70] Marc Schumann. “Dual-phase liquid xenon detectors for dark matter searches”. In: *Journal of Instrumentation* 9.08 (June 2014), pp. C08004–C08004. ISSN: 1748-0221. DOI: 10.1088/1748-0221/9/08/c08004. URL: http://dx.doi.org/10.1088/1748-0221/9/08/C08004.

[71] D. S. Akerib et al. “Improved measurements of the β -decay response of liquid xenon with the LUX detector”. In: *Physical Review D* 100.2 (July 2019). ISSN: 2470-0029. DOI: 10.1103/physrevd.100.022002. URL: http://dx.doi.org/10.1103/PhysRevD.100.022002.

[72] D. S. Akerib et al. “Calibration, event reconstruction, data analysis, and limit calculation for the LUX dark matter experiment”. In: *Physical Review D* 97.10 (May 2018). ISSN: 2470-0029. DOI: 10.1103/physrevd.97.102008. URL: http://dx.doi.org/10.1103/PhysRevD.97.102008.

[73] Carlos Faham. “Prototype, Surface Commissioning and Photomultiplier Tube Characterization for the Large Underground Xenon (LUX) Direct Dark Matter Search Experiment”. PhD Dissertation. Brown University, 2014. DOI: https://doi.org/10.7301/Z0QV3JV5.

[74] Dev Ashish Kaithan. “Pulse Shape Discrimination in the LUX Dark Matter Detector”. PhD Dissertation. Rochester,New York: University of Rochester, 2019. URL: http://hdl.handle.net/1802/35473.

[75] F. Neves et al. “Measurement of the absolute reflectance of polytetrafluoroethylene (PTFE) immersed in liquid xenon”. In: *Journal of Instrumentation* 12.01 (Jan. 2017), P01017–P01017. ISSN: 1748-0221. DOI: 10.1088/1748-0221/12/01/p01017. URL: http://dx.doi.org/10.1088/1748-0221/12/01/P01017.

[76] Jeremy J. Chapman. “First WIMP Search Results from the LUX Dark Matter Experiment”. PhD Dissertation. Brown University, 2014. URL: https://escholarship.org/uc/item/6p9899hw.

[77] Various Authors. *Table de Radionucléides*. 2008. URL: http://www.nucleide.org/DDEP_WG/Nuclides/Cf-252_tables.pdf.

[78] D. S. Akerib et al. “Tritium calibration of the LUX dark matter experiment”. In: *Physical Review D* 93.7 (Apr. 2016). ISSN: 2470-0029. DOI: 10.1103/physrevd.93.072009. URL: http://dx.doi.org/10.1103/PhysRevD.93.072009.

[79] Claus Grupen. *Introduction to radiation protection:practical knowledge for handling radioactive sources*. Berlin, Germany: Springer, 2010.

[80] R.F. Lang et al. “Characterization of a deuterium–deuterium plasma fusion neutron generator”. In: *Nuclear Instruments and Methods in Physics Research Section A: Accelerators, Spectrometers, Detectors and Associated Equipment* 879 (Jan. 2018), pp. 31–38. ISSN: 0168-9002. DOI: 10.1016/j.nima.2017.10.001. URL: http://dx.doi.org/10.1016/j.nima.2017.10.001.

[81] LUX Collaboration et al. *Low-energy (0.7-74 keV) nuclear recoil calibration of the LUX dark matter experiment using D-D neutron scattering kinematics*. 2016. arXiv: 1608.05381 `[physics.ins-det]`. URL: https://arXiv.org/abs/1608.05381.

[82] S. Rosendahl et al. “A novel83mKr tracer method for characterizing xenon gas and cryogenic distillation systems”. In: *Journal of Instrumentation* 9.10 (Oct. 2014), P10010–P10010. DOI: 10.1088/1748-0221/9/10/p10010. URL: https://doi.org/10.1088%5C%2F1748-0221%5C%2F9%5C%2F10%5C%2Fp10010.

[83] Sergej Schneider. “Measurement of Kr-83m Doping in Xenon Gas for Calibration and Tracer Applications”. Bachelor Thesis Dissertation. Universit¨at M¨unster, Aug. 2012. URL: https://www.uni-muenster.de/Physik.KP/AGWeinheimer/Files/theses/Bachelor_Sergej_Schneider.pdf.

[84] D. S. Akerib et al. “Kr83m calibration of the 2013 LUX dark matter search”. In: *Physical Review D* 96.11 (Dec. 2017). ISSN: 2470-0029. DOI: 10.1103/physrevd.96.112009. URL: http://dx.doi.org/10.1103/PhysRevD.96.112009.

[85] D.S. Akerib et al. “3D modeling of electric fields in the LUX detector”. In: *Journal of Instrumentation* 12.11 (Nov. 2017), P11022–P11022. ISSN: 1748-0221. DOI: 10.1088/1748-0221/12/11/p11022. URL: http://dx.doi.org/10.1088/1748-0221/12/11/P11022.

[86] G. Barello, Spencer Chang, and Christopher A. Newby. “A model independent approach to inelastic dark matter scattering”. In: *Physical Review D* 90.9 (Nov. 2014). ISSN: 1550-2368. DOI: 10.1103/physrevd.90.094027. URL: http://dx.doi.org/10.1103/PhysRevD.90.094027.

[87] Brian Tennyson. “Two-Phase Liquid-Gas Xenon Time Projection Chambers:Theory, Applications, and Analysis”. PhD Dissertation. Yale University, 2017.

[88] Gregory Choppin *et al. Radiochemistry and Nuclear Chemistry*. Cambridge, Massachusetts, United States: Academic Press, 2013.

[89] Gerhard Hübschen *et al. Materials Characterization Using Nondestructive Evaluation (NDE) Methods*. Sawston, Cambridge, United Kingdom: Woodhead Publishing, 2016.

[90] Spencer Chang et al. “Inelastic dark matter in light of DAMA/LIBRA”. In: *Physical Review D* 79.4 (Feb. 2009). ISSN: 1550-2368. DOI: 10.1103/physrevd.79.043513. URL: http://dx.doi.org/10.1103/PhysRevD.79.043513.

[91] Christopher McCabe. “Astrophysical uncertainties of dark matter direct detection experiments”. In: *Physical Review D* 82.2 (June 2010). ISSN: 1550-2368. DOI: 10.1103/physrevd.82.023530. URL: http://dx.doi.org/10.1103/PhysRevD.82.023530.

[92] Nassim Bozorgnia et al. "Halo-independent methods for inelastic dark matter scattering". In: *Journal of Cosmology and Astroparticle Physics* 2013.07 (June 2013), pp. 049–049. ISSN: 1475-7516. DOI: 10.1088/1475-7516/2013/07/049. URL: http://dx.doi.org/10.1088/1475-7516/2013/07/049.

[93] N. Wyn Evans, Ciaran A. J. O'Hare, and Christopher McCabe. *SHM^{++}: A Refinement of the Standard Halo Model for Dark Matter Searches in Light of the Gaia Sausage*. 2018. arXiv: 1810.11468 `[astro-ph.GA]`. URL: https://arxiv.org/abs/1810.11468v2.

[94] A. Liam Fitzpatrick et al. *Model Independent Direct Detection Analyses*. 2012. arXiv: 1211.2818 `[hep-ph]`. URL: https://arxiv.org/abs/1211.2818.

[95] Gopolang Mohlabeng. "Revisiting the dark photon explanation of the muon anomalous magnetic moment". In: *Physical Review D* 99.11 (June 2019). ISSN: 2470-0029. DOI: 10.1103/physrevd.99.115001. URL: http://dx.doi.org/10.1103/PhysRevD.99.115001.

[96] Joseph Bramante et al. "Inelastic frontier: Discovering dark matter at high recoil energy". In: *Physical Review D* 94.11 (Dec. 2016). ISSN: 2470-0029. DOI: 10.1103/physrevd.94.115026. URL: http://dx.doi.org/10.1103/PhysRevD.94.115026.

[97] Maxim Pospelov, Neal Weiner, and Itay Yavin. "Dark matter detection in two easy steps". In: *Physical Review D* 89.5 (Mar. 2014). ISSN: 1550-2368. DOI: 10.1103/physrevd.89.055008. URL: http://dx.doi.org/10.1103/PhysRevD.89.055008.

[98] A. Liam Fitzpatrick et al. "The effective field theory of dark matter direct detection". In: *Journal of Cosmology and Astroparticle Physics* 2013.02 (Feb. 2013), pp. 004–004. ISSN: 1475-7516. DOI: 10.1088/1475-7516/2013/02/004. URL: http://dx.doi.org/10.1088/1475-7516/2013/02/004.

[99] Matthew Mccgreadie. "The capture of Magnetic inelastic Dark Matter in the Sun." Master Thesis Dissertation. McMaster University, 2012. URL: https://macsphere.mcmaster.ca/bitstream/11375/13985/1/fulltext.pdf.

[100] Eduard Massó, Subhendra Mohanty, and Soumya Rao. “Dipolar dark matter”. In: *Physical Review D* 80.3 (Aug. 2009). ISSN: 1550-2368. DOI: 10.1103/physrevd.80.036009. URL: http://dx.doi.org/10.1103/PhysRevD.80.036009.

[101] D.S. Akerib *et al. An Effective Field Theory Analysis of the First LUX Dark Matter Search*. 2018. URL: http://teacher.pas.rochester.edu/pub/Lux/LUXRun03EFT/LUXeft_2018new_v0.pdf.

[102] Eugenio Del Nobile, Graciela B. Gelmini, and Samuel J. Witte. “Prospects for detection of target-dependent annual modulation in direct dark matter searches”. In: *Journal of Cosmology and Astroparticle Physics* 2016.02 (Feb. 2016), pp. 009–009. ISSN: 1475-7516. DOI: 10.1088/1475-7516/2016/02/009. URL: http://dx.doi.org/10.1088/1475-7516/2016/02/009.

[103] Eugenio Del Nobile. *Direct detection signals of dark matter with magnetic dipole moment*. 2017. arXiv: 1709.08700 `[hep-ph]`. URL: https://arxiv.org/abs/1709.08700.

[104] Vernon Barger, Wai-Yee Keung, and Danny Marfatia. “Electromagnetic properties of dark matter: Dipole moments and charge form factor”. In: *Physics Letters B* 696.1-2 (Jan. 2011), pp. 74–78. ISSN: 0370-2693. DOI: 10.1016/j.physletb.2010.12.008. URL: http://dx.doi.org/10.1016/j.physletb.2010.12.008.

[105] Sebastian Arrenberg. “Searching for Dark Matter with the Cryogenic Dark Matter Search Experiment”. PhD Dissertation. Universit¨at Z¨urich, 2011. URL: https://www.physik.uzh.ch/groups/groupbaudis/darkmatter/theses/cdms/arrenberg_phd_thesis.pdf.

[106] J.D. Lewin and P.F. Smith. “Review of mathematics, numerical factors, and corrections for dark matter experiments based on elastic nuclear recoil”. In: *Astroparticle Physics* 6.1 (1996), P87–P112. ISSN: 0927-6505. DOI: 10.1016/S0927-6505(96)00047-3. URL: http://www.sciencedirect.com/science/article/pii/S0927650596000473.

[107] Tom Banks, Jean-François Fortin, and Scott Thomas. *Direct Detection of Dark Matter Electromagnetic Dipole Moments*. 2010. arXiv: 1007.5515 `[hep-ph]`. URL: https://arxiv.org/abs/1007.5515v1.

[108] Moira I. Gresham and Kathryn M. Zurek. “Effect of nuclear response functions in dark matter direct detection”. In: *Physical Review D* 89.12 (June 2014). ISSN: 1550-2368. DOI: 10.1103/physrevd.89.123521. URL: http://dx.doi.org/10.1103/PhysRevD.89.123521.

[109] E. Aprile et al. “Effective field theory search for high-energy nuclear recoils using the XENON100 dark matter detector”. In: *Physical Review D* 96.4 (Aug. 2017). ISSN: 2470-0029. DOI: 10.1103/physrevd.96.042004. URL: http://dx.doi.org/10.1103/PhysRevD.96.042004.

[110] Carl Nave. *Nuclear Magnetic Moments*. 2003. URL: http://hyperphysics.phy-astr.gsu.edu/hbase/Nuclear/nspin.html.

[111] Kenneth S. Krane. *Introductory nuclear physics*. Singapore: JOHN WILEY & SONS, 1988.

[112] Jenö Sólyom. *Fundamentals of the Physics of Solids: Volume 1: Structure and Dynamics*. Budapest, Hungary: Springer, 2002.

[113] Martin Hoferichter et al. “Analysis strategies for general spin-independent WIMP-nucleus scattering”. In: *Physical Review D* 94.6 (Sept. 2016). ISSN: 2470-0029. DOI: 10.1103/physrevd.94.063505. URL: http://dx.doi.org/10.1103/PhysRevD.94.063505.

[114] P. Klos et al. “Large-scale nuclear structure calculations for spin-dependent WIMP scattering with chiral effective field theory currents”. In: *Physical Review D* 88.8 (Oct. 2013). ISSN: 1550-2368. DOI: 10.1103/physrevd.88.083516. URL: http://dx.doi.org/10.1103/PhysRevD.88.083516.

[115] Nikhil Anand, A. Liam Fitzpatrick, and W. C. Haxton. “Weakly interacting massive particle-nucleus elastic scattering response”. In: *Physical Review C* 89.6 (June 2014). ISSN: 1089-490X. DOI: 10.1103/physrevc.89.065501. URL: http://dx.doi.org/10.1103/PhysRevC.89.065501.

[116] Alan D. Martin Francis Halzen. *Quarks and Leptons: An Introductory Course in Modern Particle Physics*. New Jersey, USA: JOHN WILEY & SONS, 1984.

[117] Gary J. Feldman and Robert D. Cousins. "Unified approach to the classical statistical analysis of small signals". In: *Physical Review D* 57.7 (Apr. 1998), pp. 3873–3889. ISSN: 1089-4918. DOI: 10.1103/physrevd.57.3873. URL: http://dx.doi.org/10.1103/PhysRevD.57.3873.

[118] Kelsey Oliver Mallory. *Determination of Backgrounds for the LUX Experiment.* 2018. URL: https://indico.cern.ch/event/653314/contributions/2825765/attachments/1606246/2548594/LUX_Backgrounds_UCLA_2018_Kelsey_Oliver_Mallory.pdf.

[119] G. R. Araujo, T. Pollmann, and A. Ulrich. "Photoluminescence response of acrylic (PMMA) and polytetrafluoroethylene (PTFE) to ultraviolet light". In: *The European Physical Journal C* 79.8 (Aug. 2019). ISSN: 1434-6052. DOI: 10.1140/epjc/s10052-019-7152-2. URL: http://dx.doi.org/10.1140/epjc/s10052-019-7152-2.

[120] Mark Hanhardt. "Water Shield PMT Characterization and Muon Flux Surface Measurement for LUX Dark Matter Search". Master Thesis Dissertation. RAPID CITY, SOUTH DAKOTA: SOUTH DAKOTA SCHOOL OF MINES and TECHNOLOGY, 2011.

[121] P B Coates. "The origins of afterpulses in photomultipliers". In: *Journal of Physics D: Applied Physics* 6.10 (June 1973), pp. 1159–1166. DOI: 10.1088/0022-3727/6/10/301. URL: https://doi.org/10.1088%5C%2F0022-3727%5C%2F6%5C%2F10%5C%2F301.

[122] Kamal Singhrao. "Analysis of the Afterpulsing and the Dark Noise Spectrum from the DEAP-3600 Detector". Master Thesis Dissertation. University of Alberta, Jan. 2015. DOI: https://doi.org/10.7939/R3Q814Z0Q.

[123] Rüdiger Paschotta. *Photon Counting.* 2008. URL: https://www.rp-photonics.com/photon_counting.html.

[124] D. S. Akerib et al. "Extending light WIMP searches to single scintillation photons in LUX". In: *Physical Review D* 101.4 (Feb. 2020). ISSN: 2470-0029. DOI: 10.1103/physrevd.101.042001. URL: http://dx.doi.org/10.1103/PhysRevD.101.042001.

[125] Davide Porzio. *Measurement of optical properties of PTFE.* 2020. URL: https://indico.lip.pt/event/650/contributions/2121/attachments/1909/2546/LUX-ZEPLIN_overview_and_status.pdf.

[126] E. Aprile et al. “XENON1T dark matter data analysis: Signal reconstruction, calibration, and event selection”. In: *Physical Review D* 100.5 (Sept. 2019). ISSN: 2470-0029. DOI: 10.1103/physrevd.100.052014. URL: http://dx.doi.org/10.1103/PhysRevD.100.052014.

[127] P. Sorensen and K. Kamdin. “Two distinct components of the delayed single electron noise in liquid xenon emission detectors”. In: *Journal of Instrumentation* 13.02 (Feb. 2018), P02032–P02032. ISSN: 1748-0221. DOI: 10.1088/1748-0221/13/02/p02032. URL: http://dx.doi.org/10.1088/1748-0221/13/02/P02032.

[128] P.-A. Amaudruz et al. “Radon backgrounds in the DEAP-1 liquid-argon-based Dark Matter detector”. In: *Astroparticle Physics* 62 (Mar. 2015), pp. 178–194. ISSN: 0927-6505. DOI: 10.1016/j.astropartphys.2014.09.006. URL: http://dx.doi.org/10.1016/j.astropartphys.2014.09.006.

[129] Various authors. *Table de Radionucléides.* 2010. URL: http://www.nucleide.org/DDEP_WG/Nuclides/Bi-214_tables.pdf.

[130] M.M. Bé *et al. LE RADIUM 226 ET SES DESCENDANTS:Tables et commentaires.* 2004. URL: http://www.nucleide.org/DDEP_WG/Ra-226D_NT04-04.pdf.

[131] Thormod Henriksen. *Radioactivity and X-rays: Applications and health effects.* 2009. URL: https://www.mn.uio.no/fysikk/english/research/publications/other/radioactivity-xrays.pdf.

[132] V. Chisté *et al. Evaluation of decay data of radium-226 and its daughters.* 2007. URL: https://nd2007.edpsciences.org/articles/ndata/pdf/2007/01/ndata07122.pdf.

[133] E. Aprile et al. “Intrinsic backgrounds from Rn and Kr in the XENON100 experiment”. In: *The European Physical Journal C* 78.2 (Feb. 2018). ISSN: 1434-6052. DOI: 10.1140/epjc/s10052-018-5565-y. URL: http://dx.doi.org/10.1140/epjc/s10052-018-5565-y.

[134] LUX collaboration. “Backgrounds in the extended LUX rare event search”. In: *LUX Internal note* (2019).

[135] Akira Hitachi. “Properties of liquid xenon scintillation for dark matter searches”. In: *Astroparticle Physics* 24.3 (2005), pp. 247–256. ISSN: 0927-6505. DOI: https://doi.org/10.1016/j.astropartphys.2005.07.002. URL: http://www.sciencedirect.com/science/article/pii/S0927650505000964.

[136] C.R. Nave. *Energy and Momentum Spectra for Beta Decay*. URL: http://hyperphysics.phy-astr.gsu.edu/hbase/Nuclear/beta2.html.

[137] C.R. Nave. *Fermi Theory of Beta Decay*. URL: http://hyperphysics.phy-astr.gsu.edu/hbase/quantum/fermi2.html#c1.

[138] G. Drexlin et al. “Current Direct Neutrino Mass Experiments”. In: *Advances in High Energy Physics* 2013 (2013), P1–P39. ISSN: 1687-7365. DOI: 10.1155/2013/293986. URL: http://dx.doi.org/10.1155/2013/293986.

[139] D.S. Akerib et al. “Radiogenic and muon-induced backgrounds in the LUX dark matter detector”. In: *Astroparticle Physics* 62 (Mar. 2015), pp. 33–46. ISSN: 0927-6505. DOI: 10.1016/j.astropartphys.2014.07.009. URL: http://dx.doi.org/10.1016/j.astropartphys.2014.07.009.

[140] John E. Davis. “Event Pileup in Charge-coupled Devices”. In: *The Astrophysical Journal* 562.1 (Nov. 2001), P575–P582. DOI: 10.1086/323488. URL: https://doi.org/10.1086%5C%2F323488.